University of Southampton

Faculty of Engineering and Physical Science

Optoelectronics Research Centre

3D Printed Optical Fibre-Preforms in Silica and Polymer Materials

DOI : 10.5258/SOTON/D1642.

by

Angeles Lilian Camacho Rosales

ORCID ID 0000-0003-3603-7561

Thesis for the degree of Doctor of Philosophy

November 2020

University of Southampton

ABSTRACT

Faculty of Engineering and Physical Science
Optoelectronics Research Centre

Thesis for the degree of Doctor of Philosophy

3D Printed Optical Fibre-Preforms in Silica and Polymer Materials

by

Angeles Lilian Camacho Rosales

The fabrication of the new generation of optical fibres faces important challenges due to the complexity in their designs and compositions. Some examples of novel designs of optical fibres include those with complex geometries on single or multiple materials and fibres with high dopants content. The current fabrication processes for these fibres require many-step, which can compromise the integrity of the preforms, reducing both repeatability and yield. This thesis proposes a novel alternative fabrication method for optical preforms fabrication based on additive manufacturing processes (AM). Due to the high level of accuracy and repeatability, AM processes are a promising solution to the fabrication of the new generation of optical fibre. Fabrication of ceramics and polymers with optical properties have been explored using AM methods.

In this PhD thesis, AM processes were analysed as an alternative fabrication method for optical fibres. In particular. laser powder bed fusion (LPBF) and direct ink writing (DIW) methods were used to produced silica preforms, while fused deposition modelling (FDM) was used to produced cyclic olefin copolymer (COC) preforms. The development of the processes and the results of the optical characterization of the fabricated fibres are reported.

LPBF for silica powder was developed, producing porous silica bodies with a relative density of 51%. A CO_2 laser beam with a wavelength of 10.6µm was used to process SiO_2 spherical powder. The material was characterised, and the development of the printing process is reported. The 3D printed bodies were fabricated with an energy density of 2.1J/mm^3. After the LPBF process, the porous bodies were heat-treated for densification. 3D printed parts were densified in a furnace chamber at 1575˚C for 1.5 hours (10 min dwell) with an inert atmosphere, reaching an average relative density of 93%. The 3D printing parameters reported in this work are the starting point for producing silica optical preforms by LPBF

LPBF was used to fabricate 3D printed silica preforms with complex structures as well as preforms with multiple materials such as step-index and multicore structures. Following the developed LPBF process, silica preforms of photonic crystal and antiresonant structures were fabricated. The 3D printed preforms reached a relative density of 54% using an energy density of 2.7J/mm^3. The resolution of the preforms' internal lattice is 1mm walls thickness.

Silica powder was doped with GoO_2, and the developed mixing process is reported. Ge-doped silica powder was used to fabricate a step-index and multicore fibres. The multiple materials optical fibre presents and attenuation of 8.3 dB/m at a wavelength of 800nm

An Er-doped silica fibre was fabricated from a 3D printed optical preform using a DIW process. A colloidal ink of nanoparticle size of hydrophobic silica powder was developed. The produced Er-doped silica ink was used to fabricate a 3D printed preform, which was drawn into a fibre. An overview of the fibre fabrication process is reported. The optical fibre presents an absorption of 62.98dB/m at 980nm and 151.49dB/m at 1535nm.

Additive manufacturing methods for polymer preforms were analysed. The optical and thermal properties of a variety of polymers used for optical fibre fabrication were analysed. COC preforms with complex structures were produced by FDM. The development of the fabrication process for COC filaments is discussed. Fibres from 3D printed preforms were drawn and characterised by THz time-domain spectroscopy (THz-TDS). The produced fibres transmit in the range below 0.5THz with attenuation similar to the noise level above 0.8THz

This thesis contribution is the proof that the use of additive manufacturing processes (such as LPBF, DIW and FDM) is a viable approach for the fabrication of optical fibres with novel designs such as complex geometries or multiple materials.

Table of Contents

Table of Figures

List of Equations

List of Tables

Research Thesis: Declaration Of Authorship

Print Name: Angeles Lilian Camacho Rosales

Title of thesis: 3D Printed Optical Fibre-Preforms in Silica and Polymer Materials

I declare that this thesis and the work presented in it are my own and has been generated by me as a result of my own original research.

I confirm that:

1. This work was done wholly or mainly while in candidature for a research degree at this University;
2. Where any part of this thesis has previously been submitted for a degree or any other qualification at this University or any other institution, this has been clearly stated;
3. Where I have consulted the published work of others, this is always clearly attributed;
4. Where I have quoted from the work of others, the source is always given. With the exception of such quotations, this thesis is entirely my own work;
5. I have acknowledged all main sources of help;
6. Where the thesis is based on work done by myself jointly with others, I have made clear exactly what was done by others and what I have contributed myself;
7. Parts of this work have been published as:

   [1] Camacho-Rosales, A., et al. *3D printed Er-doped silica fibre by Direct Ink Writing*, Europhoton, September 2020,

   [2] Camacho-Rosales, A., et al. *Optical fibres produced by 3D printed silica preforms*, Photonics West, February 2020.

   [3] Camacho-Rosales, A., et al. *Development of 3-D Printed Silica Preforms*, Conference on Lasers and Electro-Optics Europe and European Quantum Electronics Conference. 2019. Munich: Optical Society of America.

   [4] Camacho-Rosales, A., et al. *Additive manufacturing towards fabrication of next generation of optical fibres*, 6th International Symposium on Optics and its Applications (OPTICS 2018), SPIE FOCUS, February 2018.

Signed: Date:17th November 2020

Acknowledgements

The following institutions are gratefully acknowledged for the support received during this research project.

- National Council of Science and Technology – CONACyT México (Consejo Nacional de Ciencia y Tecnología), CVU 607008.
- Faculty of Engineering and Physical Sciences and, University of Southampton
- Engineering and Physical Sciences Research Council (EP/M020916/1)
- Centre for Innovative Manufacturing in Photonics
- Centro de Física Aplicada y Tecnología Avanzada de la Universidad Nacional Autónoma de Mexico (Centre of Applied Physics and Advanced Technology from the National Autonomous University of Mexico).

I want to thank to:

My supervisor, who believed in my work and gave me the opportunity to participate in this research project.

Colleagues and friends that always have supportive words and were ready to help anytime I asked for it.

Senta, my dear friend that spend many hours helping me and always was there with a smile. Thank you for your support and friendship. Ich liebe dich Freund

Adriana, that always supported me and gave me her unconditional friendship. Te quiero mucho amiga.

My siblings and mother that never give up on me.

Gaby and Lalo. Thank you for being there for my family.

Socorro, who guided me, loves me and trusted in me no matter what.

Josefine that I will be in my heart for the rest of my life. Thank you my dear friend wherever you are.

Daniel and Carlos, my beloved sons. I want you to know that every effort has its rewards and what it is worth requires work, patience, but mainly love and trust. Always be honest with you and work for what you want and never give up. Keep going! Even when you think you cannot do it; you always will find the way. It's in your genes.

My dear and beloved husband. This project, this path, this happiness couldn't happen without you. We have walked a long way together, and I think we are the best team ever. In every down moment, you are there to support me. This thesis is a product of all our effort, work and support as a family but mainly this was possible thanks to your support. Thank you! Te amo mil!

Definitions and Abbreviations

All the units in this document are given under the International System of Units, its derived units, multiple and sub-multiples; unless otherwise specified in the text.

The preforms and fibres refractive index is given at a wavelength of 633nm unless it is specified a different wavelength in the graph.

Equipment:

DSC	Differential Scanning Calorimetry.
IFA	Multi-wavelength optical fibre analyser
OSA	Optical Spectrum Analyser
SEM	Scanning Electron Microscope.
TGA	Thermogravimetric analysis or thermal gravimetric analysis
THz-TDS	Terahertz-Time Domain Spectroscopy.
WLS	Wight Light Source
XRD	X-Ray Diffraction.

Materials:

ABS	Acrylonitrile Butadiene Styrene.
COC	Cyclic Olefin Copolymer
FEP	Fluorinated ethylene propylene.
$GeCl_4$	Germanium tetrachloride.
HDPE	High Density Polyethylene.
PA	Polyamide.
PC	Polycarbonate.
PDMS	Poly(dimethylsiloxane).
PE	Polyethylene.
PET-G	Polyethylene Terephthalate Glycol.
PLA	Polylactic Acid.
PMMA	Poly(methyl methacrylate).
$POCl_3$	Phosphorus oxychloride.
PTFE	Polytetrafluoroethylene.
RE	Rare-earth, chemical elements from the lanthanides series.
$SiCl_4$	Silicon tetrachloride.
xN	Refers to the number of ‘nines’ in the purity level of a compound, for instance, a compound referred as 4N refers to a purity level of 99.99%, whereas 6N refers to 99.9999% purity.

Related to Optical Fibres:

ARF	Anti-resonant Fibres.
EOP	Elastomer optical fibre.
LWIR	Long-wavelength infrared.
MCVD	Modified Chemical Vapour Deposition.
MOF	Micro-structured Optical Fibre.
MPOF	Micro-structured Polymer Optical Fibre.
OF	Optical Fibre.
OVD	Outside Vapour Deposition.
PCF	Photonic Crystal Fibre.
POF	Polymer Optical Fibre.
PPCF	Polymer Photonic Crystal Fibre.
SOF	Silica Optical Fibres.
THz	Terahertz.
VAD	Vapour Axial Deposition.

Related to Additive Manufacturing:

CAD	Computer-Aided Design.
DIW	Direct Ink Writing.
DLMS	Direct Laser Metal Sintering.
DLP	Digital Light Processing.
FDM	Fused Deposition Modelling.
LPBF	Laser Powder Bed Fusion
SLA	Stereolithography Apparatus.
SLM	Selective Laser Melting.
SLS	Selective Laser Sintering.
STL	Native file format of the stereolithography CAD software.

Chapter 1 Introduction

1.1 Background

Optical fibres play an extremely important role in different areas of the economy. For instance, optical fibres find use in telecommunications, health applications and environmental sensing[1]. The mechanical and optical properties of the optical fibres make them an efficient and reliable component for devices such as sensors for temperature, pressure or strain in a variety of applications, including those in harsh environments[2,3]. Novel fibre designs that include the use of complex geometries and multi-material compositions are features of the new generation of optical fibres in sensing[4]. In the high-power laser industry, optical fibres are mainly used for manufacturing processes such as metal-processing, (such as engraving, cutting, welding) and additive manufacturing (3D printing)[5].

The development of novel optical fibres with complex geometries and multiple materials face several limitations. These limitations are mainly in process control, repeatability and yield. Parameters such as geometry stability, dimensions and dopant distribution are among the principal challenges of this optical fibre technology. Moreover, the current processes are expensive, time-consuming and have limited scalability.

Conventional fabrication processes such as Modified Chemical Vapour Deposition (MCVD), Outside Vapour Deposition (OVD) and Vapour Axial Deposition (VAD)[6,7] are limited to produce only preforms with cylindrical geometry, due to the nature of these processes. Therefore, it is necessary to post-process the original preform to produce specialty optical fibres. Unfortunately, these processes, such as milling, drilling and stacking assembly, can endanger the preform integrity and the precision is restricted by the equipment resolution and the operator skill. For instance, preforms fabricated by a stacking process[8], which are used in the fabrication of microstructured optical fibre, requires multiple drawing and assembly stages before the final fibre can be produced. This fabrication process is complex, time-consuming, and the repeatability of the preforms is compromised due to the complexity of the process. Therefore, this thesis proposes an alternative manufacturing process based on additive manufacturing technology.

Additive Manufacturing (AM), also known as 3D printing, has the advantage of being able to build complex shapes with high accuracy and repeatability[9]. These manufacturing methods are currently used in many industries around the globe for the development of the next generation of products and technologies, allowing the construction of complex geometries and control of selective deposition. Nowadays, there are some examples of 3D printing processes currently used for manufacturing optical components such as polymer lenses[10] and polymer optical fibres[11]. Polymer optical components are of particular interest for sensing applications[2], lenses[12] and microstructure optical fibres[13].

1.2 Aim of research

The present research project aims to assess the viability to produce optical preforms and fibres with intricate designs by additive manufacturing. Produced optical preform fabricated by AM can provide a highly flexible and versatile alternative technology to manufacture advanced optical preforms. These can revolutionise the way in which optical fibres are fabricated and facilitate the technology transfer to industry.

In this project, two different materials were analysed, which are currently used in the production of optical fibres: silica (SiO_2) and polymers. The objectives that this thesis pursues are described in the sections below for each material.

1.2.1 Silica preforms

Silica optical fibres are of great interest due to their wide range of applications, particularly for harsh environments. The main target of this section is to develop a fabrication process of silica optical fibres. The optical and geometrical profile of the produced fibres is a key evaluation factor in this work. Therefore, the chemical, mechanical and physical properties of the raw material were evaluated for the AM fabrication methods proposed in this thesis: laser powder bed fusion method (LPBF) and direct ink writing method (DIW). Specific objectives were completed to produce 3D printed silica fibres by AM processes.

1. Development of the 3D printing process for silica bodies using AM methods.
2. Development of the sintering process for 3D printed silica bodies.

3. Production of 3D printed preform with simple geometries using AM methods.

4. Development of the drawing process for 3D printed solid silica preform.

5. Production of 3D printed preform with complex geometries using AM methods.

6. Production of 3D printed preform with complex geometries and multiple materials by AM methods.

7. Drawing and characterisation of optical fibres produced using AM methods.

1.2.2 Polymer preforms

Polymer optical components are of particular interest for sensing applications, lenses and microstructure optical fibres. 3D printing methods for polymers are widely used for different types of polymers. For this research project, the next specific targets are considered.

1. Development of the 3D printing process for COC preforms using Fused deposition modelling (FDM).

5. Printing of preforms with complex shapes without voids between layers, reaching and smooth surface.

6. Establish drawing conditions for polymer optical preforms

7. Drawing of 3D printed optical preforms

8. Characterisation of polymer optical fibres fabricated from 3D printed optical preforms using FDM.

1.3 Research Methodology

The PhD project described in this thesis evaluated the viability of the additive manufacturing processes as a solution to the complex fabrication process of novel optical fibre designs. Two materials with different physical properties were used in this thesis: silica and polymer. Materials used in this PhD project are novel materials to be used for the AM process. Therefore, the development of the process and the fabrication parameters must be determined by a systematic procedure according

to the specific objectives described in section 1.2.1 and 1.2.2. The methodology described below was followed to achieve the project aim.

I. Evaluation of different AM methods used for glasses.
II. Definition of AM methods used in this research project based in the chosen materials.
III. Performing preliminary experiments with the chosen material.
    a. Material characterization
    b. Equipment characterization
IV. Definition of experimental methodology.
    a. Production of green bodies with the 3D printing method
    b. Densification of the printed body by heat treatment
    c. Preform preparation for drawing preparation
    d. Optical fibre fabrication
    e. Optical fibre characterisation

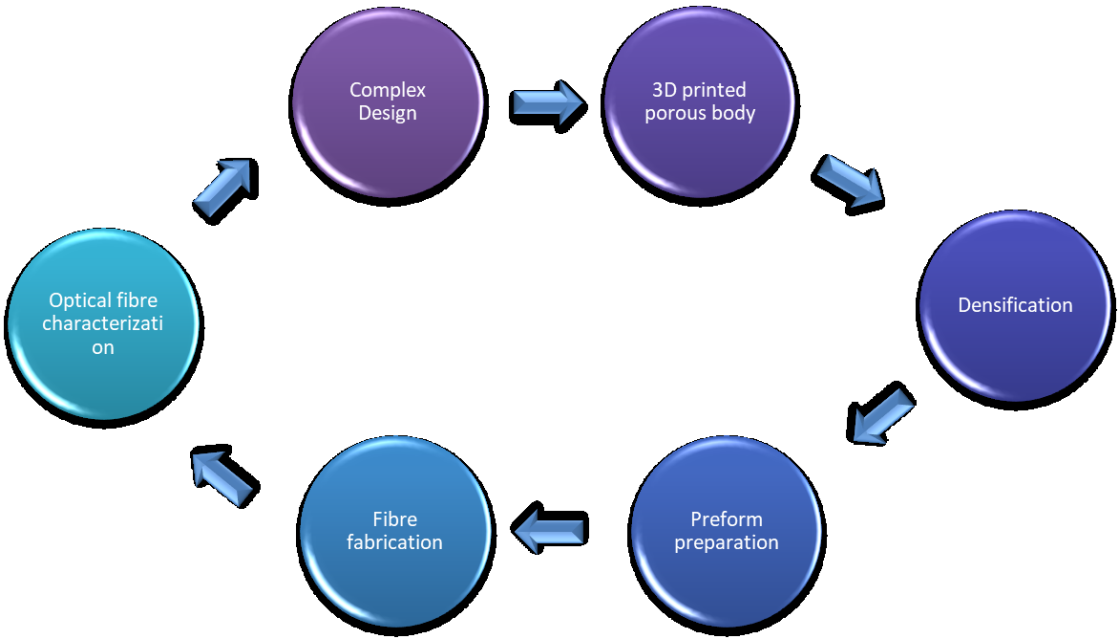

Figure 1. Experimental methodology

V. Experimental execution
    a. Development of 3D printing process of silica preforms.
    b. Fabrication of optical preforms with complex designs using a 3D printing method
    c. Fabrication and characterization of optical fibres from 3D printed silica preforms.

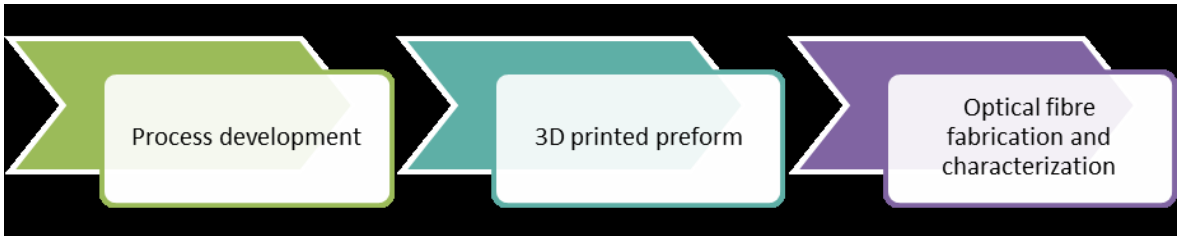

Figure 2. The strategy of experimental execution.

1.3.1 Statement of novelty

This research project has shown the capability to produced optical fibres based in additive manufacturing processes. This project has been accomplished by the careful control of the chemical, mechanical, optical and physical properties of the employed materials. The fabrication of silica optical fibres with complex geometries and multiple materials by additive manufacturing methods reported in this work is the first in its class. The presented work demonstrates novelty in the following areas:

- Functionalisation of additive manufacturing methods of glass for optical fibre fabrication
- Fabrication of 3D printed glass using three process stages: silica printed bides by LPBF, consolidation of the printed porous body and finally, glass formation at exposure to high temperature.
- Development of 3D printing processes for doped silica optical fibre using LPBF and DIW.
- Fabrication of optical fibres with complex structures and multiple materials using additive manufacturing methods.

1.4 Structure of the Thesis

The content of this thesis is presented in eight chapters, which content theoretical background, literature review, experimental results and discussion as well as a conclusion of the research project. Chapter 2 discusses state of the art and the theoretical background where the project liaised. The experimental results are presented in the four following chapters, followed by a thorough discussion in Chapter 7. Finally, the conclusions and further work is presented in Chapter 8.

1.4.1 Outlines

Chapter 2; The commonly used processes for optical preforms fabrication are described in section 2.2, as well as the fibre drawing process and an overview on different applications for optical fibres in telecommunications, sensing and high power laser. Section 2.3 focuses on additive manufacturing technologies, their applications and different processes. The variety of additive manufacturing methods are also described in this chapter, as well as the 3D printing methods currently used for glass are thoroughly discussed in this section.

Chapter 3; In this chapter, the development of the LPBF process for silica powder is presented, and the fabrication of 3D printed silica parts is demonstrated. Sections 3.1 and 3.2, showed preliminary experiments on 3D printing silica bodies as well as the analysis of material feasibility to produce porous bodies using a laser printing process. The development of doped silica powder and sintering process of the produced 3D printed silica porous bodies is also described in this chapter.

0; This chapter, describes the development of the printing fabrication process of silica preforms using a customised laser-based printed apparatus. In section 4.2 and 4.3 3D printed silica preforms with complex geometries and multiple materials are presented. In addition, the fabrication of optical fibres from 3D printed silica preforms is described. Finally, the profile and characterisation of the obtained optical fibres are presented.

Chapter 5; The experimental results for silica preform fabrication using direct Ink writing are described in this chapter. The use of hydrophobic silica and rare-earth-doped silica for 3D printed preforms was demonstrated and reported. Optical fibres drawn from the silica 3D printed preforms were characterised, and their results are discussed in this chapter. The exploration of other AM method for silica preforms is driven by the need for a purer silica host and reduction of the losses in the fibre originated from the raw material used in LPBF.

Chapter 6; Polymer preforms were fabricated using FDM. Novel optical preforms designs based on complex geometries were fabricated in COC (Topas®). The details and characteristics of the fabricated polymer-based optical preforms and fibres are discussed in this chapter.

Chapter 2 Literature Review

2.1 Introduction and Structure

In this chapter, the general background of optical fibre technologies, as well as additive manufacturing technologies, are discussed. The importance of optical fibres within the technological era of today is described as well as the current fabrication processes for passive and active optical fibres and fibres with novel designs. The drawbacks of these fabrication processes are highlighted along with the need for innovative solutions to cope with the current challenges in the fabrication processes for the new generation of optical fibre.

In addition, a variety of additive manufacturing processes and their potential for application in optical technologies are discussed. The 3D printing processes are described along with the materials commonly used with this technology. The state of the art of additive manufacturing technologies for the fabrication of glass and optical components is also discussed.

2.2 Optical Fibre Technology

The last four decades have seen rapid development in fibre optics technology. Optical fibres have evolved from being a simple waveguide for telecommunication purposes to complex optical components for a wide variety of applications such as optical amplifiers, sensors, fibre lasers, polarisers and numerous other devices[14]. Its improvement and a broad range of applications were enabled by the evolution of different materials, designs and refinement of fabrication processes of the optical fibre. The best example of this improvement is the erbium-doped fibre amplifier (EDFA)[15], allowing the telecommunication channels to use an optical amplification instead of the original low efficient electro-optic conversion. This was a turning point in the history of telecommunications, and its success arose from the development of doped fibres in the 1980s and 1990s.

Polymer fibres (POF), soft glasses fibres and photonic crystal fibres (PCF) are other examples of the evolution of the optical fibre through the last couple of decades. The demand for new high-performance optical fibres in telecommunications and other application such as medicine, environment and energy has triggered the

development of the next generation of optical fibres. These make use of complex geometries, high dopant concentration and large active areas. Some examples of these fibres are microstructured optical fibre (MOF) and PCF.

These fibres currently have a key role in numerous fields of research and industrial applications[16]. Their applications go from fibres with low levels of nonlinearities for supporting high-power pulses, to highly nonlinear counterparts for supercontinuum generation. The current drawback for those types of fibre lies in its fabrication processes, which include complex shapes such as staking[14,17]. These processes result in complex structures such as gradient index guiding, photonic bandgap (PBG) and anti-resonant fibres (ARF). An example of these designs is shown in Figure 3: a) PCF b) PBG and c) ARF. However, complex and time-consuming processes are the main routes for the fabrication of these fibres, which still require a great effort in their development.

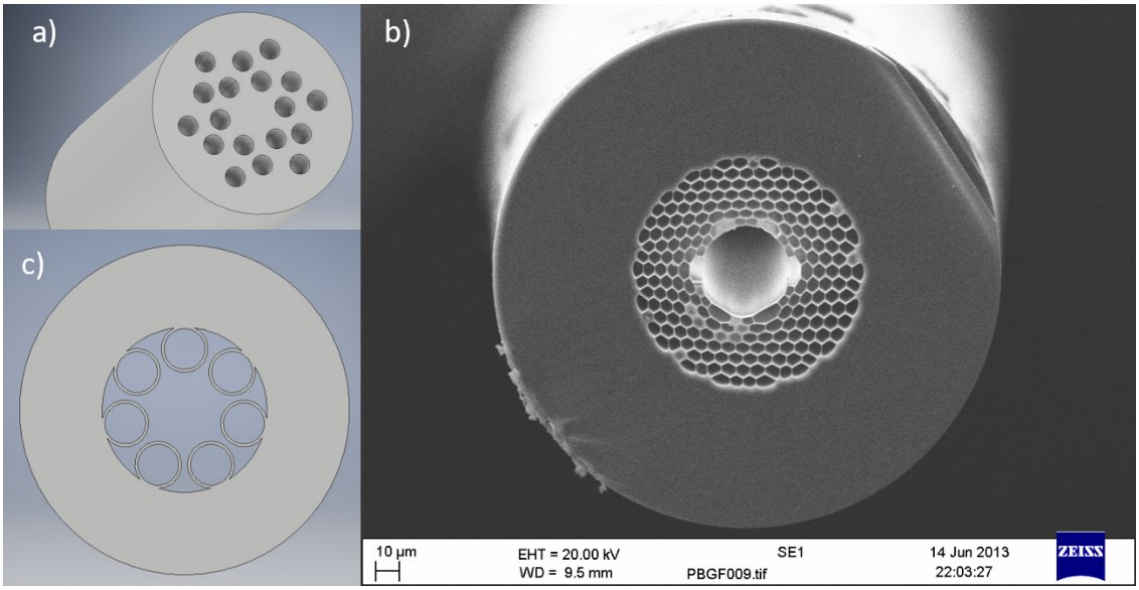

Figure 3. Examples of optical fibres with complex geometries; a) PCF; b) PBG; c) ARF.

Optical fibres are commonly made from either glasses or polymers. The purity of the raw materials is a critical factor for fibre performance. Due to its outstanding properties and relatively low cost, SiO_2 is the most commonly used material for optical fibre fabrication[18]. However, silica is not the only material employed for optical fibres as some soft glasses such as germanates[19] and even chalcogenides[20] are used more and more often in optical fibre fabrication.

2.2.1 Optical preform manufacturing

Preforms can be built either by Modified Chemical Vapour Deposition (MCVD), Outside Vapour Deposition (OVD) and Vapour Axial Deposition (VAD) processes[21,22]. Figure 4 shows an example of an MCVD lathe commonly used for preform fabrication within the industry. In MCVD silica soot is deposited inside a rotating substrate, which is typically a silica glass tube that will be later used as cladding. The dominating phenomena in this process is known as thermophoresis[23].

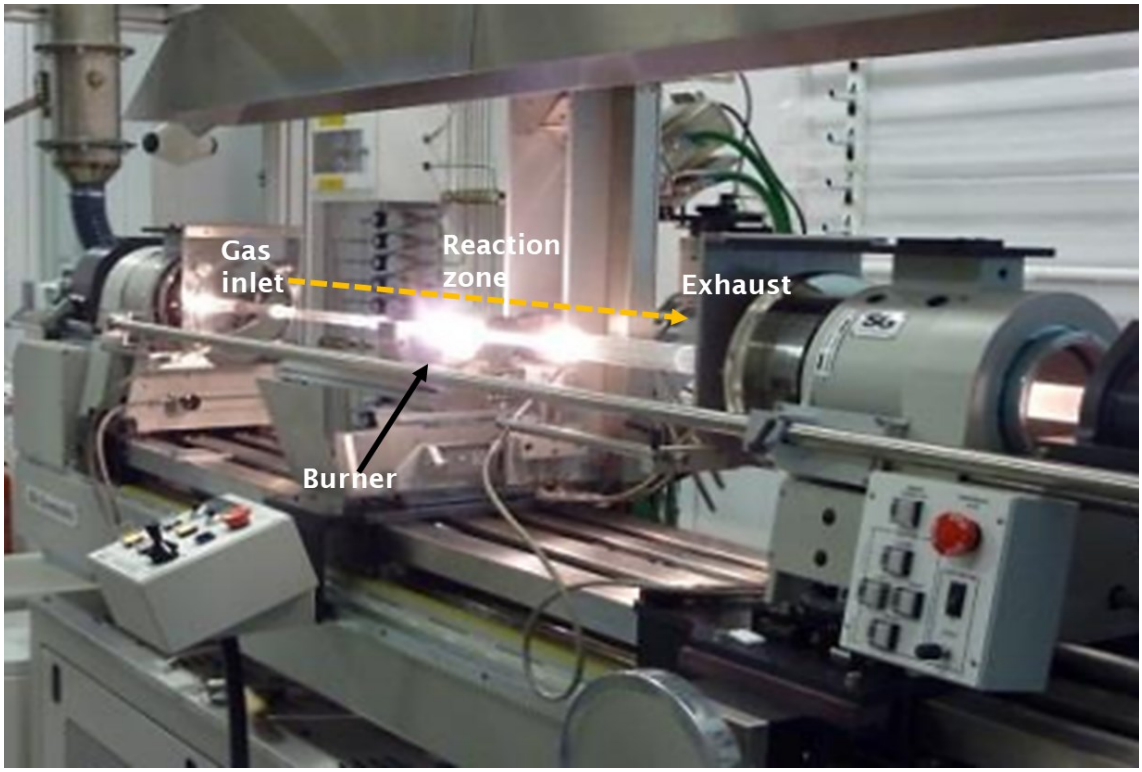

Figure 4. Schematic of the MCVD process.

The substrate tube is heated from the outside to ~1600˚C using a flame. The deposited soot is produced by a chemical reaction between an O_2 flow and a saturated vapour flow of $SiCl_4$. Depending on the application, additional flows can be added to the reaction zone such as $GeCl_4$ or $POCl_3$, for passive preforms and rare-earth dopants for active preform fabrication. The inner layer deposited in the tube will eventually form the core of the preform and hence of the fibre. After the soot deposition, the temperature is increased to completely sinter the soot layer, after which the collapsing process starts, exposing the tube to temperatures above 2200˚C. High temperatures, reduced traverse speed and control internal pressure allow the softened glass to collapse until it reaches the sealing stage where the final preform is produced.

On the other hand, processes such as OVD and VAD differ in the way the soot is deposited and formed. The preform building process starts from the outside, requiring the core layers composition to be deposited first, followed by the cladding. After the deposition is finished, the preform requires to be dehydrated and then finally consolidated, which is equivalent to the sintering process in the MCVD method.

The new generation of optical fibres[24,25] requires more complex and hybrid fabrication methods. Complex geometries, high dopant concentrations, multicore structure and large core diameters are some features of the novel designs that are not possible to be fabricated by conventional fabrication methods. For instance, MOFs are fabricated by an expensive and time-consuming process called stacking[16]. In this fabrication process, a considerable number of capillary tubes and/or rods are arranged in a specific design followed by a complex multi-step drawing process[26,27]. Other novel designs target high concentrations of dopants[28-31] and multicore structrures[32,33], which can be achieved by hybrid fabrication methods such as drilling, milling and chemical etching. The post-processing methods; however, usually endanger the mechanical integrity of the preforms compromising yields, quality and repeatability of the fibre production.

2.2.2 Optical fibre manufacturing

The optical fibre fabrication process is carried out by drawing the optical preform in a fibre drawing tower[34]. The process starts by positioning the preform inside a vertical furnace where the temperature is increased beyond the softening point so that the reduced viscosity of the glass allows the formation of an initial section called ‘drop’. This drop pulls the glass down such that the tip of the preform tapers down to a filament of reduced diameter, usually in the same order of magnitude than the desired fibre. The cane/fibre is pulled at a constant speed by a tractor or mini capstan. Once the size of the fibre is small enough to pass through the coating stage, the fibre is passed through a die which will control the thickness of the coating. Depending on the application, different materials can be used at this stage to coat the optical fibre in single or multiple stages. Photo-polymerisation has been adopted as one of the most widely used processes to cure the resins applied for optical fibre fabrication allowing high speed and reduced vapour generation from the by-products. The coating provides the mechanical strength to the fibre enabling the possibility to bend and collect the fibre using a larger capstan which feeds the fibre into a winder. Multiple parameters such as tension, bare fibre diameter,

preform feed and fibre line speed are closely monitored during the process. Figure 5 shows a schematic of the general process of fibre drawing.

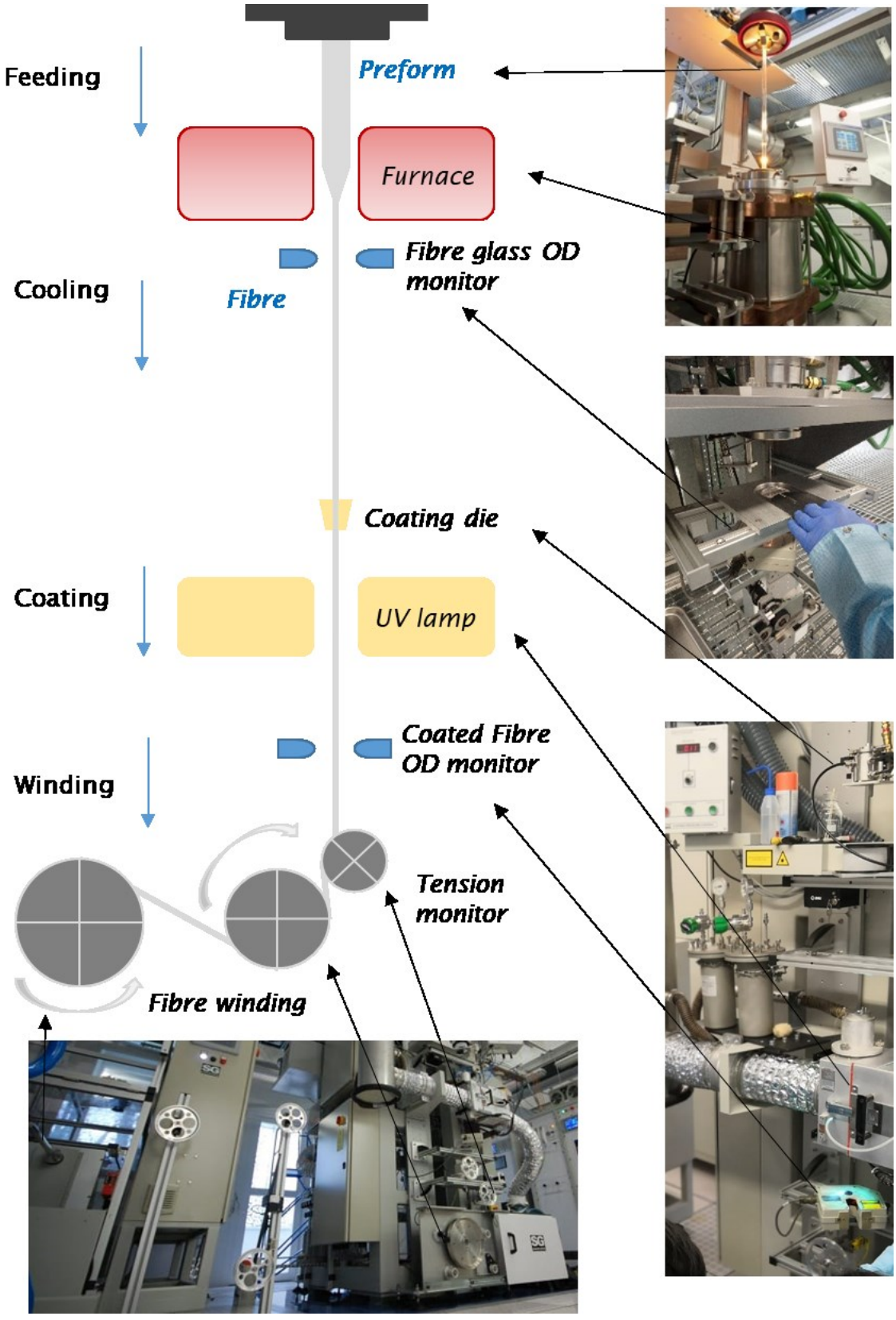

Figure 5. Schematic of the optical fibre fabrication process.

2.2.3 Glass hosts for optically active dopants

Optical fibres obtain their waveguiding properties through a refractive index contrast between core and cladding. Therefore, dopants must be added to the silica in the core region in order to modify the refractive index. While GeO_2, P_2O_5, B_2O_3, and Al_2O_3 can be added to the silica matrix for passive fibres, lanthanides can be added for active fibre designs. Incorporation of these compounds to the silica matrix gives the fibre specific properties. For instance, a phosphosilicate glass host raises the refractive index and reduces viscosity, thermo-optic coefficient (TOC), and reduces photo-darkening, while fluorosilicates reduce both the linear and nonlinear refractive index and viscosity of the glass[35]. Usually, SiO_2, GeO_2, and P_2O_5 are compounds that are formed through the oxidation of saturated vapour. Fluorine is generally added directly as a precursor in the gas phase. Aluminium and rare-earths can be incorporated into the glass matrix by solution doping. They can also be added in the gas phase or a hybrid combination between the gas phase and solution doping[36]. These fabrication methods offer a wide range of glass hosts and dopant compositions that aims to satisfy the novel designs in optical fibre fabrication.

Silica-based glasses cannot be used in applications beyond 2.1-2.2 μm due to the intrinsic silica IR-absorption. Therefore, other glasses have been developed to operate in wavelengths beyond the 2μm range. Chalcogenide, fluorides and germanates are examples of glasses without silica in its matrix. The demand of these fibres to use for long-wavelength range imaging and sensing has triggered the need to find innovative glass hosts. Chalcogenides show a broad transmission spectrum from the visible to the long-wavelength infrared (LWIR). Depending on their composition, chalcogenide glass can be used for mid-infrared supercontinuum generation[37].

2.2.4 Novel Optical Fibre Designs

The development of optical fibres technologies and their designs have been driven mainly by their applications. Biomedicine, energy and telecommunication are fields that require novel fibre designs with complex structures and/or multiple materials. One example of these novel applications is in the biomedical sector, where the use of optical fibre technologies have offered advantages in the detection and treatment of health conditions, offering innovative and revolutionising solutions for remote sensing, imaging and medical care[38,39].

The optimisation of the light transmission and its manipulation to fulfil the purpose of the fibre design has prompted novel configurations, shapes and structures with fibre geometries increasingly complex such as PCF, PBG (e.g. honeycomb and Kagome[40]) and anti-resonant[41]. Fabricating these complex geometries requires long fabrication process such as stacking, where the accuracy and repeatability from one preform to another is the main challenge. Therefore, alternative fabrication methods are desired to overcome the current limitations and eventually transfer these methods to a more reliable process suitable for industrial fabrication.

Multicore fibre, bow-tie, panda and elliptical jacket fibres are other types of complex geometries that have emerged for applications in sensing, medicine and telecommunications[42]. The challenges in manufacturing these fibres are mainly in the manipulation of the preforms during the different post-processing stages. Milling, drilling and in some cases chemical etching are operations that are used for these speciality preforms in order to give them the desired properties for the final fibre. This can compromise the mechanical integrity of the preform resulting in low yields. The repeatability and accuracy in the fabrication process are the main concerns for the industries fabricating these fibres.

Despite the current variety and engineering solutions to fabricate novel optical fibres, the drawbacks mentioned in this section, prevent or limit these technologies to be fabricated with higher yields. It is; therefore, essential to develop an alternative manufacturing method that overcomes these challenges. Nowadays, additive manufacturing (AM) processes, also known as 3D printing processes, are gaining acceptance for industrial and medical solutions due to its accuracy, repeatability and prompt feedback to the designs. Some methods, such as FDM for tissue scaffolding in medicine or laser printing in the metal-mechanic industry, have revolutionised the manufacturing industry. However, in terms of fabrication of optical components, there is still much to explore and resolve to establish 3D printing processes as a solution for the current limitations in fibre fabrication. In section 2.3, a thorough discussion of AM technology is presented. The application of this manufacturing technology for ceramics and optical materials is also discussed, aiming to understand their advantages and drawbacks for its application in optical fibre fabrication.

2.2.5 Polymer Optical Fibres overview

In recent years, polymer optical fibres (POF) have gained acceptance in its use for the visible wavelength range[43]. Its capability of measuring temperature, strain and

humidity is leading the research on POF using materials such as Polymethyl methacrylate (PMMA), Polystyrene (PS) and Polycarbonate (PC) as viable options in sensing applications with outstanding results in recent years[44]. During the early 1960s DuPont built, a POF for the first time, based on PMMA with an attenuation above 1000dB/m[45] measured at a wavelength of 650nm. The development of POF started in the early 1980s when NTT reported losses of 55dB/km measured at 570nm in its PMMA fibre[46]. With the expansion of the internet and associated technologies in the 1990s, POF found an excellent opportunity in the market for short-range applications.

The main advantages of POF over conventional silica fibres are the greater elastic and plastic strain deformation, negative thermal sensitivities, high numerical aperture and low stiffness on large diameters[47]. POFs have been positioned in specific applications such as medium to short-range data transmission[48] as well as for high sensitivity of low-temperature measurements, due to its low glass transition temperature. This POF's material feature allows to sensing small temperature variations at a low-temperature range.

POFs are commonly used for multimode, short-distance communication in local area networks (LAN) and datacentres, as well as applications in digital home appliances, home networks and industrial networks. In recent years, work has been done to extend the use of POF in sensing and medicine[49]. Some of the applications for POFs are listed in Table 1 according to their material.

Table 1. POF materials and their applications.

Material	Applications
PMMA (Polymethyl methacrylate)	Industrial communications and sensing.
PS (Polystyrene)	Industrial short-haul communications and sensing
PC (Polycarbonate)	Industrial communications and sensing
CYTOP (amorphous fluorinated polymer)	Local Area Networks (LANs)
PCS (Plastic clad silica) and HCS (Hard core silica)	Communications, medical, industrial and sensing

POFs can be used in a wide range of applications, and their attenuation will depend directly on the material used for its fabrication as well as the refinement of the fabrication process. Table 2 shows the most common optical properties of POF such as attenuation, numerical aperture, as well as the usual core diameters used for their application. POF can use different materials as cladding such as Polyfluoroalkyl methacrylate or Polyolefin-based materials[50,51].

Table 2. Optical properties of POF[49].

Material	Attenuation [dB/km]	Bandwidth [GHz*km]	Refractive index core/cladding	NA	Core diameter [μm]
PMMA	55 (538nm)	0.003	1.492/1.417	0.47	250-1000
PS	330 (570nm)	0.0015	1.592/1.416	0.73	500-1000
PC	600 (670nm)	0.0015	1.582/1.305	0.94	500/1000
CYTOP	16 (1310nm)	0.59	1.353/1.34	0.19	125-500
PCS and HCS	5-6 (820nm)	0.005	1.46/1.41	0.38	110-1000

There are different methods and materials to fabricate POFs[52]. PMMA is the most widespread material used to fabricate POF; however, there are other options such as Elastomers (EOP), Cyclic-olefin polymers (TOPAS and ZEONEX), Deuterated polymers, Amorphous fluorinated polymer (CYTOP), PS, and PC[2,46]. The materials used to coat the POF plays an important role to improve the mechanical properties such as resistance to compressive load and tensile strength. Materials commonly used for this purpose are; Polyvinyl Chloride (PVC); Polyethylene (PE) for applications with temperatures between 70˚C to 90˚C; and Polyamide (PA); Fluorinated ethylene propylene (FEP) and Polytetrafluoroethylene (PTFE) for high temperature applications[46].

The variety of manufacturing methods in POF is as diverse as the materials for their fabrication. POF can be produced from a preform draw similar to the conventional process for silica optical fibres, but it can also be fabricated direct extrusion or through more complex processes including the polymerisation stage[52]. Batch extrusion and polymer cross-linking are examples of direct polymer formation processes for fabricating POF[46].

Improvements in the materials and novel designs such as cable production and microstructure polymer fibres MPOF have been studied in the last couple of decades. The first MPOF was reported in 2001 by Eijkelenborg[53] where the optical fibre was drawn from a preform. Extruded PMMA was used for single mode optical guidance in multiple rings of air-hole structures. Additionally, MPOF can be fabricated at a much lower cost than MOF, FBG and PCF[53] with a wider variety of cross-sections.

2.3 Additive Manufacturing

Additive manufacturing (AM) refers to a process where an object is built layer by layer using a 3D model from a CAD file[54]. This technology is also called 3D printing or rapid prototyping. AM has recently been introduced to the domestic market thanks to the success and availability of the extensive selection of low-cost 3D printers.

The concept of AM dates back to the 1980s when Hideo Kodama published the first scientific papers on the subject in 1981[55]. The oldest patent on record of a 3D printing system was filed in 1984[56,57] and only months later the first commercial 3D printing system, which expanded the rapid prototyping (RP), was developed by 3D Systems Inc[58].

In the 1990s, the interest in AM technology grew rapidly, and additional systems and methods for RP were quickly developed. This opened up opportunities to introduce other manufacturing techniques such as extrusion and laser printing. However, the materials employed for these processes were the main limitation of this technology in the early 1990s. One turning point in the development of AM was in the 2000s, when the patent of the fused deposition model (FDM) system, held by Stratasys, expired. Since then, several new companies emerged using this technology, which caused the price of FDM equipment to drop from $10,000 to $1,000 or less for domestic printers.

Additive manufacturing systems have gained significant interest in the field of medicine because they have the capability for building objects with complex shapes that can be used as a tissue scaffold using biocompatible materials[59]. Thus, AM methods are constantly developing with trialling new materials that are able to fulfil the requirements for an application with the potential to be transferred to industrial scale[60].

This technology presents advantages over conventional manufacturing processes such as the possibility to build complex shapes with practically no restrictions on the designs or the shapes that can be made. Moreover, the process is versatile, allowing quick changes during the fabrication from one piece to another if necessary, reducing time and costs. Additionally, AM enables researchers to obtain the pieces they require by enhancing product performance through the combination of different materials. All the advantages of AM are possible due to the large variety of equipment that is now available.

Since the first prototype emerged in the 1980s, different 3D printing techniques have been developed, and the majority started in research facilities. Once the process is fully developed, the technology is launch to the market. The quality of the production is regulated for ASTM standards, and the printing method is classified by ASTM into seven categories[54].

Table 3 shows the ASTM classification, listing the seven categories with a brief description of the processes and the materials that can be manufactured by each of these methods. In addition, some of the currently available brands on the market are added according to their category.

Table 3. AM categories by ASTM designation: F2792-12a.

Categories	Description	Materials[9,61]	Equipment in the market
Binder jetting	Liquid bonding agent is selectively deposited to the bed of powder materials.	Polymer, Metal, Ceramic	3D system, ExOne, Z-corp.
Directed energy deposition	Thermal energy is used to fuse materials by melting as they are being deposited.	Metal	Insstek
Material extrusion	Material is selectively dispensed through a nozzle.	Polymer	Stratasys, MakerBot, Ultimaker, ABB, UP, Makergear, DeltaWASP.
Material jetting	Droplets of build material are selectively deposited.	Polymer	Objet, Solidscape, 3D system
Powder bed fusion	Thermal energy selectively fuses regions of a powder bed	Metal, Polymer	3D system, EOS
Sheet lamination	Sheets of material are bonded to form an object	Paper, Plastic, Metal	Mcor
Vat photo-polymerisation	Liquid photopolymer in a vat is selectively cured by light-activated polymerisation	Resins, Polymer resins	3D system, Envisiontec

The use of polymers in 3D printing processes is widely developed due to the characteristics and properties of the materials. The low melting temperature, low cost, commercial availability and wide potential for recycling are among the attractive features most of the polymers exhibit. Fused deposition modelling (FDM) has gained popularity in the market due to its accessibility and the option to use a wide range of new materials with low melting temperatures during extrusion.

Other methods have been developed to produce solids via 3D printing of polymers aiming to achieve high mechanical performance and chemical resistance of the final part[62]. Although 3D printing methods such as selective laser sintering (SLS),

stereolithography apparatus (SLA) and selective laser melting (SLM) were initially developed for polymeric material, they were rapidly adapted to process other types of materials such as metal and ceramics. These new manufacturing processes were developed to fulfil specific requirements in industries such as aerospace, automotive as well as medicine[63].

The use of lasers as a source of thermal energy has enabled more precision and quality in AM processes. Direct metal laser sintering (DMLS), SLM, SLS, direct metal deposition (DMD) and SLA are 3D printing techniques used for complex materials such as metallic alloys, and some composites[63,64]. Furthermore, laser technologies in AM opened the window to a new era in material processing. The use of these technologies enabled the possibility of delivering the final product instead of printing prototypes. The laser beam acts either as heat or photo-catalytic source, depending on the printed material and the specific printing technique[58]. The high precision that a laser offers is a desirable feature that will be explored for 3D printing glass in the present work.

2.3.1 Additive manufacturing of ceramics.

In contrast to polymers and metals, ceramics have presented a challenge for AM processing due to their extremely high melting point and their intrinsic material properties such as viscosity and surface tension. Some of the AM methods that have been used for ceramics are direct extrusion, polymerization, direct writing-based process and laser-based processes[65]. In this section, the methods that have been used for AM processing of ceramics are explained. Their features, methodology, advantages and drawbacks of these techniques are discussed.

The effort to fabricate ceramics using AM has been driven by the industrial need for automotive, aerospace and biomedical applications[66]. This section; however, will focus on, the state of the art of AM processes for glasses such as quartz silica (SiO_2), and soft glasses such borosilicate, soda lime and chalcogenides that can be used for optical applications

As all AM methods, ceramics are printed on the principle of 3-dimensional models fabricated layer by layer, from a computer-aided design (CAD). The model is sliced in 2-dimensional cross-sections areas, and the entire part is produced. However, 3D print ceramic parts comprise multiple steps before the final good is obtained. The post-printing processes of 3D printed ceramic green bodies will be described and explained for each listed AM method.

2.3.1.1 Powder Bed Fusion

Powder bed fusion method (PBF) uses thermal energy over a powder bed, fusing the powder particles selectively and forming the desired layer from a 3D CAD design. The heat source commonly used in this process is a laser beam. The selection of the laser beam will depend on the wavelength and power required by the material to be processed[63]. Additive manufacturing (AM) processes based on laser technology have become more important in the market in recent years due to the versatility, repeatability and quality of the 3D printed parts[67].

The powder bed fusion printing system comprises of a powder-feeding system, which spreads the powder in a homogeneous layer of the desired thickness using a transversal roller. Once the powder bed is set in the building chamber, the powder is pre-heated to remove potential moisture in the material, before being exposed to the laser beam. The laser scans the surface of the deposited powder bed, following the CAD model. The process is repeated sequentially to build the desired structure layer by layer. This process might require a controlled atmosphere for safety or quality purposes, depending on the processed material. A schematic of a LPBF process is shown in Figure 6.

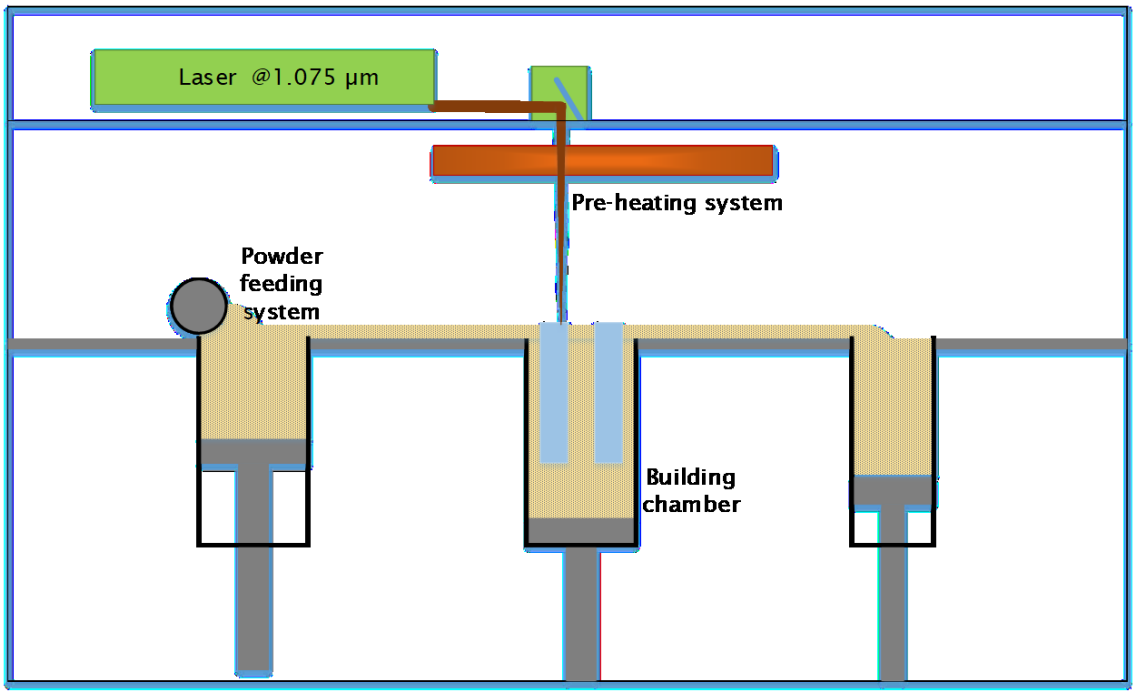

Figure 6. Schematic of a selective laser sintering system.

In PBFmethod, the binding of the powder particles, induced by a laser beam, can be partially or fully melted. Some authors have classified this AM method according to its binding mechanism. This classification can be as simple as sintering and melting, where sintering refers to a partial melting process (solid-state sintering)

while melting refers to a full melting of the powder (liquid-state melting)[61]. However, more complex classifications have been given in an attempt to include all variations of PBF. *Kruth et al*. (2005) classified LPBF in four categories[68]:

- **Solid-state sintering**, which is a thermal process that occurs at temperatures between $T_m/2$ and T_m, where T_m. In this case, the powder is exposed to a low intensity laser beam for a long time, providing the necessary energy to the system for neck formation between the powder particles.

- **Chemical induced bindin**g; which refers to a LPBF, where a chemical reaction occurs in the processed material, adding a third element in the fabrication process such as N_2 or O_2.

- **Liquid-phase sintering**; which refers to a process, where a binder and a structural material are combined. This uses composited materials, such as metal-metal or metal-ceramic. In this process, the binder material is fully melted while the structural material does not necessarily reach its T_m.

- **Full melting;** in this case, the powder particles are molten in the printing process to produce a full dense object and avoid post-processes. This process is used mainly for polymers and metals.

Multiple variables can directly affect the quality of the final solid during the laser powder bed fusion (LPBF) process[69]. These variables can be grouped according to material characteristics (physical and chemical) and optical characteristics (wavelength, power laser, speed scan). The interaction of these characteristics will result in the thermal response within the material and the final density of the printed solid. Physical characteristics of the powder include its flowability and bulk density, which have a direct correlation to the particle size and its morphology[70]. Improving the dispersion of the powder particles reduces the possibility of defects in the final printed solid.

The optical characteristics of the power will affect the energy density necessary to heat the material. Some other essential aspects of the LPBF process that must be controlled are the stress between layers due to the material shrinkage and the crystallisation of the material. These can be controlled by printing parameters such as laser power *(P)*, scan speed *(v)*, layer thickness *(t)*, hatch distance *(h)* and printing

pattern. The energy per volume of each scan *(E)* is a function of the parameters, as it expressed in Equation 1.

$$E = \frac{P}{v * h * t}$$

Equation 1. Volumetric energy density.

The LPBF printing method can be used for a wide range of materials such as polymer, ceramics, metal, alloys and composites[71]. As already explained, one of the main challenges in AM is the processing of ceramics. In 2004, *Klocke et al.* [72] reported borosilicate glass printed using SLS, and 3D printed glass has become a primal subject for research groups around the globe ever since then. In this section, some research in PBF methods for glasses are discussed, as well as their advantages and potential drawbacks for optical fibre fabrication. In addition, the discussion in section 2.3.2 explains how this technology has been used for the fabrication of optical components along with other AM methods[73].

One of the first reported 3D printing methods for glass was developed in 1997 by *Wang, H. et al.* at the University of Texas[74]. In their experiment, they used fused quartz powder to produce a 3D printed part using selective laser sintering (SLS). They used a CO_2 laser beam at a wavelength of 10.6μm with a spot size of approximately 600μm. In this work, the morphology and particle size of the quartz powder was analysed, and it was found that spherical powder with a particle size between 30 to 60μm produced 3D printed parts with better density and smooth appearance. These results opened up the possibility to process glass with a low power laser using fused quartz.

The use of low melting temperature glasses has also been explored with the laser sintering process. *Klocke F. et al.* reported in 2004 3D printed borosilicate glass, using powder with a particle size of 30μm[72]. The impact of different printing parameters in the final part was explored in this work, mainly focusing on the density and roughness of structure. It was found that low laser power, low scan speed and a hatch distance of 0.18 mm produced printed parts free of thermal stress and cracks. They also reported the results from thermal post-processing, which increased the density of the printed glass. They found that the full density of the part can almost be reached if the temperature of densification is above the softening point of the material.

Soda-lime is another soft glass that has been used for the PBF process. In 2014, *Fetari M. et al.* started to explore the potential of soda-lime glass for a selective laser melting (SLM) method[75]. The process was carried out using a fibre laser at a wavelength of 1070 nm with an average power of 60W. The parts produced by fully melting the material achieved a density of 99%. After several experimental alliterations, they conclude that a high energy density produces bulky and deformed parts, while a low energy density produces weak bonds, causing a lack of dimension accuracy in the final part. After these initial results, Fetari and Gabhardt presented an extension of their work with soda lime glass[76]. They discussed the printing parameters and patterns used in the SLM process to produce solid parts without post-processing for densification and without crystallization in the fabricated parts. Another contribution for soda-lime glass processing, using SLM, was given by *Datsiou K.C. et al.* [77]. In their study, the authors report an energy density between 80 and 110 J/mm^3 to produce 3D printed parts with this method. The fully melted glass was used to produce complex structures with high accuracy.

The direct PBF processing presented promising results for soft glasses either using full melt or solid-state sintering methods. The final parts presented high levels of densification despite their lack of transparency. Unfortunately, soft glass such as soda-lime and borosilicate contain a high level of undesired impurities, which are detrimental for optical components in particular for optical fibres. Therefore, the process for quartz glass[78] and silica powder[79] are the most relevant material to fabricate optical fibre.

In contrast to soft glasses, silica presents higher glass traction and melting temperatures than soda-lime or borosilicate. Moreover, processing silica with a fibre laser is not possible because the wavelength of a fibre laser is transparent for silica glass. Therefore the energy is not absorbed in silica. However, *Chang S. et al.* reported an indirect PBF method (liquid-phase sintering) using doped silica with active carbon powder[80]. The authors used a fibre laser at a wavelength of 1070nm instead of a CO_2 laser beam at a wavelength of 10.6µm, which is commonly used for silica processing. The authors presented a study where the efficiency of the 1µm laser beam in the printing process for coated silica was evaluated. In addition, the impact of the carbon content in the printed solid was analysed. The printed parts were fabricated with an energy density of 88.9 J/mm^3. The authors reported porous bodies with no traces of carbon after laser processing. These results are promising for fibre fabrication due to the low level of impurities in the material;

however, the final XRD analysis showed a crystallised structure of the produced solid, which is an undesired feature for an optical fibre profile.

A transparent 3D printed silica body is a clear indicator of the amorphous nature of the glass and is therefore desired for fibre fabrication. Following this principle, *Schwager A.M. et al.* studied a modified SLS, processing silica powder at hight temperature[79]. In their study, the authors described a building chamber, which was heated to 1000˚C, where the silica powder is scanned with an energy density of 33 J/mm^3 from a CO_2 laser beam at a wavelength of 10.6µm. The printed parts had a relative density of 56% with respect to quartz silica density. The porous bodies were heat-treated at 1750˚C after the printing, which resulted in a relative density of 96%. Finally, the laser polishing process was applied, obtaining the full transparency or the silica printed part. This approach could be used for conventional preforms fabrication; however, the advantages of this technique to the current preform fabrication process still have to be analysed. Moreover, the feasibility of this method to produce complex geometries such as hollow core fibres also has to be studied.

2.3.1.2 **Direct energy deposition (DED)**

Additive manufacturing methods based on laser beam processing also vary depending on the feed material system. DED is an AM method that melts the feed material by applying a high energy density directly to the deposited material. In contrast to LPBF, in a DED printing process, the material (powder) is feed in a continuous stream deposited on the substrate instead of a pre-deposited powder bed. Therefore, the processing parameters differ from DED to LPBF processes[61].

The resolution of a DED process depends on the energy source, and the fabrication speed depends on the deposition rate. The following equations describe the control of the printed parameter:

$$Wa = AP_L t_i$$

Equation 2. Energy absorbed in a DED process.

The laser energy absorbed by the material (*Wa*) is the product of the power on the laser beam (P_L), the heat absorbed by the material (A), and the time of the laser beam on the surface of the workplace (t_i). The interaction between the spot size of the laser beam (*d*) and the scanning speed (*v)* defines the time of the laser beam at the working space.

$$t_i = \frac{d}{v}$$

Equation 3. Time of the laser beam over the working space in DED process

DED processes have also been used to produce soft glasses and quartz with a wire-fed system. In their study, *Luo J. et al*. analysed the advantages of a DED printing method above SLM method for soda-lime glass. The authors introduced for the first time a wire-fed system for glass printing, obtaining transparent glass walls with this method[81]. They optimised the process, presenting a potential 3D printing method for transparent glass[82]. Following this work, von *Witzendorff P. et al*. took this concept and adapted it to process quartz[83]. A passive fibre of 0.5mm OD with a polymer coating was used to produce a 3D printed part. The power of the laser used to 3D print these parts was 120W with an equal feed rate glass and axial velocity between 200 to 300 mm/min. In this work, amorphous glass fully dense before was used to produce the printed part. The deposition and binding between layers happened when the heat source softened the glass. However, the material was not fully melted, deferring from powder-based processing, there the fabricated part is densified forming the glass.

Another reported DED based on the liquid-phase sintering method was done by *Lei J. et al.*, using a paste compound of fused silica and polymer (HPMC)[84]. The authors combined different AM methods to produces the final printed transparent glass. First, the compound material was extruded and deposited in a building chamber; then, after the layer was finally deposited, a CO_2 laser beam selectively scanned the layer surface, melting the material. The process was repeated layer by layer until the final CAD design was completed. Even though the final printed part presented height densification without post-processing, the high content of H_2O in the compound might have added OH in the final printed glass, which is undesired for optical components.

Other 3D printing methods that have commonly been used for the fabrication of 3D printed ceramics using binders are extrusion and photopolymerization. In the following sections, we will explore these methods that have been successfully used to fabricate glasses using binders or compound materials.

2.3.1.3 Material extrusion

Material extrusion is a 3D printing method where constant pressure is applied to the material, pushing it through a nozzle. The material is deposited on a substrate at a controlled printing parameters[61].

2.3.1.3.1 Fused Deposition Modelling (FDM)

FDM is a 3D printing method based in a nozzle system. FDM is also known as fused filament fabrication, and it is an AM method that enables the construction of three-dimensional solids using primarily thermoplastic materials[85]. In FDM, like the rest of the AM techniques, the printed objects are built layer by layer from a CAD design. The fabrication process consists of an extrusion-feeding system, where the material called filament, is drawn through a heated nozzle. The filament changes from a solid to a semi-liquid state during the heating process. The softened material is then deposited superposing layer by layer, fusing each layer to the previous one. This process has a fast cooling process due to the reduced exposure time of the material to the heat source. The printed object can be a fully dense solid or use an internal scaffold to reduce the amount of material used and the processing time, which is one of the main advantages of the FDM.

FDM presents additional advantages such as a wider choice of material and equipment compared to other 3D printing techniques such as SLS, or the photo-polymerisation processes (e.g. SLA and PolyJet). Manufacturing based on FDM requires the control of critical parameters in the process to achieve a successfully printed body. These parameters can be divided in a) the feeding mechanism parameters (nozzle, printing head, gantry and the building surface); b) the process parameters (building temperature, bead width, air gaps and raster operation)[86]. The polymers most commonly used in FDM are acrylonitrile butadiene styrene (ABS), polylactic acid (PLA), PC, high-density polyethylene (HDPE) and polyethylene terephthalate – ethylene glycol (PET-G). More recently, novel materials have been developed for being processed with this 3D printing method such as carbon fibre and even some high viscosity substances and polymer composites[87].

Although waveguides and optical fibres have been explored using commercially available materials such as ABS, PC, PETG, PLA, those materials are not necessarily suitable for optical applications. Alternatively, PMMA[88], TOPAS[89] and other materials such as silica[90,91] and chalcogenides[92] have been trialled to produce solids for optical applications with direct extrusion methods, including direct ink writing (DIW)[93].

2.3.1.3.2 Direct Ink Writing (DIW)

DIW is a nozzle-base printing technique, where the composite ink is extruded through a nozzle in a controlled pattern. The material is solidified by evaporation, gelation or heating, depending on the ink features. The careful control of the ink composition and the printing parameters allow the creation of intricate scaffolding structures with this 3D printing method[93]. In contrast to FDM where the nozzle is heated to soften the extruded polymer, DIW works with low-temperature processes or even at room temperature.

Some of the more controllable and accurate printing methods for SiO_2 were done using a colloidal ink with a DIW printing system. Lewis J. presented the design and analysis of a silica gel consisting of in micro-spherical silica coated with poly(ethylenimine), suspended in deionised water[93]. In this study, it was demonstrated excellent control of the deposition process, the uniformity of the printed lattice and the capability of shape control of a silica compound. This experiment opened up the opportunity to fabricate silica printed parts with this method. However, until this point, no transparent glass had been printed using a composite material without a laser-based process. It was *Nguyen D. et al.*, who presented the first experiment using a composite gel to extrude a silica green body using hydrophilic silica powder[90]. In this work, the silica was mixed at 20wt% with PDMS polymer and a solvent with a high boiling point called tetraglyme. The compound was deposited layer by layer by extrusion method at room temperature. Finally, the green body was heat-treated in three stages: removing the solvent, burning the non-organic components and final densification of the printed part. The limitation of this method was the achievable size of the final parts, which presented a drawback for further studies to print transparent silica parts using compound materials. In an attempt to tackle this drawback, stereolithography (SLA) has been studied using silica compounds with photocurable polymers.

The research mentioned above does not include a feasibility study of the FDM process using these materials for optical preform fabrication; hence this will be discussed in section 2.3.2. Chapter 6 discusses the optical fibre fabrication using FDM and in Chapter 5 discusses the DIW technique.

2.3.1.4 Photo-polymerization

Additive manufacturing using the photo-polymerisation method consists of a process, where a photosensitive resin is hardened with a UV source. Different well-

developed techniques use this 3D printing method such as SLA, digital light processing (DLP) and PolyJet. All these systems initiate the curing process of the resin (polymer) by activating the photosensitive radicals that initiate the cross-linking process of the polymeric chains that harden the resin. The difference between the abovementioned techniques lies in the resin feeding system and how the UV light source exposes the printed part.

SLA was developed in the 1980s, and therefore it was the very first AM technology[9]. Nowadays, the SLA process generally includes a UV laser beam that is focused into a photo-curable resin. The UV laser is used to draw a design from a native file format of the stereolithography CAD software (STL). The UV beam shapes the part by scanning the surface of the photopolymer. This process is sequentially repeated for each layer, and the solidified 3D model is then surrounded by uncured polymer that stays in the resin container, creating support for the printed solid. Once the model is completed, the printing platform moves out of the vat, and the excess resin is drained. Finally, the printed solid is cleaned to remove leftover resin on the surfaces.

The DLP process follows a similar principle to the SLA process. The feeding system consists of a tank where the photosensitive resin is also scanned. The difference between these techniques lies in the delivery method of the UV source. The DLP printer uses a digital projector screen, while the SLA use a laser source. DLP has a lower surface quality that can compromise the appearance of the final part.

The PolyJet process differs from the SLA and DLP in terms of the material feeding system and the curing principle. On PolyJet printers, a UV light tracks the feeding system and cures the resin material, as soon as it hits the part. The laser source and the feeding system move together on top of the building platform. This can create solids with a minimum surface roughness of the printed parts. The quality is similar to SLA printing technique.

Many equipment manufacturers have developed their systems and processes based on their resins developments. Monomers, oligomers and photo-initiators are the necessary components of the resins used for these processes. Modifying these components can provide specific properties to the material such as strength, transparency, flexibility, and chemical and thermal resistance. This represents an opportunity to develop materials with optical properties. Develop a compound, mixing nano-particulate silica with photopolymers, can be processed either using SLA, DPL and PolyJet techniques, with the possibility to 3D printing transparent

solids. *Kortz F. et al.* presented for the first time a photocurable composite to print silica parts[94]. The photocurable resin content nanoparticles of silica powder dispersed with a monomer. The compound was exposed to a UV light by a stereolithography (SLA) printing process. The printed green part was heat-treated to remove the non-organic parts of the composite, and the sintering process occurred at 1300˚C, forming a transparent glass. In an attempt to increase the silica content in the compound and improve the mechanical properties of the 3D printed parts, *Shukrun E. et al.* developed a complex sol-gel compound based on silicon alkoxy and monomers and photopolymerisable acrylate[95]. After a gelation process, the compound was exposed to UV light in a stereolithography printer. The produced green body was left at room temperature for the final curing of the object. This compound presented better mechanical properties of the printed parts; however, due to the high content of impurities, it was not suitable for optical applications.

2.3.2 Additive manufacturing for optical applications

The application of AM technology to produce optical components has been pursued for the last decade. One of the earliest examples of a 3D printed solid in this sector was designed for a terahertz plasmonic waveguide[96]. An SLA process was used to print a U-shape structure, which was sputter with Au. THz frequencies were used to measure the waves on the surface of the metal. Other works using 3D printing for optical components are period gratings by extrusion method[97], planar waveguides by photopolymerization[98], lenses by extrusion[89] and optical fibres.

One of the most common approaches to produce optical fibres by AM is to fabricate polymer preforms by FDM, followed by a drawing process[99]. There have been some published works related to print polymer preforms in a single material and using multiple materials. The first demonstrations of 3D printed polymer optical fibre (POF) were done by *Cook K. et al.*, in 2015[11]. A 3D printed preform of styrene-butadiene-copolymer and polystyrene (SBP) was produced using an FDM printer. The preform was drawn to a high multimode PCF, which was characterised, showing a low transmission level in the NIR region. Later, a double material preform was fabricated by an FDM. SBP and PET-G polymers were used to produce the preform, which was drawn to a high multimode step-index POF. The fibre was characterised in the visible and NIR regions[100]. The printing pattern of the produced polymer fibres was analysed, and the modification of a symmetrical pattern was proposed

by *Wang Y. et al*.[101]. the modification on the printing pattern can reduce the fibres losses and improve the transmission.

The strength of AM processes over conventional fabrication method for optical fibres is the possibility to produce complex geometries with a high level of accuracy and repeatability. Therefore, many attempts to produce optical fibres with complex geometries, such as microstructure fibres, have been perused. *Talataisong w. et al*. reported the fabrication process of microstructured polymer optical fibres (MPOF) from 3D printed PETG preforms[102]. The analysis of the drawing process of a MPOF is presented in this works, as well as the fabrication of the preform by FDM method.

Other attempts to produce hollow core waveguides were made using varied printing techniques. A hybrid material waveguide was studied by *Yudasari N. et al.,* by using metal wires embedded in the polymeric cladding printed by a photopolymerization method[103]. Polymer antiresonant fibres (PARF) has also been produced by extrusion (FDM). *Zubiel M. G. et al*., presented a fabrication method of PARF drawn from a 3D printed poly(methylmethacrylate) PMMA preform[88].

A key factor to the fabrication of optical fibres by any AM method is to measure the performance of the fibre. Therefore, the transmission of hollow core polymer waveguides in the THz region has been studied. The waveguides have been designed and characterised by THz-time domain spectroscopy (THz-TDS). A waveguide based on Kagome photonic crystal structure was produced by photopolymerization in a thermoset material[104]. *Cruz A. et al.* studied the attenuation in other antiresonant and Bragg waveguide designs, which were produced by FDM in Acrylonitrile butadiene styrene (ABS) polymer[105]. Van *Putten L.D. et al*., produced 3D printed antiresonant waveguides in polycarbonate by FDM[106]. The effect of the wall thickness in the attenuation of the waveguide was analysed.

Optical fibre fabrication by 3D printing methods has been mainly explored in polymer materials due to its accessibility. However, more recent research studies have been explored to use 3D printed silica for optical fibres[107]. The leading 3D printing methods that have been used to fabricate silica optical components are photopolymerization[108,109], lased-based methods[110-112] and extrusion[113-115].

Chapter 3 Development of Laser Powder Bed Fusion (LPBF) for SiO_2

As discussed in Chapter 2, the current optical preforms and fibre fabrication processes face challenges that need to be addressed in order to satisfy the increasing demand for innovative designs based on complex geometries and multiple materials. In this chapter, a laser-based printing process is explored as a potential 3D printing method for glass with optical properties suitable for optical fibre fabrication.

Even though there are several studies of laser-based printing processes for metals and polymers, this manufacturing method is new for silica powder, and a deeper understanding on the effect of the laser in the material is needed before a complete structure can be produced. Therefore, the full development of laser powder bed fusion (LPBF) process is described and discussed in this chapter.

As a result of initial experiments with a 60W CO_2 laser, operating at a wavelength of 10.6μm, the basic parameters for a successful LPBF process were defined. The information obtained from these experiments also provided crucial information for the development of a custom-made apparatus for a laser-based printing process.

In this chapter, it is also presented the fabrication development of 3D printed silica porous bodies using the LPBF process. The experiments were divided into three stages: single lines, single areas and volumetric structures. The followed methodology is reported, and the results are discussed in every section. In addition to silica, the process was also trialled with multi-materials using a mixture of silica with germanium dioxide (GeO_2), demonstrating the viability to produce doped preforms and fibres with this method.

In addition, printed bodies were densified through heat treatment, reaching quartz silica density. The conditions for the densification process are described in section 3.8, and the analysis of the obtained glass are discussed.

3.1 Silica powder characterization

The first stage of this analysis focused on the selection and characterisation of the raw material. It is well-known that commercially obtained powder will have lower levels of purity compared to the materials that can be obtained by a chemical

vapour deposition (CVD) processes. It was essential to select a silica powder that has the lowest impurity levels and fulfilled the mechanical properties for the laser powder bed fusion (LPBF) process, as shown in Chapter 2. Flowability is the most critical mechanical property of the powder, which is critical for the homogenous distribution of the powder in the building chamber. The flowability of the silica powders was measured by obtaining the angle of repose.

The angle of repose is a characteristic related to the interparticle friction or resistance to movement between particles[116]. The funnel method was used to measure the angle of repose of silica powders. The technique uses a funnel with a wide outlet, where the material is poured through, such that the material forms a cone. The angle of the resulting cone is the angle of repose. It can be calculated by the inverse tangent of height divided by half of the base width of the cone. This technique is widely used to measure the angle of repose of dry powders in the industry such as micro and nanoparticles in nanomedicine or powder for additive manufacturing.

Equation 4 was used to calculate the angle of repose (θ), where the diameter of the cone (D) was constant (20mm), and the distance between the base and the deposited powder peak (h) were measured with a ruler, as is shown in Figure 7.

$$\theta = \tan^{-1}\left(\frac{h}{\frac{1}{2}D}\right)$$

Equation 4. Angle of repose.

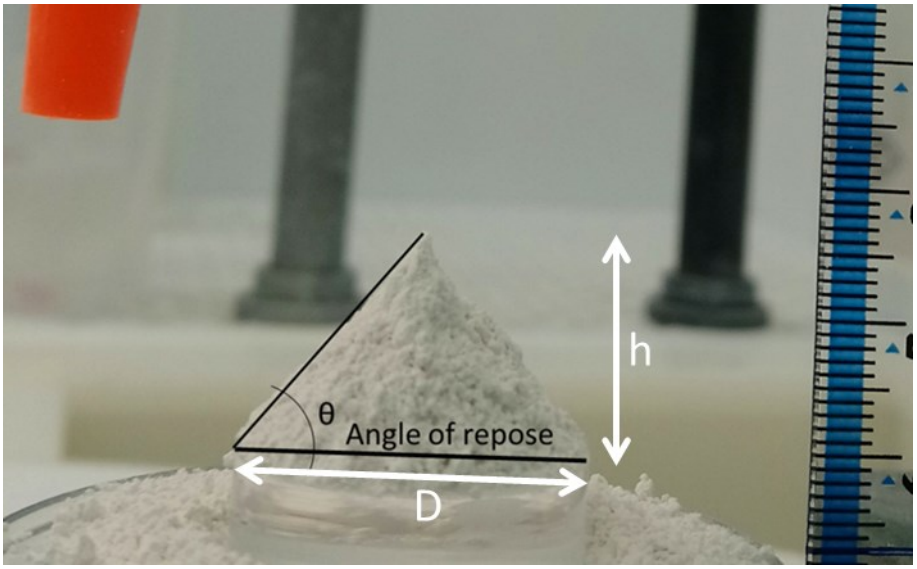

Figure 7. Schematic of the experiment of the angle of repose.

The relationship between flowability properties and the angle of repose has been established[116,117]. When the angle of repose is less than 25 degrees, the flowability is said to be excellent; on the other hand, if the angle of repose is more than 40 degrees, the flowability is considered to be poor. As larger the angle of repose, the sticker the material, and the lower, the material presents better flowability in the deposition bed.

The angles of repose of various silica powders with different particle sizes and morphologies were measured. Table 4 shows a summary of the silica powders characterised with this technique and their correspondent angle of repose. The particle size reported in the table corresponds to the supplier datasheet.

Table 4. The angle of repose of SiO_2.

SiO_2 particle size [µm]	Particle shape	Angle of repose [degree]
10	amorphous	52.30
44	amorphous	35.87
150	amorphous	34.79
2	spherical	44.23
5	spherical	55.50
15	spherical	55.09
30	spherical	22.02

Figure 8 shows the angle of repose of amorphous silica powder with a particle size of 10, 45 and 150µm. Figure 9 shows the angle of repose of spherical silica powder with particle sizes between 2 to 30µm.

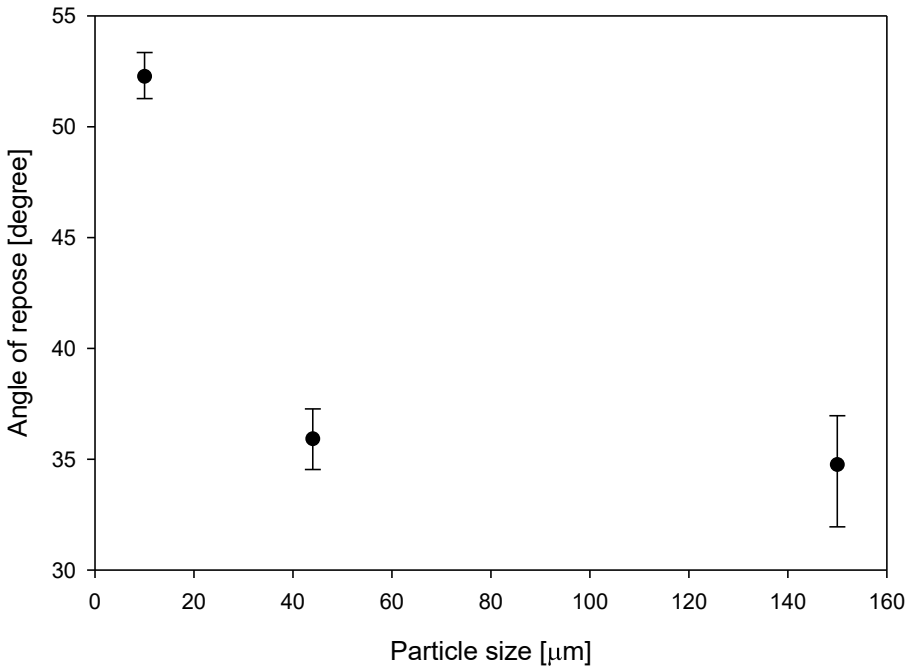

Figure 8. The angle of repose of amorphous silica powder.

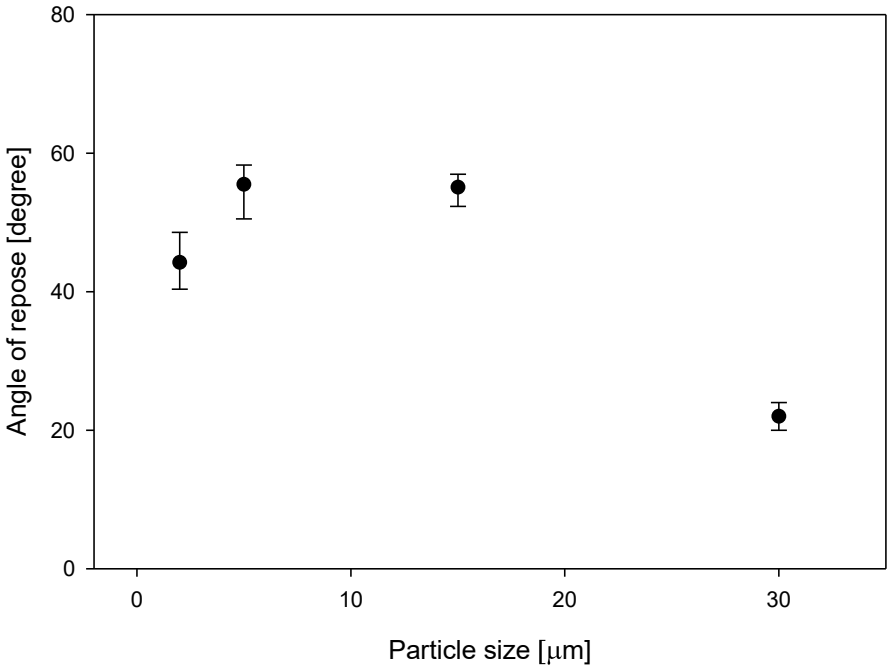

Figure 9. The angle of repose of spherical silica powder.

Following the experimental results, the powder selected to be used in our preliminary experimentation was the spherical silica powder with a particle size of 30μm, which presented an angle of repose of 22 degrees. It was found that the powder flowability does not only depends on the particle morphology, but also on the particle size. It was found that smaller particle sizes present poor flowability characteristics.

The chemical composition provided by the supplier (International Powder) of the SiO_2 powder contained Na, K, Ca, Mg, Fe at ppm level as reported in Table 5. Although these impurities are low, the powder is not considered high purity for optical fibre applications. Nonetheless, its mechanical properties make this powder the most suitable for use in the laser-based process. Furthermore, it is expected that some of the impurities can be removed during the heat treatment of the printed part.

Table 5. Silica spherical powder characteristics.

Characteristic	Reported value
Particle size [μm]	30 ±2
H_2O content [%]	≤ 0.05
Na [ppm]	≤ 20
K [ppm]	≤ 10
Ca [ppm]	≤ 10
Mg [ppm]	≤ 10
Fe [ppm]	≤ 80

The particle size distribution of the selected power was measured by image processing with an optical microscope. The samples were prepared, placing the silica powder in a microscope slide and dispersed by a solvent. Once the samples were dry, an image of the particles was analysed with a Nikon microscope. It was found that the average particle size is ~15µm. Even though the supplier reports 30µm particle size, only 4% of the powder was found to be in a range between 28 and 32 µm in size. In Figure 10, it is noticeable that 53% of the powder particles are between 10 to 20µm, and only 29% are between 20µm and 35µm. Only 3% have a particle diameter above 35 µm and 15% of the powder present a diameter below 10 µm.

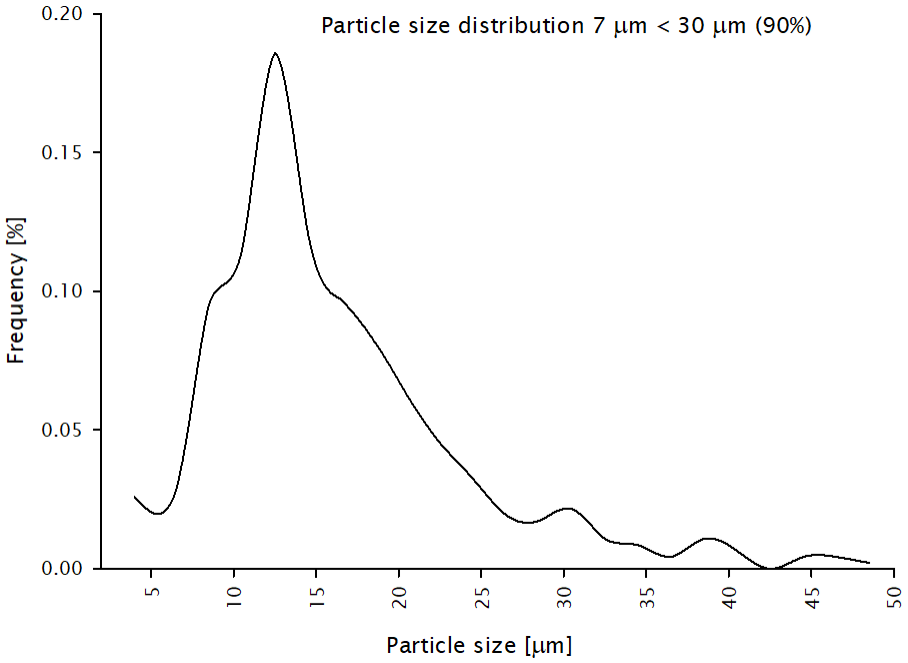

Figure 10. The particle size distribution of spherical silica powder.

The differences in the particle diameter are well appreciated in Figure 11. It shows the micrograph obtained using the scanning electron microscope (SEM) for the selected powder. The morphology of the particles is regular with a spherical shape, which is favourable for the flowability. The different particle size is expected to increase the packing powder density during the process by filling up the available gaps with smaller particles.

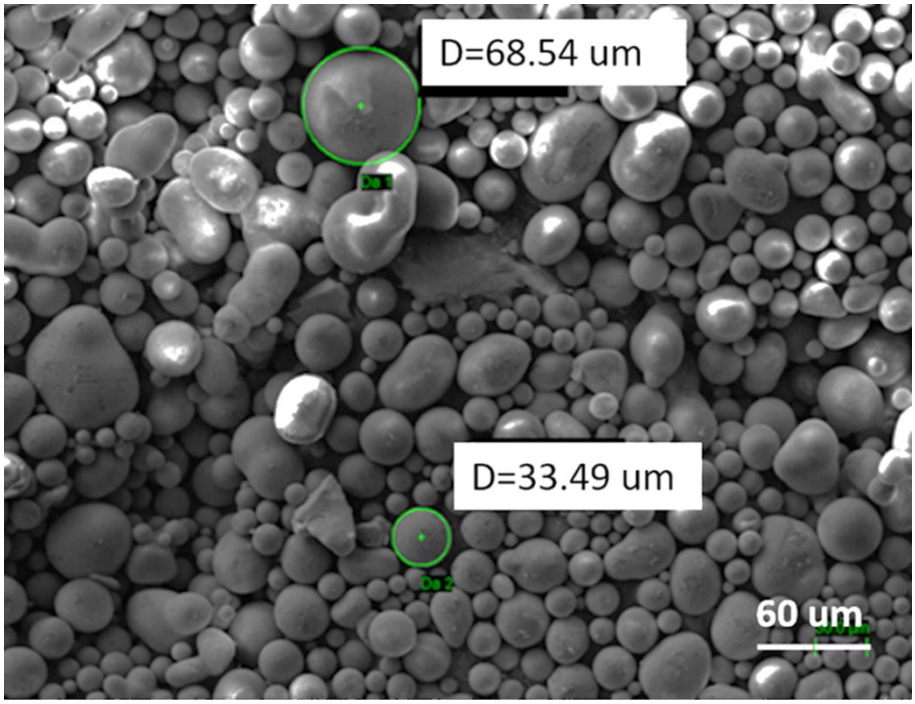

Figure 11. SEM micrograph of spherical silica powder.

Other important properties of the material that needs to be considered during the printing process are the melting point (T_m) and the glass transition temperature (T_g) of the material. In order to obtain these properties of the selected silica powder, a thermo-gravimetric analysis (TGA) of the SiO_2 powder was performed with a PERKIN ELMER TGA DIAMOND. The experimental conditions were set to a maximum temperature of 1500˚C starting from room temperature, with a temperature ramp rate of 10˚C/min in a horizontal chamber in a controlled N_2 atmosphere. A control sample of fumed SiO_2 soot obtained by OVD was also measured for comparison.

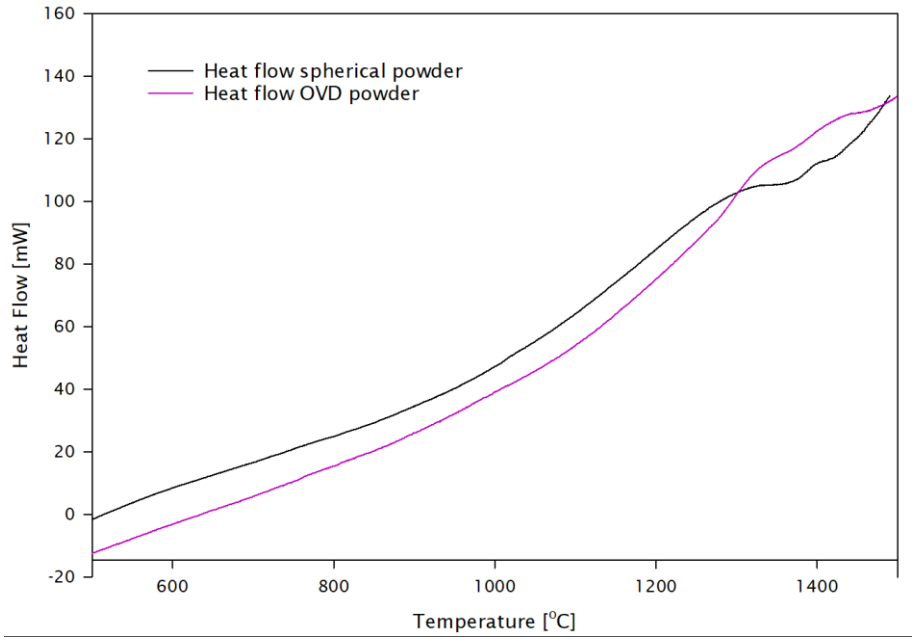

Figure 12. TGA measurement of silica powders.

Figure 12 shows both TGA curves from the spherical silica powder and OVD powder. It is noticeable that the spherical silica powder has lower T_g compared to the high-purity SiO_2 fabricated in-house using OVD. This difference is due to the impurities present in the spherical powder. This information is crucial to understand the requirements for processing the spherical powder and its difference when processing high-purity SiO_2.

3.2 Preliminary experimentation

Laser powder bed fusion (LPBF) process for silica powder is a novel additive manufacturing process proposed for 3D printing glass. Initial experiments were carried out to understand the effect of the laser beam on the silica bed surface. These preliminary experiments help to define the required energy level for silica processing with LPBF. In addition, it was possible to establish an approximation of the printing parameters for silica powder such as scan speed. Due to the absorption properties of silica, a CO_2 laser was used as a heat source to silica. This thermal processing coalesced the particles.

A custom-build experimental set up was developed using a 60W CO_2 laser with a wavelength of 10.6μm by Epiloglaser 24. The set up included a 3-axis (x, y and z) deposition stage. Figure 13 shows the apparatus used in the experiment. This simple design was used to simulate a laser-based printing process.

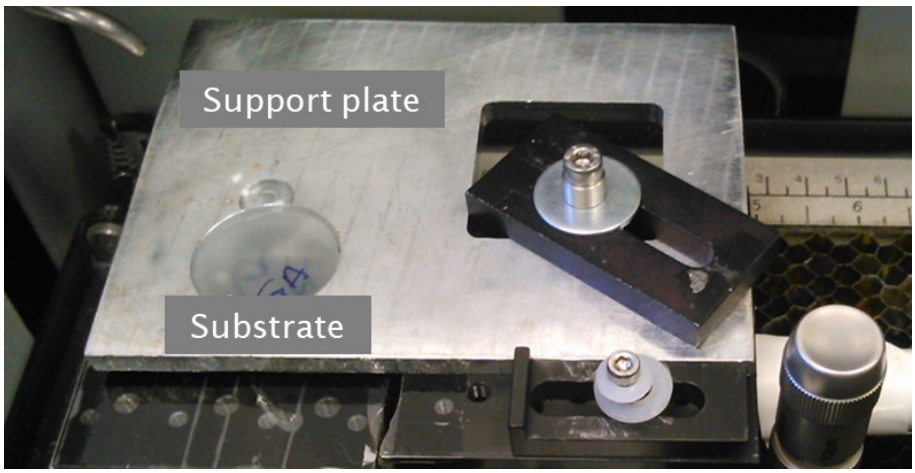

Figure 13. Experimental setup for powder scanning with a CO_2 laser.

The laser beam is collimated to a spot size of 0.075mm. The powder bed is moved in the z axis using a micrometre precision stage. An aluminium plate was designed with an opening to hold a planar glass substrate, where the powder bed is placed. The substate is resting on a base that is moved downwards. The silica powder,

which was placed on top of the aluminium plate, is fed on the substrate with a roller. This process provides a uniform SiO_2 layer thickness, as shown in Figure 14.

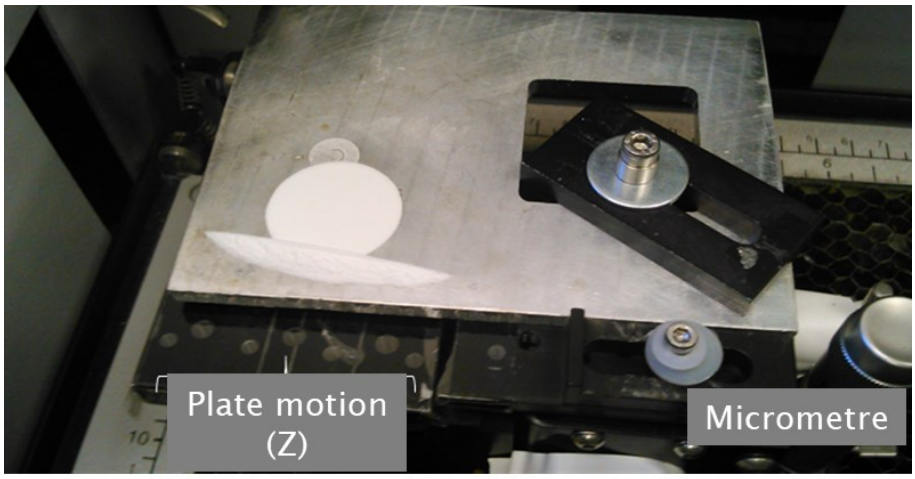

Figure 14. Silica powder bed with controlled thickness.

Finally, the laser beam scanned the silica powder surface in the x and y-axis, according to a designed pattern with a hatch distance of 200μm, as presented in Figure 15.

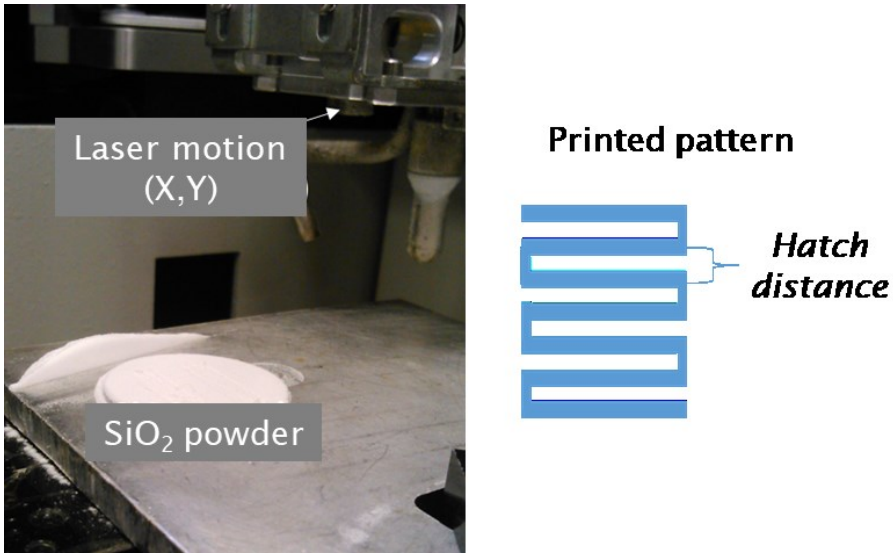

Figure 15. Laser scanning and printed pattern for preliminary experimentation.

The process window was determined based on the morphology of printed tracks. The described pattern was scanned, varying the two printing parameters: laser power from 6W to 60W and scan speed from 150mm/s to 1200mm/s.

It was observed that the applied energy in this experiment could reach the silica melting point. At higher laser power, the silica powder melted and formed droplet-like features on the powder bed. It is worth mentioning that due to the viscosity of

the glass, the molten glass does not flow as it is the case for other materials used in the LPBF process (e.g. metal and plastics).

For the specific case of silica, it is observed that the particles coalesce on a more uniform stripe-like shape and with well-defined geometries when the laser exposure is performed at low power levels, as shown in Figure 16. Figure 16a shows a ~0.300mm droplet, which is formed after scanning the silica bed surface at 500mm/s and with laser power 36W. As the laser power was reduced, a stable and well-defined stripe was achieved at a relatively low linear energy density of ~25J/m. This can be observed in Figure 16c.

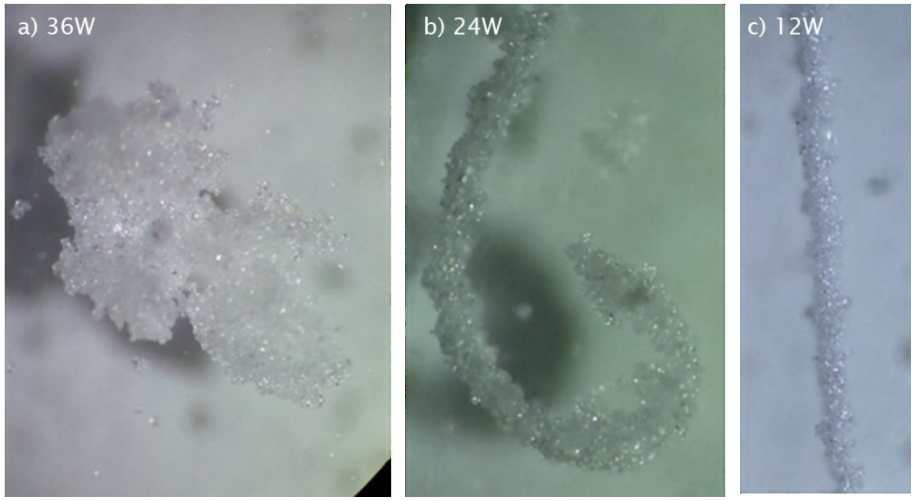

Figure 16. Silica powder scanned above 500mm/s by a CO_2 laser beam at different laser powers.

High energy densities applied on the surface of the silica powder produces large defects in the printed layer, which can result in overall low density of the printed solid due to the defects and gaps between layers during the printing process. Figure 17 shows an example of the defects present in a printed line of 0.5 mm, where the energy density is not optimised. In this case, silica powder was fully molten, and the material did not flow on the printed part.

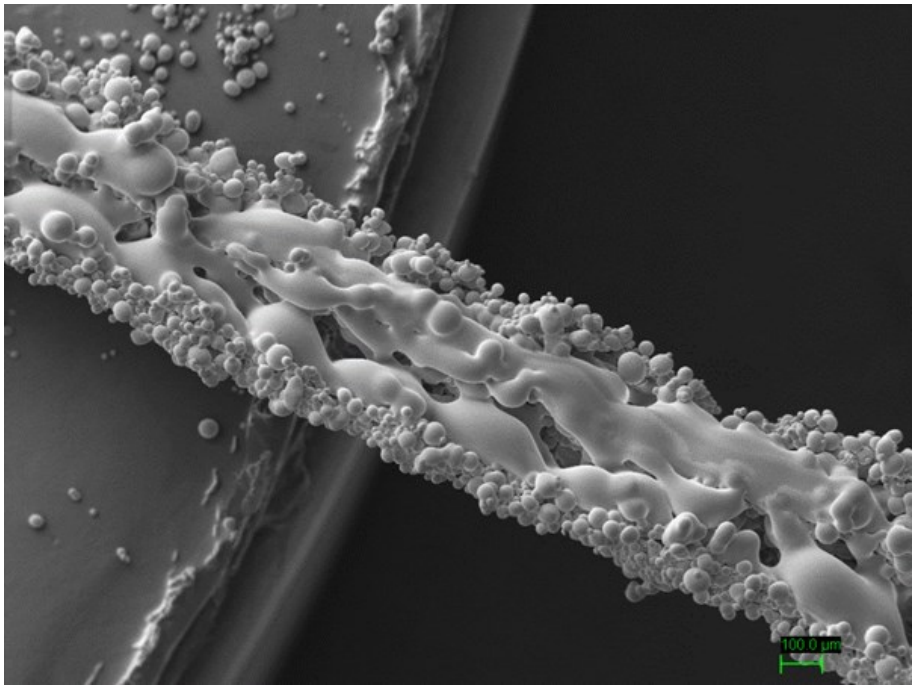

Figure 17. Stripe scanned by CO_2 laser beam without optimisation of the energy density.

These preliminary experiments showed that the scan speed plays an essential role in the amount of energy delivered to the powder surface. The experimental results suggest that the molten volume of SiO_2 powder is directly proportional to the energy applied to the surface of the powder. For longer exposure times, there is more heat diffusion, and higher melting rates in the glass are observed. Therefore, it could be possible to estimate the temperature on the powder surface and the required laser power to melt the powder, enabling defined printed layers.

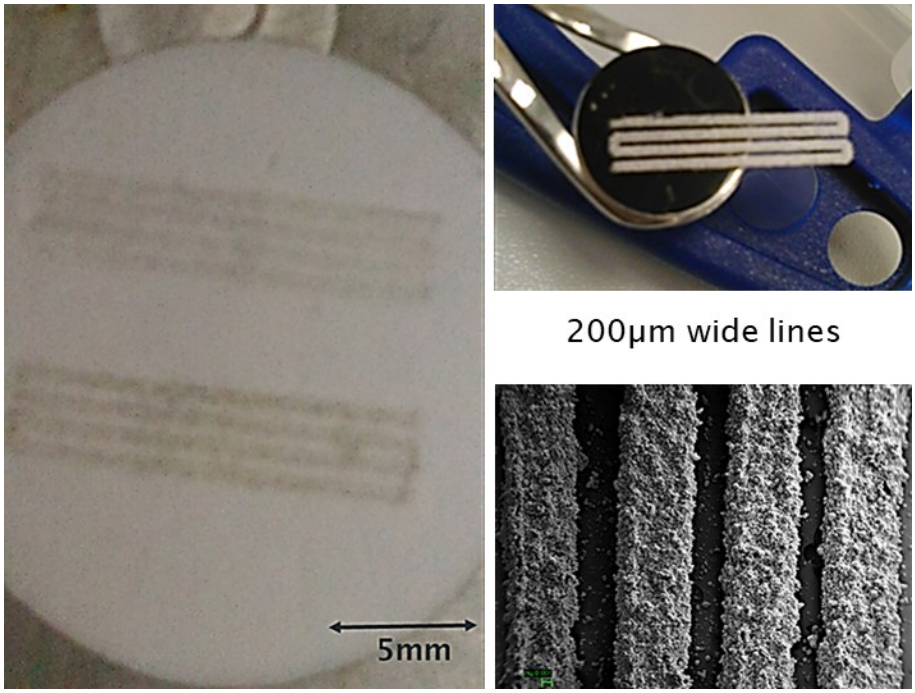

Figure 18. Single tracks using initial optimisation conditions.

As a result of the initial experiments, it was possible to print well-defined single tracks, as shown in Figure 18. Using the preliminary experimental setup, it was also possible to demonstrate the capability of this fabrication technique for printing single layers and volume structures as it is presented in Figure 19.

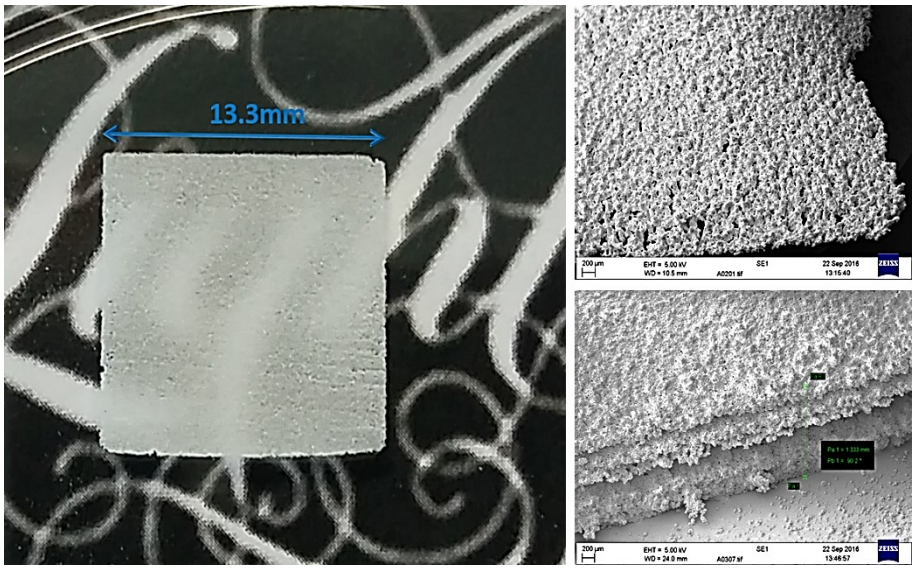

Figure 19. Single layers and volume structures using initial optimisation conditions.

The effect of the laser beam on the powder surface at different powers and scan speeds was analysed. The initial results showed the capability to print silica spherical power with LPBF using a CO_2 laser beam with a low energy density. The chosen powder presented the mechanical and physical characteristics suitable for 3D printing porous bodies using a laser-based process.

The preliminary experimentation reported in this research provided crucial information for the design and development of a new customised laser-based printing apparatus built for the University of Southampton, as is described in section 3.3.

3.3 Equipment characterisation and experimental setup

The results of the preliminary experimentation provided the starting point for the design and development of a customised 3D printing system that was built for the University of Southampton. The parameters obtained from the preliminary analysis were used as reference values for the characterisation of the new equipment, defining the laser power below 100W and the scan speed range from 10mm/s to 1500mm/s.

The multi-material additive manufacturing (MMAM) instrument, shown in Figure 20, can process a wide range of materials due to its dual laser system, which consists of a 500W CW fibre laser (SPI) with an operating wavelength of 1075-1080nm, and a 100W CO_2 laser (Synrad) with a wavelength of 10.6μm.

Figure 20. Customised 3D printing system, University of Southampton.

The laser beams are directed to the surface of the material bed using two independent galvanometer mirrors (HurryScan30 and Hurryscan20), as shown in the schematic in Figure 21.

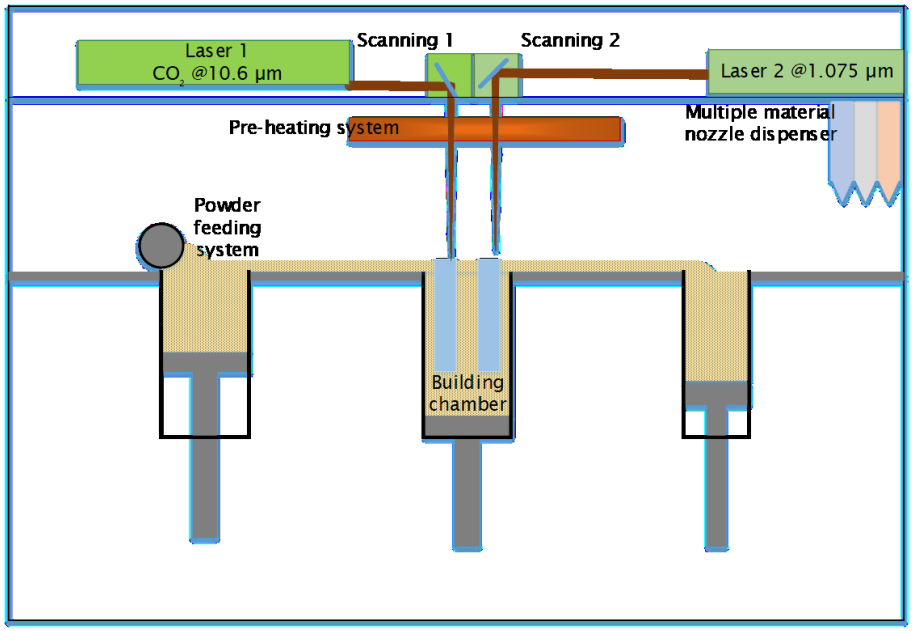

Figure 21. Schematic of the customised 3D printing system with a dual laser system.

The equipment also has a dual feeding system that can work independently to add multiple materials. The first system is a conventional powder bed feeding

mechanism, and the second system is a nozzle-based dispenser aimed to supply multiple materials. For this work, the silica powder was fed using the conventional powder bed mechanism. The system has a roller that spreads the powder from the powder feeding system to the central building chamber. Inside the building chamber, the building platform moves down one step at a time after the laser scans the surface. This process is repeated sequentially. The computer-controlled system reads the design from a STL file. Once the printing process is finished, the building platform is lifted, and the printed part can be removed.

3.4 Single Tracks

Single lines were scanned in a layer of silica powder, preheating the surface of the powder bed to 200˚C in order to remove moisture from the powder. This first trial was designed to validate the results of the experimental analysis with the new system. For this purpose, the 30µm silica spherical powder was fed into the building chamber with a roller, forming a homogeneous layer. The surface of the powder was scanned with a CO_2 laser beam with a spot size of 100µm. The regularly scanned pattern had a length of 16mm, and every track was 0.3mm wide, with a hatch distance of 1mm, as is shown in Figure 22.

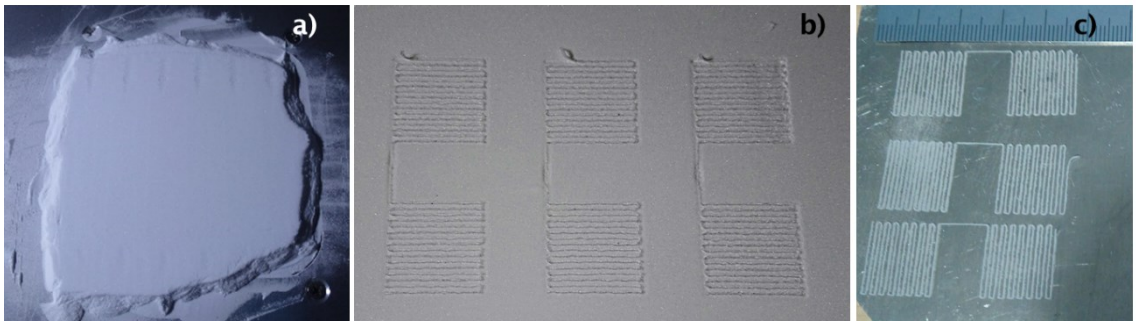

Figure 22. 3D printed single tracks in silica powder; a) powder bed; b) laser scanning; c) cleaned single tracks.

After the printing process, the width, thickness and the cross-sectional area of the printed stripes were measured. These measurements established the correlation between scan speed and laser power. With these measurements, an adequate hatch distance and layer thickness was found for this printing process.

The effect of the laser beam on the silica powder was analysed. The laser power was varied from 10 to 100W, and the scanning speeds from 100 to 500mm/s, as described in Table 6.

Table 6. Correlation of laser power and scan speed vs average width in [µm] of 3D printed stripes.

Power [W]	Speed [mm/s]	100	200	300	400	500
20		312.72	-	-	-	-
30		319.34	-	-	-	-
40		319.16	377.26	364.23	-	-
50		345.72	307.59	421.12	389.79	304.30
60		288.71	394.53	436.54	396.43	378.44
70		335.69	352.34	448.69	458.01	374.36
80		397.43	390.31	435.05	461.46	431.31
90		373.20	445.7	422.70	464.9	428.08
100		371.91	311.69	503.02	486.17	450.50

At low laser powers (<30W) and scan speeds greater than 100mm/s, the printed parts were not sufficiently mechanically stable to be taken out of the building chamber, and the parts broke during the removal process. This can be explained by the low energy density applied to the powder, which did not provide enough heat to enable a proper bonding between the particles.

The energy density delivered to the powder also has an effect on the quality of the edges of the stripes. Inadequate power can lead to mechanically stable parts with poor edge quality, which is detrimental when high-quality single tracks for planar waveguide applications are required, or when the printing process is scaled-up for single areas or volumetric structures.

Figure 23 describes the correlation between the scanning speed and the width of the printed stripes at different laser powers.

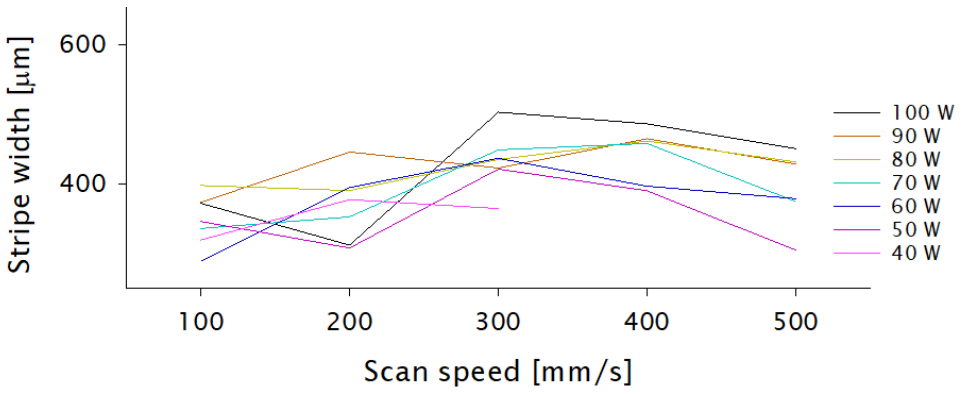

Figure 23. Stripe width as a function of scan speed in single tracks.

Figure 24 presents the standard deviation of the stripes' width, which is an indication of the edge's uniformity and their surface quality. The experimental data reveal that the stripes were more irregular, with an increase in laser power and a decrease in scan speed. It is also observed that with an increase in scan speeds, the width of the stripes becomes more regular.

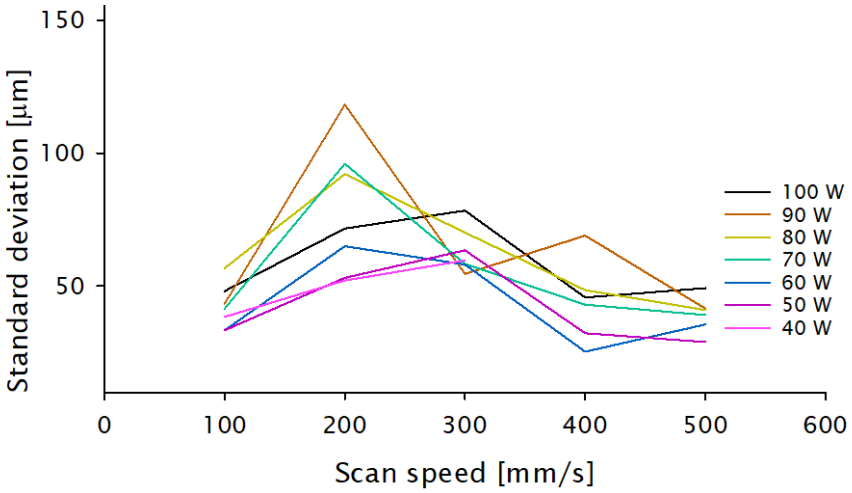

Figure 24. The standard deviation of stripes width in unidimensional structures.

Figure 23 shows the experimental results analysing the effect of the scan speed on the width and the edges of the stripes at a fixed laser power. The stripes printed with a laser power of 60W and a scan speed of 100mm/s present large irregularities on the edges resulting in the silica forming large cross-sections concave structures highlighted with the black line.

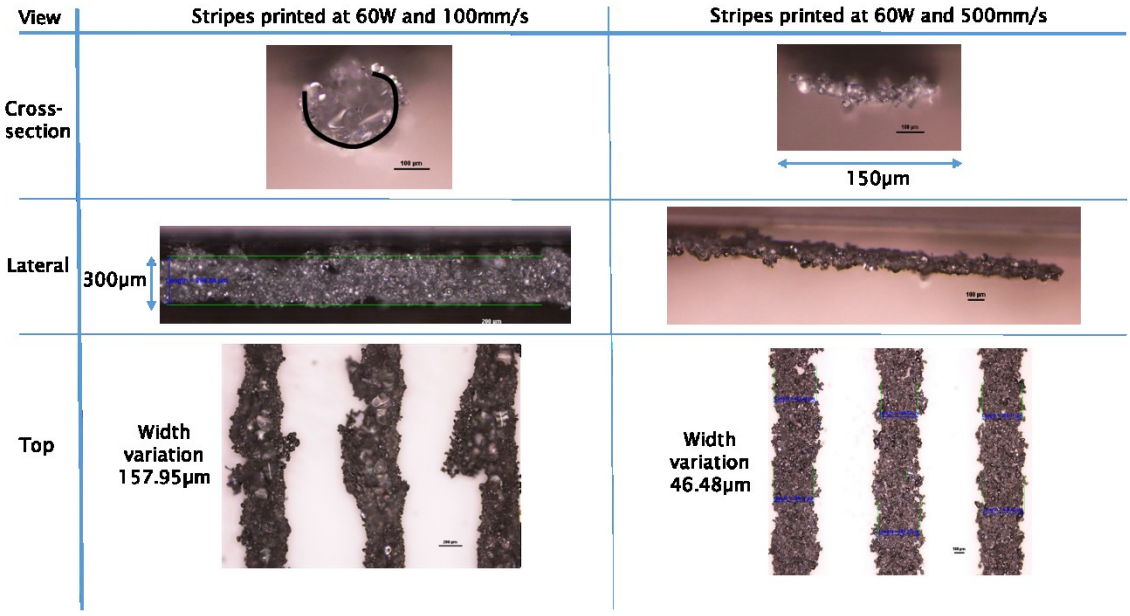

Figure 25. 3D printed unidimensional structures at different scan speeds and fixed laser power.

3.5 Single Layers

The aim of this set of experiments was to measure the effect of the laser beam on single areas of silica powder. Thus, this experiment was set up with a constant hatch distance of 200μm and variable laser power and scan speed. It is targeted to obtain a printed layer with minimum roughness and porosity. The selected hatch distance aims to get an overlap in the printing pattern to ensure adequate bonding between stripes.

The experimental setup was prepared to produce 3D printed squares with a size of 100mm^2. The laser beam scanned a homogeneous layer of silica powder in the building chamber as it is shown in Figure 26.

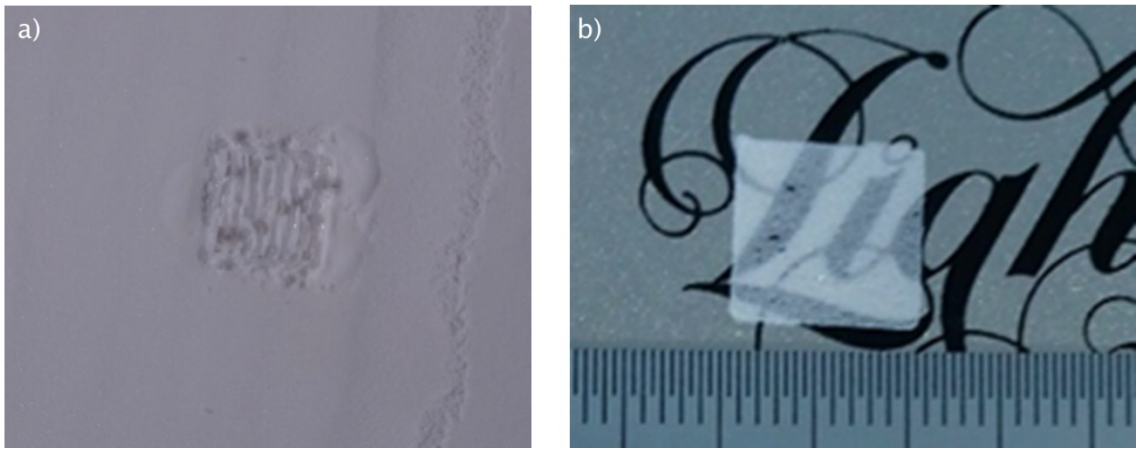

Figure 26. Silica 3D printed single layers; a) powder bed; b) cleaned single layer

The laser power was set between 20 and 100W with a scanning speed between 10 and 1300mm/s, as shown in Table 7. The thickness of the 3D printed areas was measured, and their morphology was observed using an optical microscope and SEM.

Table 7. The average thickness of the 3D printed square areas in mm, with varied laser power and scan speed.

Speed [mm/s]	Power [W]	20	40	60	80	100
10		1,461.51	-	-	-	-
50		1,012.00	-	-	-	-
100		461.91	625.45	-	-	-
300		226.38	533.00	403.96	369.28	-
500		106.15	227.21	299.88	317.10	-
700		-	103.20	144.89	203.70	314.44
900		-	-	102.81	149.50	289.75
1,000		-	-	78.28	146.80	275.10
1,200		-	-	-	-	133.20
1,300		-	-	-	-	83.24

The printing parameters aimed to find the fabrication conditions that promote a low roughness and low surface porosity in the printed body. It was observed that the quality of the surface and the roughness of the printed area improves with faster scan speeds. Layer thickness between 100µm and 150µm presented lower surface roughness and sufficient mechanical strength to keep the shape after the cleaning process. These thicknesses were reached at scan speed above 500mm/s.

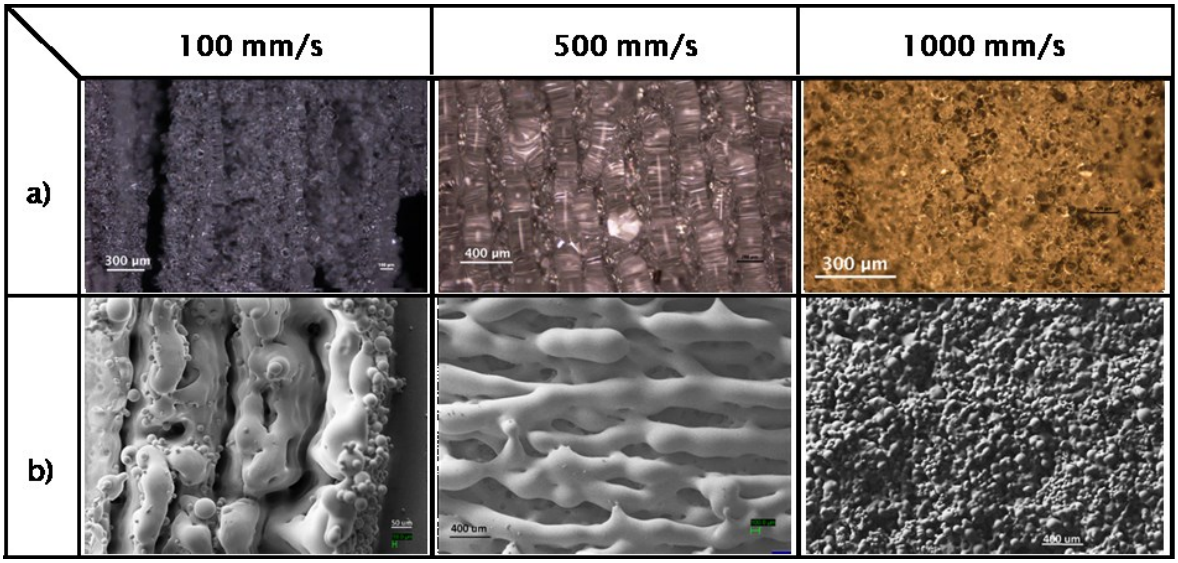

Figure 27. 3D printed single areas at different scan speeds and fixed laser power.

An example of the differences in the area surface is shown in Figure 27, where the scan speed increases from left to right. Optical microscope and SEM images of single areas printed at 60W laser power are shown in Figure 27a and b. The areas exposed with a scan speed of 100mm/s shoes more irregular surface structures compared to areas printed with a scan speed of 1000mm/s.

The thickness is correlated to the roughness and morphology of the layer. Figure 28 shows the cross-section of silica printed layers with a laser power of 20W and at three different scan speed: 10, 100 and 500mm/s. Figure 28a shows a printed silica layer thickness of 1.4cm thickness for a scan speed of 10mm/s, while the layer printed at 500mm/s, shown in Figure 28c, shows a thickness of 0.1mm.

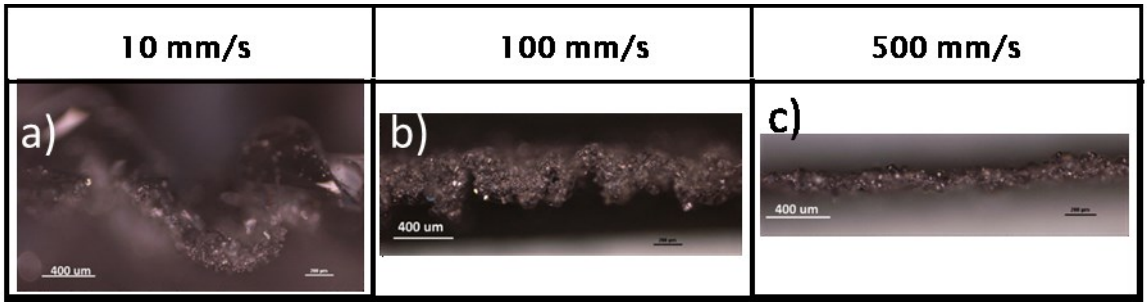

Figure 28. Cross-section of printed silica areas at 20W.

As the scan speed increases, the layer thickness decrease, as shown in Figure 29. It was observed from the experiments that printed layers of 100µm thickness presented well-defined edges, better surface homogeneity and higher overall density.

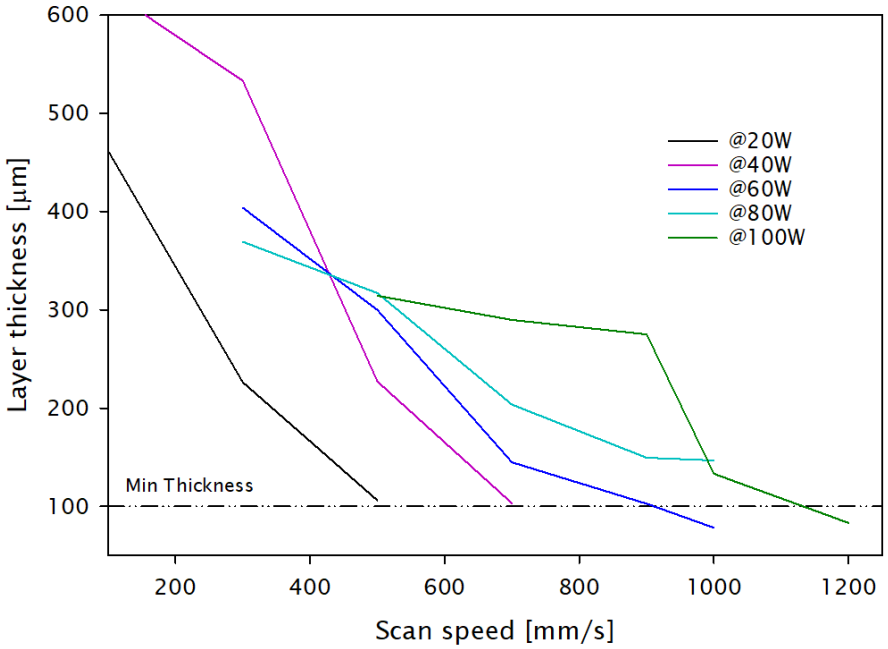

Figure 29. Layer thickness as a function of scan speed.

Scan speed is not the only variable of the printed parameters for single areas. The laser power is a critical parameter in the process. The energy density delivered from the laser beam to the power bed depends on the laser power and the exposure time. Therefore, it is essential to understand the relation between laser power and scan speed and their effect on the layer thickness. Figure 30 shows the parameter window to achieve a layer thickness of 100µm using LPBF.

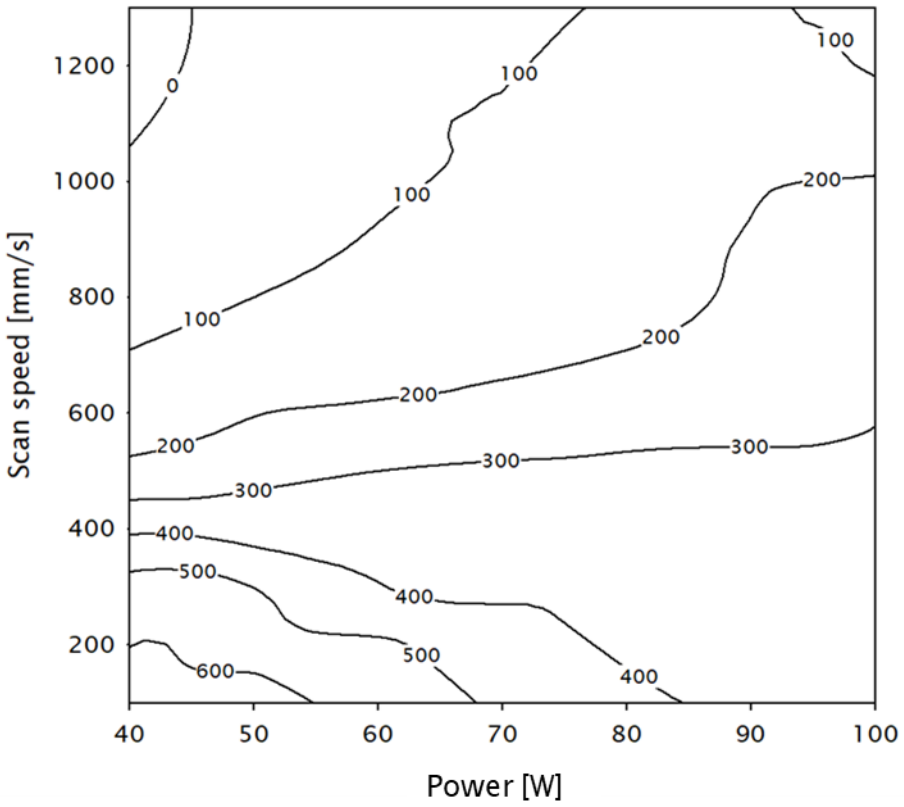

Figure 30. The layer thickness of 3D printed silica areas with respect to scan speed and laser power.

The experimental results on the average thickness of the silica in single layers were incorporated in the next set of experiments as an additional variable for volume structures.

3.6 Printed Silica Volumes by LPBF

Following the successful experimentation on single lines and single areas, 3D printed silica volume structures were produced by LPBF. The 3D printed volumes require good control of the shape and a high density of the printed volume. The multilayer process presents the additional challenge of controlling the residual stress formed between layers. The layers can present warpage while reaching relatively high densities. The following experiments focus on the printing parameters aiming to avoid additional stress in the layers and to prevent the formation of internal cavities without compromising the cohesion between layers.

To optimise the printing parameters, cubes with a width of 10mm per side were 3D printed using SiO_2 spherical powder according to section 3.1. The experiment was set to print nine samples for each printing conditions to increase the accuracy of the measurements. Table 8 lists the printing parameters of laser power, scan

speed, and layer thickness for a fixed hatch distance of 300µm. The overall calculated density of the printed bodies is also listed in this table.

Table 8. 3D printing process parameter for silica tri-dimensional structures.

Laser power [W]	Scanning speed [mm/s]	Layer thickness [mm]	Energy density [J/mm³]	Overall density [kg/m³]
20	300	0.1	2.222	1,058.08
30	300	0.1	3.333	1,134.15
40	300	0.1	4.444	1.158.25
50	300	0.1	5.556	1,141.73
60	300	0.1	6.667	1,191.38
40	100	0.1	13.333	900.00
40	200	0.1	6.667	1,190.00
40	400	0.1	3.333	1,161.87
40	500	0.1	2.667	1,093.01
40	300	0.05	8.889	1,125.50
40	300	0.08	5.556	1,169.47
40	300	0.12	3.704	1,125.61
40	300	0.15	2.963	1,100.36

The volumetric energy density (ED) in this table is calculated values with Equation 5, where *P:* laser power [W], *v*: scan speed [mm/s], *h*: hatch distance [mm] and *t*: layer thickness [mm].

$$ED = \frac{P}{v * h * t}$$

Equation 5. The energy density (ED).

The overall density of the printed cubes was calculated with Equation 6, where ρ: density [kg], *m*: mass [kg], *V*: volume [m³].

$$\rho = \frac{m}{V}$$

Equation 6. Density.

The effect of the printed parameters was analysed for each sample. Some 3D printed volume structures presented poor cohesion between layers at high energy densities due to warpage. In contrast, the low energy density applied in the process produced fragile structures.

The effect of the printing parameters on the overall density of the silica cubes was analysed. The scan speed was varied from 100 to 500mm/s with a fixed laser power of 40W and a layer thickness of 100µm, to analyse the effect of the scan speed on printed volume structures. Figure 31shows the increased warpage and low density for slow scan speeds.

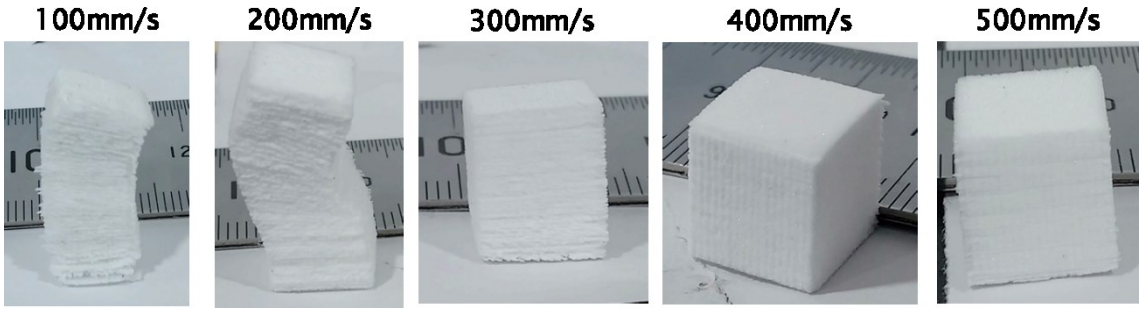

Figure 31. Effect of scan speed in 3D printed tri-dimensional structures.

Figure 32 shows the effect of scan speed on the overall density of the volume structures for constant laser power and layer thickness. The overall density of the printed solids improves significantly at higher scan speeds, whereas silica bodies printed with a scan speed below 300mm/s exhibit a high level of deformation due to warpage and poor overall density.

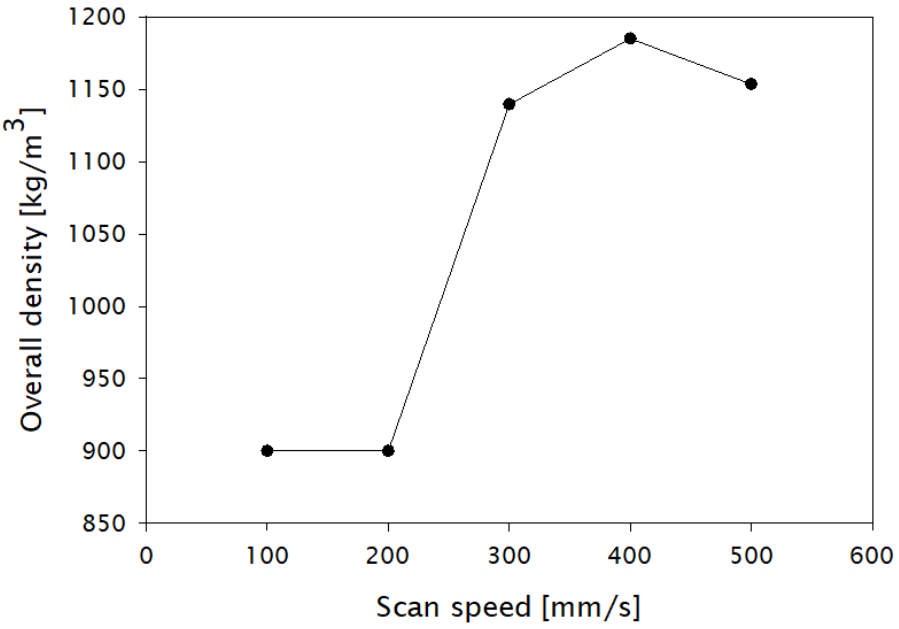

Figure 32. Effect of scan speed in the overall density of 3D printed tri-dimensional structures.

The micrographs in Figure 33, taken with a SEM, present the cross-section of silica printed samples with scan speeds of 200 and 500mm/s. It is noticeable that the use of higher scan speeds produces a more compact structure and consequently, a higher overall density of the printed body.

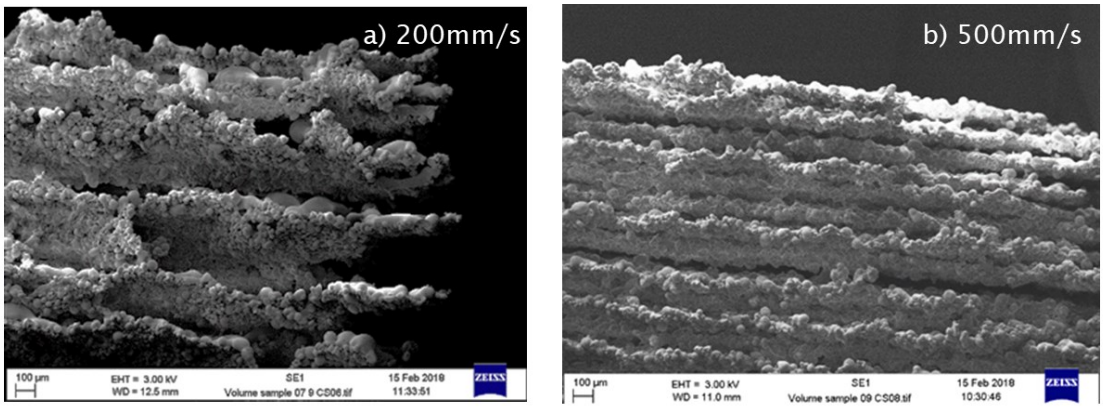

Figure 33. SEM micrographs show the effect of varying scan speeds on printed layers; a) low speed; b) high speed.

The effect of the laser power on the overall density was also analysed. A fixed scan speed of 300mm/s and a constant layer thickness of 100µm was used while the laser power delivered to the powder bed was varied from 20W to 60W.

Figure 34 shows a barely noticeable change in the printed volume structures with modified laser power. Even though the overall density of the printed bodies presents a slight change with varied laser power, it does not show evidence of detrimental warpage on the samples with an increase in laser power.

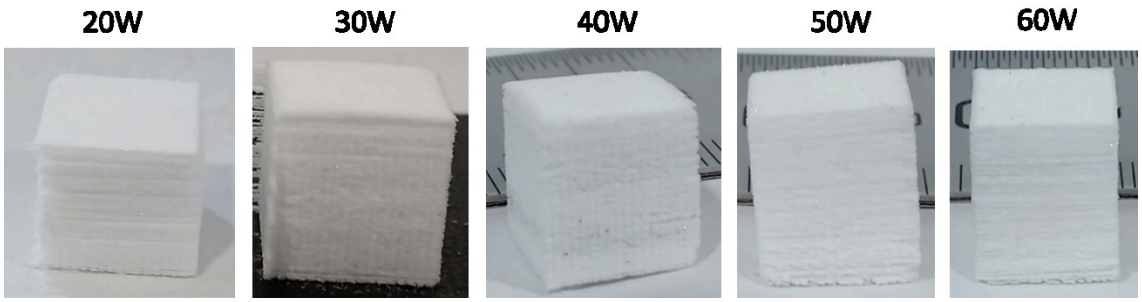

Figure 34. Effect of laser power in 3D printed volume structures

These results suggest that a varied scan speed has a more significant impact on the printing process than the laser power.

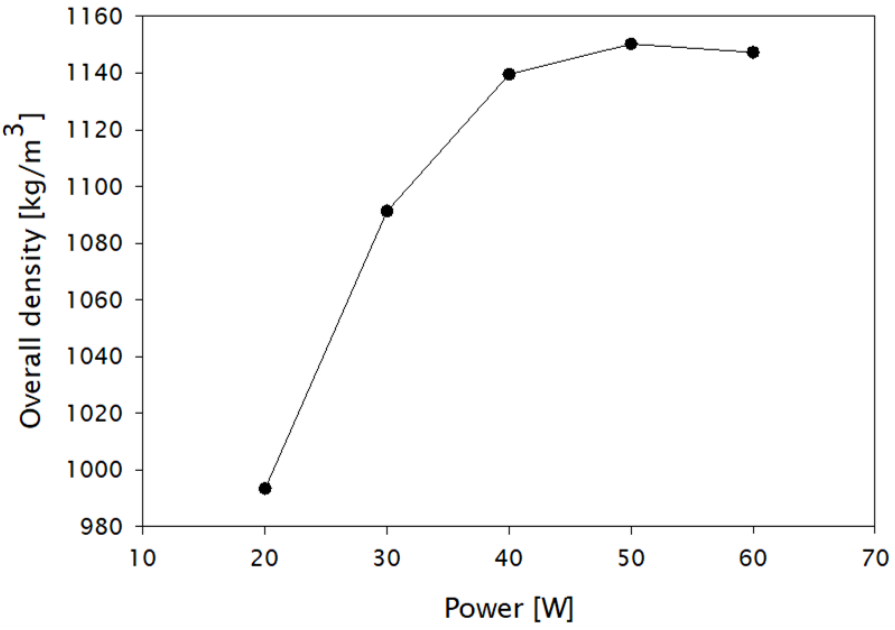

Figure 35. Effect of laser power on the overall density of 3D printed structures.

Figure 35 displays the effect on the overall density of the printed bodies due to the variation of the laser power from 20 to 60W with a constant scan speed of 300mm/s.

The effect of the layer thickness on the overall density of silica volumes was studied using a fixed laser power of 40W and scan speed of 300mm/s while the layer thickness was varied from 0.05 to 0.15mm.

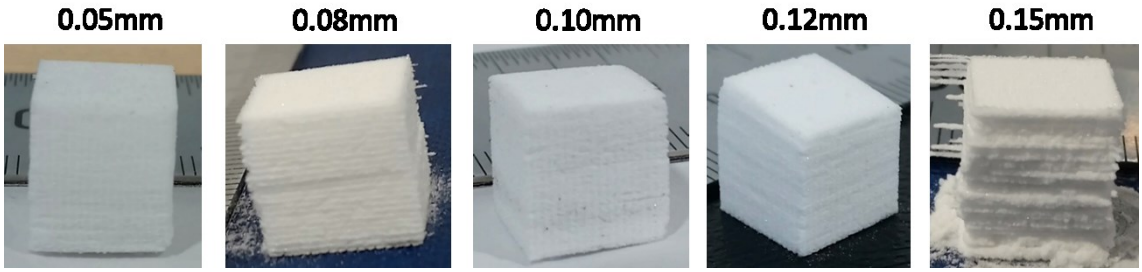

Figure 36. Effect of layer thickness in 3D printed volume structures.

Figure 36 shows the detrimental effect in the 3D printed parts with an increased layer thickness. Figure 37 shows that the overall density increases with a reduction in the layer thickness. The reduced overall density of the 3D printed parts with thicker layers is due to the reduced energy density that interacts with a larger volume of powder.

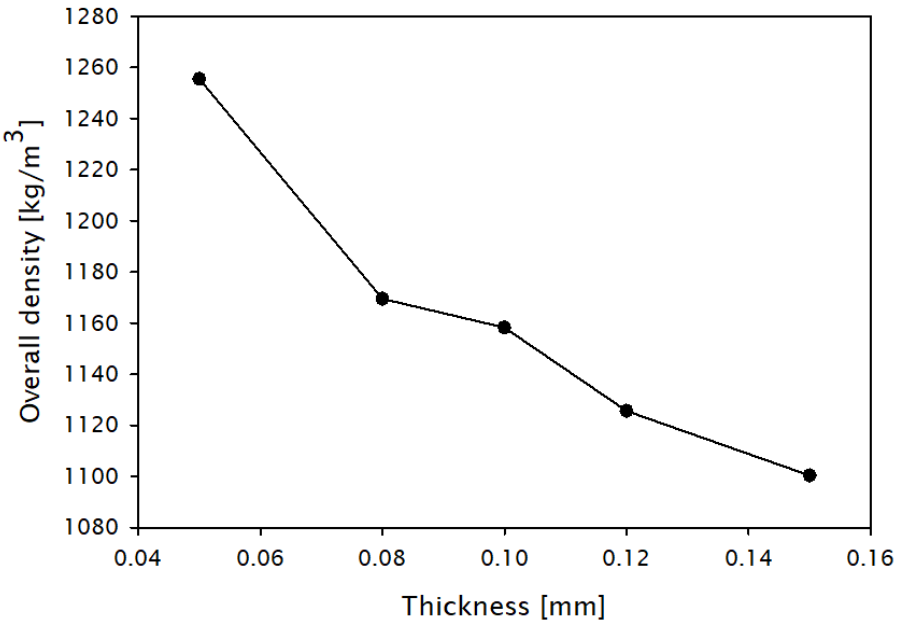

Figure 37. Effect of layer thickness on the overall density of 3D printed volume structures.

The overall density of silica volumes has the lowest repercussion when the layer thickness and laser power is varied. In contrast, scan speed has the largest impact on the overall density of the printed samples.

The graph presented in Figure 38 considers the combined effects on the overall density of the printed samples, varying the three analysed variables: scan speed, laser power and layer thickness. This information was used to estimate the printed parameters for a volume structure with high density and low warpage.

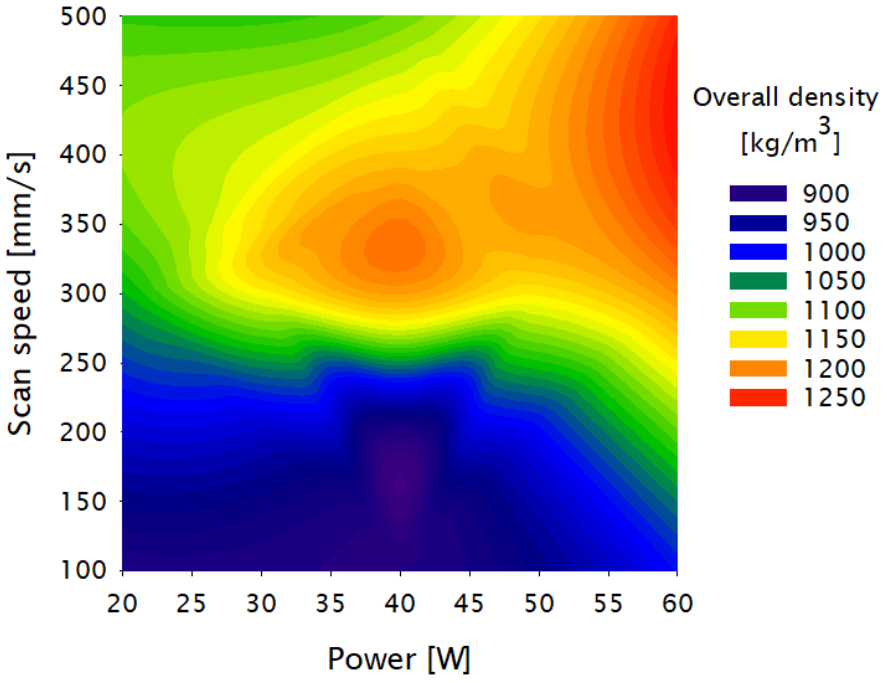

Figure 38. Proposed model for 3D printing silica tri-dimensional structures.

Silica cubes were printed targeting an overall density between 1100 and 1200kg/m^3. With the available data, the process conditions were set to 60W laser power, 100µm of layer thickness and a scan speed of 900mm/s. Figure 39 shows the printed silica volume with an overall density of 1,119kg/m^3.

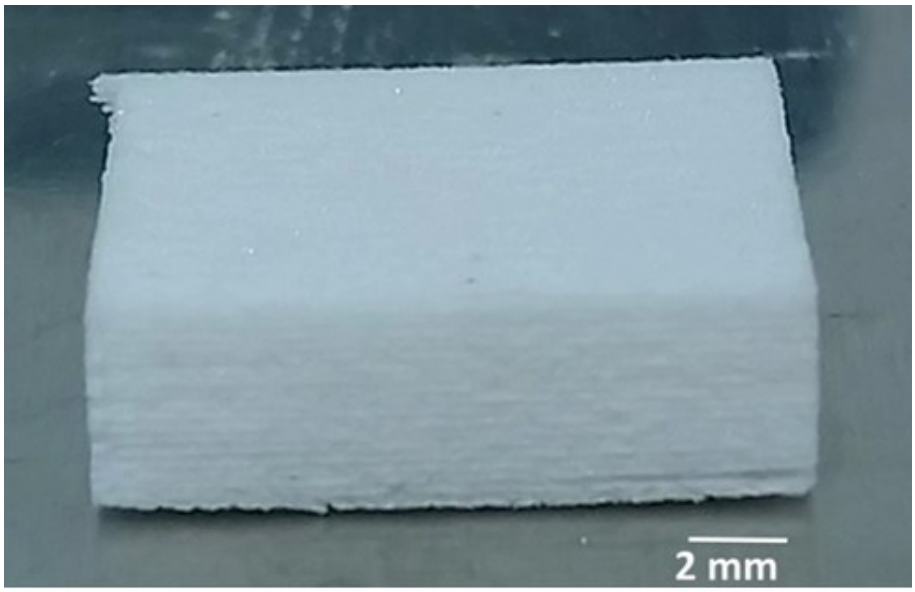

Figure 39. Volume structure printed using the proposed model.

3.7 Germanium-doped Silica

The use of different optical materials has been a paramount motivation of the LPBF process reported in this thesis. Therefore, it was essential to demonstrate the capability of the system to produce 3D printed structures with silica powder doped with other materials.

Spherical silicon dioxide and germanium dioxide (GeO_2) were mixed mechanically. Figure 40Figure 3 shows the in-house ball miller. The powder was mixed in a ball miller for 48 hours at 17rpm using a weight ratio of 3.5:1.

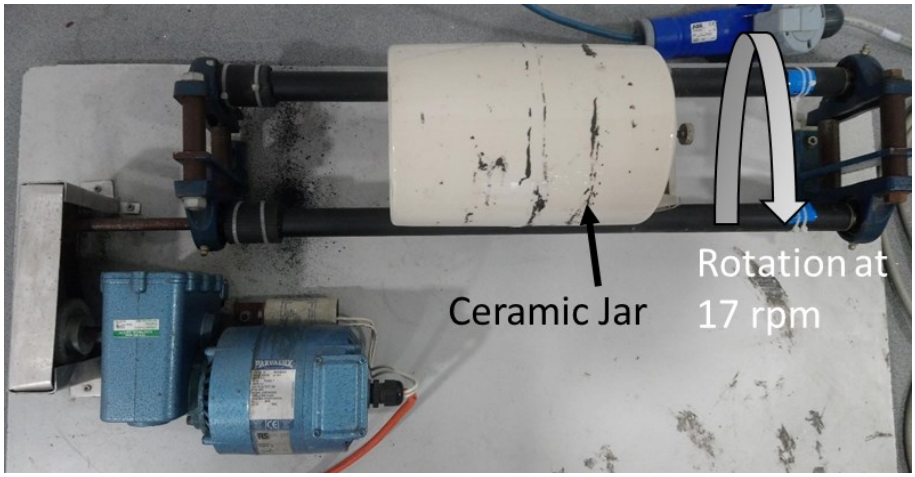

Figure 40 Experimental setup for mixing SiO_2 and GeO_2 powders.

The GeO_2 powder presents an irregular particle geometry. The flowability of mixed powder was measured by the funnel technique, explained in section 3.1. It was found that at low GeO_2 content in the mixture has a similar angle of reposed compared to pristine SiO_2 powder. A large content of germanium; however, affected the flowability of the mixture, as shown in Figure 41.

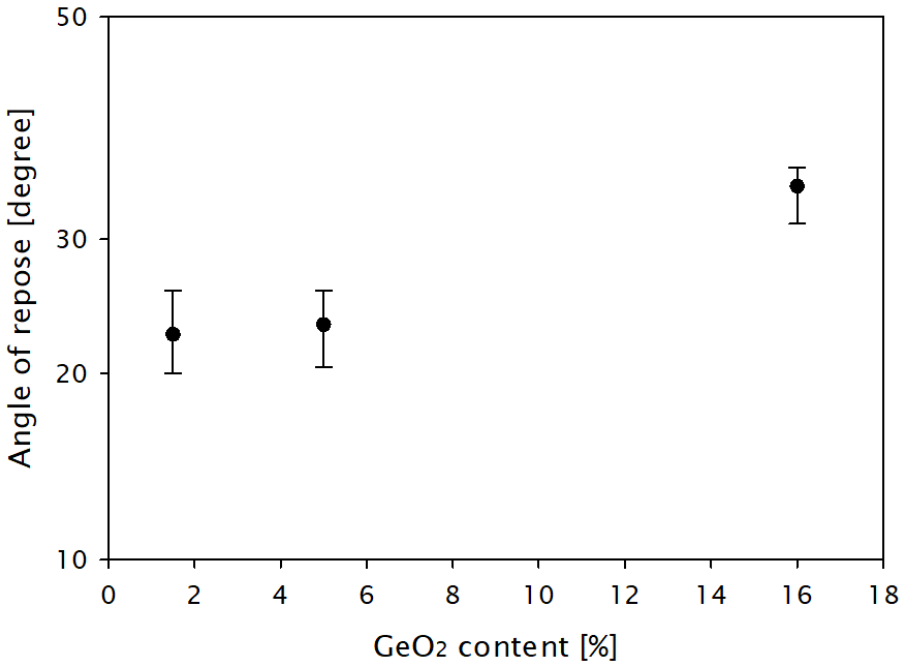

Figure 41. The angle of repose of GeO_2 doped silica powder.

Pristine and mixed silica powder were evaluated using a thermo-gravimetric analysis. Figure 42 shows the T_m for pristine powders and SiO_2-GeO_2 mixed powder with a different ratio. The pristine silica powder presented a melting point just above 1400˚C, which is ~300˚C below the T_m of soot silica. This difference can be explained due to the impurities in the spherical silica powder. In contrast, germanium powder presented a T_m of 1116˚C, which corresponds to its theoretical

melting temperature. Mixed powder of 2, 4, 8 and 16wt% GeO_2 ratios were also analysed, and it was found that the melting point of the mixed powder is lower with an increased percentage of GeO_2.

The 3D printing parameters, laser power and scan speed were adjusted for the new powder composition. According to the TGA results, it was expected that the energy density required to 3D print the germanium-doped silica powder was lower compared to the pristine SiO_2 powder.

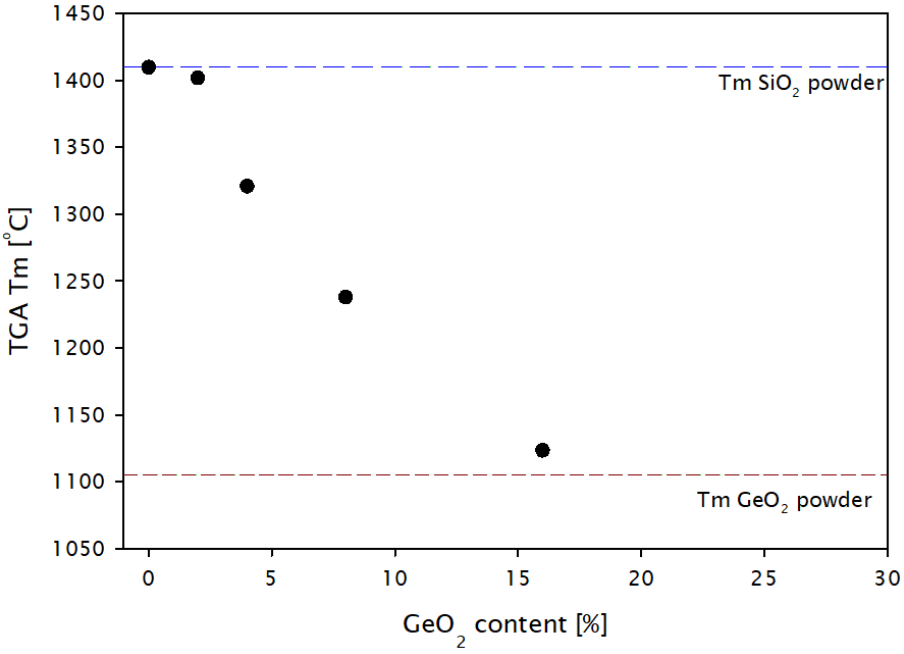

Figure 42. TGA measurement of SiO_2 and mixed SiO_2-GeO_2 powders.

A calibration experiment was performed to approximate the magnitude of the required adjustment. Initially, the same printing conditions for SiO_2 were used to print the SiO_2-GeO_2 powder. It was observed that the mixed powder presented a more visible warpage and poor density (~ 0.62g/cm^3), which can be explained due to the lower T_m of the mixed powder. Therefore, the process parameters were adjusted to 50W laser power, and a scan speed of 850mm/s while maintaining 100µm for the layer thickness. Overall, the energy density was reduced by ~12% compared to the SiO_2 experimentation.

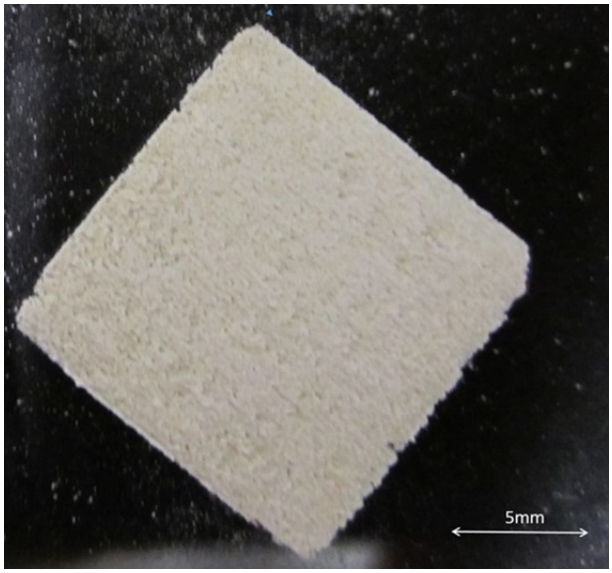

Figure 43. 3D printed structure using germanium-doped silica powder

Figure 43 shows the 3D printed structures obtained with the new parameters established for germanium-doped silica powder. This structure has an overall density just above 1g/cm^3.

The capability to 3D print germanium-doped silica structures has been successfully demonstrated. It should be noted that the printing parameters will require adjustment according to the desired mol% of dopant content in the silica matrix to achieve a waveguide according to specific designs of the fibres.

3.8 Densification process

As previously explained, the silica powder does not fully melt when silica printed bodies were processed with low energy. Thus, the produced green bodies were porous forming voids between layers. The relative density of these porous silica bodies with respect to glass density is below 60%.

To improve the overall density of the printed bodies, aiming quartz density[118], the 3D printed silica structures were heat treated. In addition, it can be expected that impurities in the SiO_2 powder, listed in section 3.1, can be burned off in this post-process. The temperatures for this densification process were set to a range between 1550˚C and 1600˚C.

A set of samples for this experiment were fabricated as described in section **Error! Reference source not found.**, with an overall density of ~1150kg/m^3. This overall density was achieved using a laser power of 40W with a scan speed of 300mm/s and a layer thickness of 0.1mm. The printed silica samples were placed in a furnace

with a controlled N_2 atmosphere at 300°C for 30 minutes, followed by an incremental ramping temperature stage at a rate of 10°C/min. After a dwell time of 3 hours, the samples were rapidly cooled to room temperature. Figure 44 shows the thermal cycling process for the 3D printed samples.

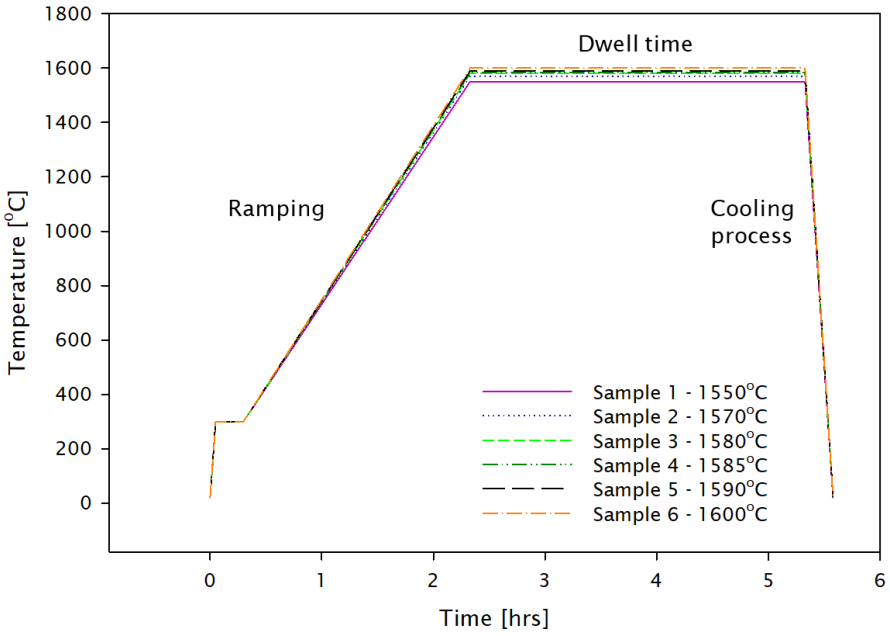

Figure 44. The thermal treatment process of 3D printed structures.

It was observed that the samples went through a crystallisation process after they were retrieved from the furnace. Figure 45 shows the evolution of the nucleation process of the 3D printed bodies to full crystallisation of the samples.

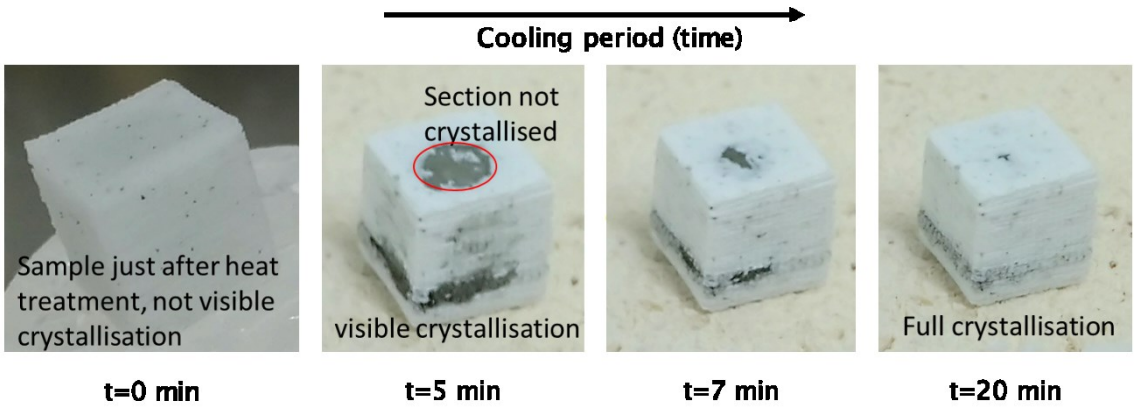

Figure 45. The crystallisation process of 3D printed structures.

In order to understand the nature of the observed crystallisation, XRD analysis was performed. Figure 46 presents the diffractogram obtained from the crystallised samples after heat treatment. In addition, the crystallographic standard for the synthetic cristobalite is shown as a reference, which corresponds to diffractogram presented in the silica crystallized samples.

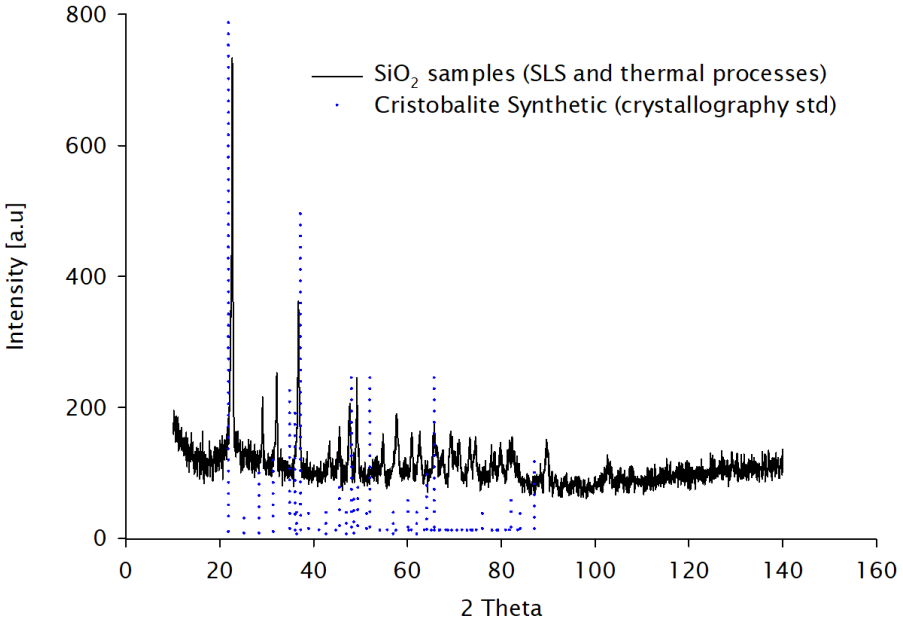

Figure 46. XRD from crystallised 3D printed structures after heat treatment.

The crystallisation process observed in the samples can be explained with the formation of cristobalite crystals in the 3D printed silica structures due to the heat treatment. However, the origin of the crystallization is uncertain. Therefore, XRD analysis of the 3D printed bodies was performed before the sintering heat treatment to investigate the crystalline nature of the 3D printed structures after the SLS process.

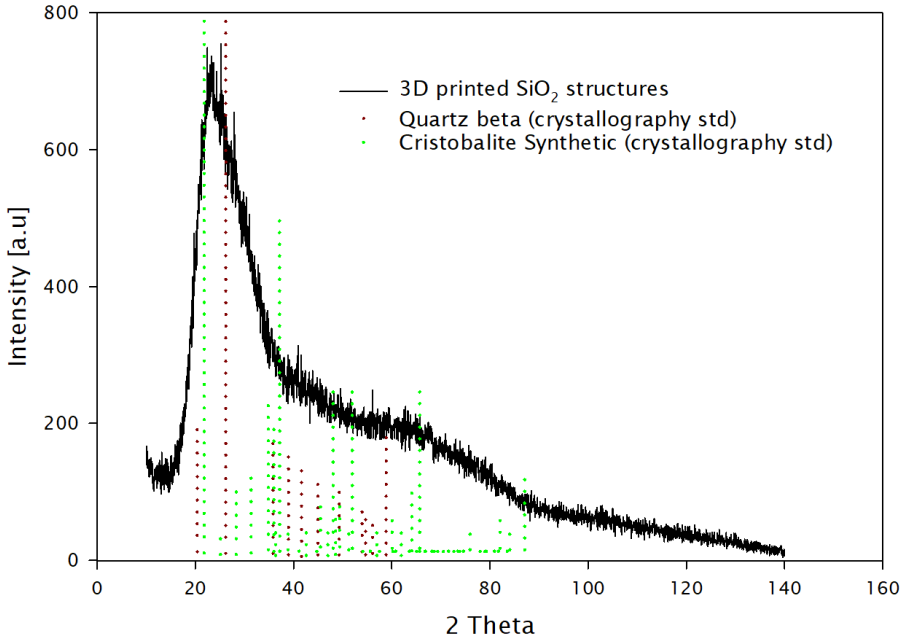

Figure 47. XRD from 3D printed structures before heat treatment.

Figure 47 shows the diffractogram obtained from the samples after the 3D printing process, as well as the crystallographic standards for cristobalite and β-quartz as

a reference. The XRD analysis performed for the 3D printed structures confirmed that the crystallisation is a result of the sintering heat treatment. Nonetheless, the diffractogram also shows indications that the 3D printed structures contain a fraction of cristobalite and β-quartz crystals. Further XRD analysis was performed in the pristine silica spherical powder before 3D printing.

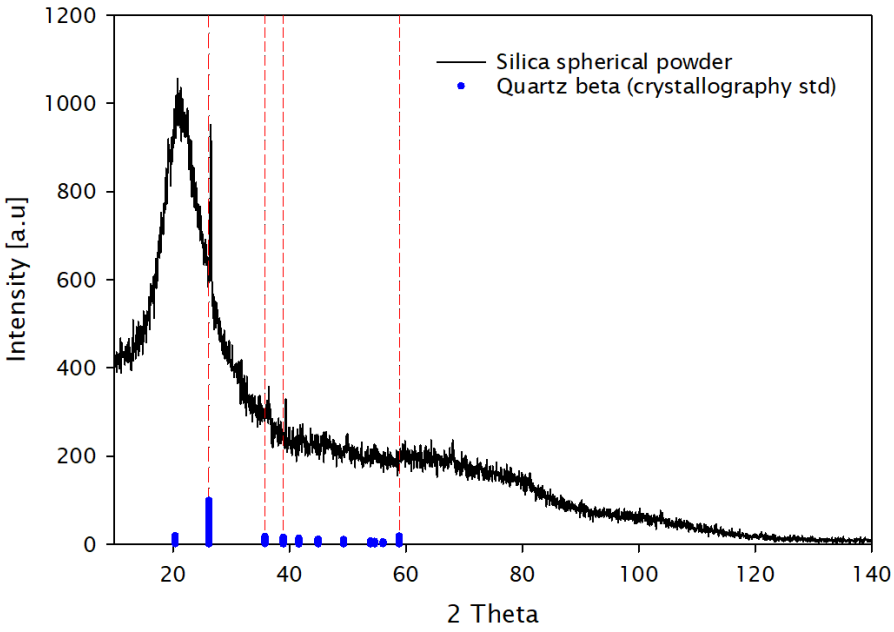

Figure 48. XRD from silica spherical powder before the 3D printing process.

The diffractogram shown in Figure 48 corresponds to the spherical silica powder before the 3D printing process. The crystallographic standard for β-quartz is also presented as a reference. The XRD analysis of the spherical silica powder evidences that there is a crystalline fraction of β-quartz in the pristine powder.

The evidence suggests that the spherical silica powder has an amorphous nature with a fraction of β-quartz crystalline phase, which is affected by the thermal energy provided by the laser beam. The printing process provides enough thermal energy to promote a more complex crystalline phase distribution, where a fraction of the β-quartz crystals is converted to cristobalite.

The thermal treatment from the densification process adds enough energy to the silica, which undergoes a full crystalline transition into cristobalite when exposed to temperatures greater than 1470°C. The cristobalite phase is then fixed on the silica matrix by the crystallisation process while the samples cooled down after being retrieved from the furnace.

Due to the crystallisation presented after the heat-treatment, it was essential to validate the crystalline nature of the final optical material obtained after the

drawing process, where the silica is exposed at temperatures above its melting point, and crystallisation can be avoided. Therefore, a circular 3D structure was built using the same parameters. The sample was exposed to the sintering heat treatment and finally processed in the fibre drawing tower. A sample from the tapered region of the 3D printed preform, which has been exposed to the fibre drawing fabrication conditions was analysed using XRD.

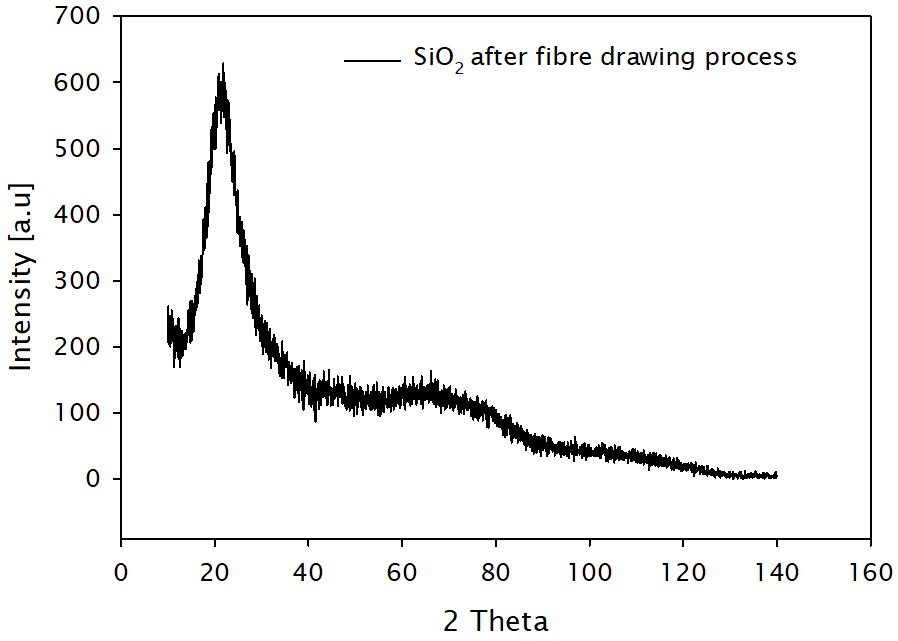

Figure 49. XRD from 3D printing silica preform after the fibre drawing process.

Figure 49 presents the diffractogram obtained from the section of the 3D printed silica structure after being exposed to the fibre drawing fabrication conditions. The XRD analysis demonstrates the amorphous nature of the final material, which is suitable for the optical application pursued in this research. The high temperatures during the fibre drawing (above 2000˚C) allow the fractions of crystals to fully melt the material. Once the fibre exits the furnace, the glass experiences an extremely fast cooling process setting the amorphous nature of the silica glass.

From the crystallisation analysis presented above, it was necessary to investigate the densification conditions that minimise the crystallisation process while providing the highest density. Hence, a set of experiments were carried out to investigate the threshold of the dwell time in the furnace that triggers the crystallisation process in the 3D printed structures. In addition, it was necessary to evaluate the impact of processing time in the overall density of the 3D printed silica structures.

3D printed silica square samples with a width of 15mm, an overall density of ~1.12g/cm^3, were densify with heat treatment. It was found that samples heat-treated above 1580˚C presented crystallisation. Figure 50 shows the diffractogram of the crystalline nature of the 3D printed structures exposed to the densification process for a maximum duration of 1.5 hours (10min dwell) and densification temperature below 1580˚C. After this threshold, the samples start to exhibit severe crystallisation.

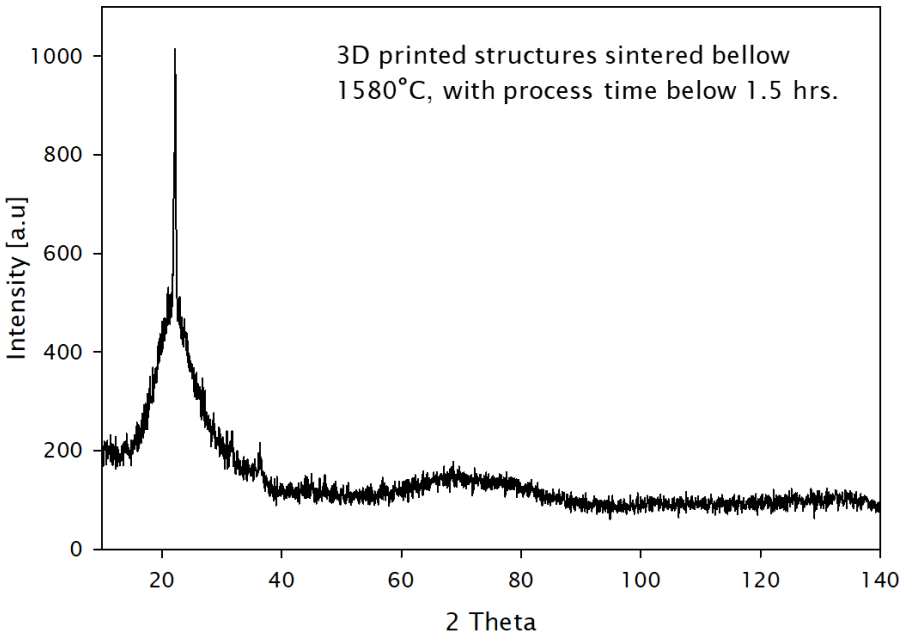

Figure 50. XRD of 3D printed silica structures with sintering process time below 1.5hrs.

A new thermal densification treatment recipe was developed to maximise the densification process and minimise crystallisation of the samples. Figure 51**Error! Reference source not found.** shows the modified thermal cycling process. Samples were placed in a furnace in an inert atmosphere at 800˚C for 30min; the temperature was ramped up to 1570˚C at a rate of 10˚C/min. The dwell time was modified for each sample, as described in Figure 51**Error! Reference source not found.**. Samples were cooled rapidly to room temperature, showing no sign of crystallization.

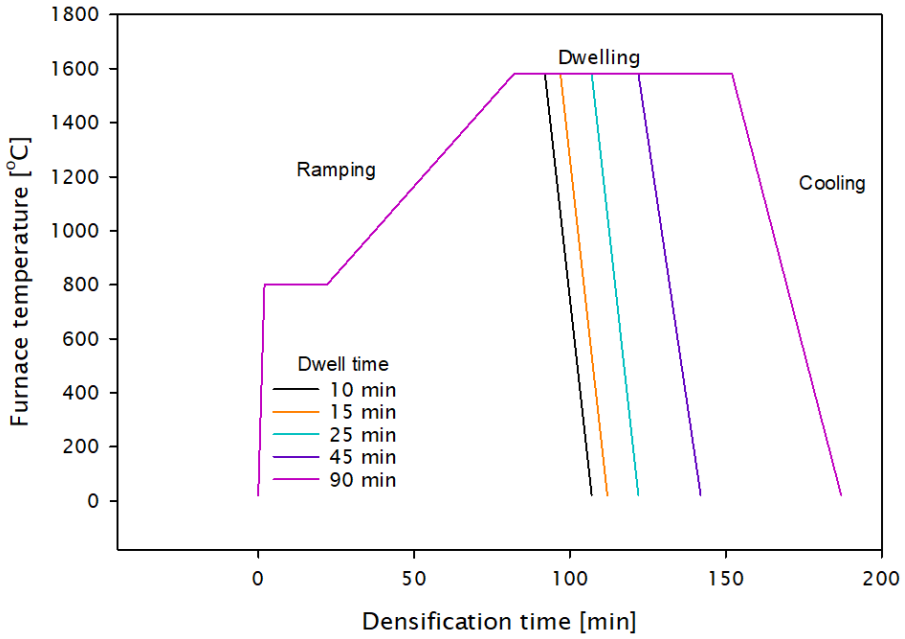

Figure 51. The modified thermal treatment process of 3D printed structures.

The overall density of the 3D printed structures, after the modified heat treatment, presents values between 2,000 and 2,100kg/m^3, which is within the reported values for silica glasses for optical applications, as shown in Figure 52.

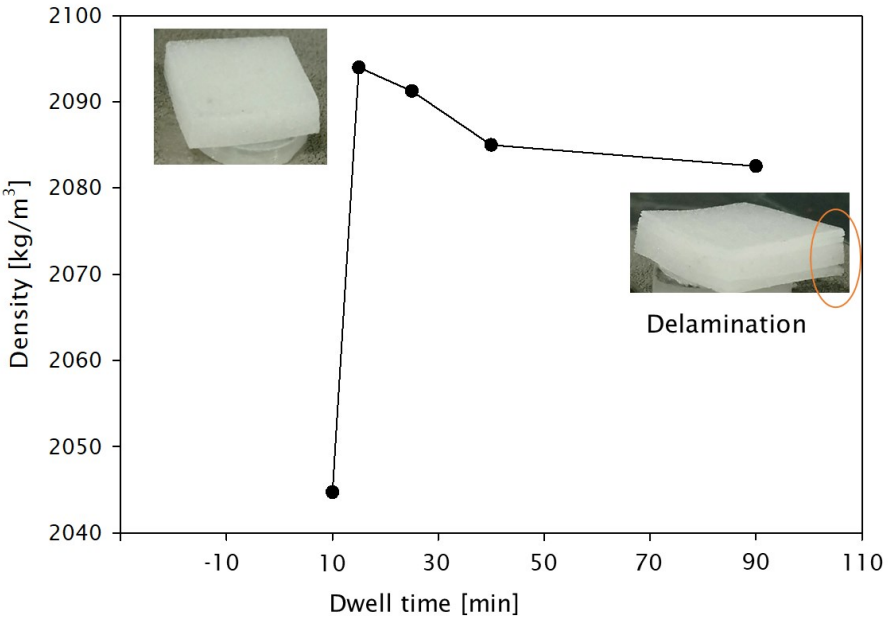

Figure 52. Effect of density process in the overall density of 3D printed silica parts.

The sample with longer dwell time exhibits signs of warpage, whereas densified shorter dwell time does not present the aforementioned detrimental effect.

After the modified thermal treatment was established, the samples were analysed with SEM to observe the topographical changes in the 3D printed samples after the sintering process.

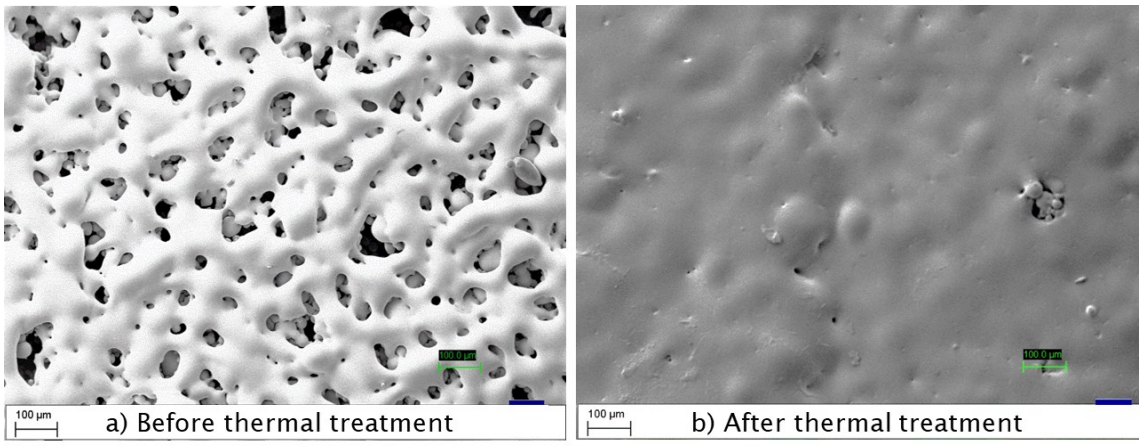

Figure 53. Effect of the sintering process in the 3D printed silica structures: a) Before; b) After.

Figure 53 shows the importance of the thermal sintering treatment and the evident improvement in the surface roughness and density of the 3D printed silica structures.

3.9 Summary

In this section, it was successfully demonstrated that silica structures can be produced by LPBF process. The parameter for 3D printing silica single lines, singles layers and volume structures were developed, and the impact of fabrication variables such as laser power, scan speed, layer thickness and energy density were investigated. The crystallisation of the 3D printed silica structures after the heat treatment process was analysed. Optimisation of the densification process was developed to obtain an overall density suitable for optical components.

Chapter 4 Development of 3D printed Silica Preforms with Complex Structures and Multiple Materials

In this chapter, the fabrication parameters for 3D printed silica were used to produce functional structures based on optical preform fabrication. The fabrication of optical preforms with complex geometries for single and multiple materials is discussed in this section. Optical fibres manufactured from 3D printed optical silica preforms are reported along with their physical and optical characteristics. Optical preforms with micro-structured designs such as photonic crystal fibre (PCF) and antiresonant fibre (ARF) were successfully demonstrated at the end of this chapter. A multicore optical preform is produced and demonstrated the multi-material flexibility of the 3D printing process.

4.1 Thin wall-thickness printing parameter optimisation

3D printed silica preforms with complex geometries and fibres with novel designs such as microstructured fibres, and anti-resonant fibres will require the development of a fabrication process to produce a thin wall-thickness, which will enable the construction of the inner lattice of the preforms design. Honeycomb or the PBG preforms are an example of such designs.

The resolution of the lattice, and hence the wall-thickness, is a critical parameter to consider for the printing process, as well as for the CAD design. However, these parameters will be dependent on the minimum resolution or spot size of the laser system used for the fabrication process.

A set of experiments was performed to identify the wall-thickness resolution feasible achievable with the 3D printing setup. The samples were printed using a laser power of 60W, a scan speed of 500mm/s and a layer thickness of 100µm. Cylindrical geometries with an outer diameter (OD) of 9.5mm and a wall thickness of 0.5, 1, 2 and 4mm, were printed. The fabricated preforms are shown in Figure 54.

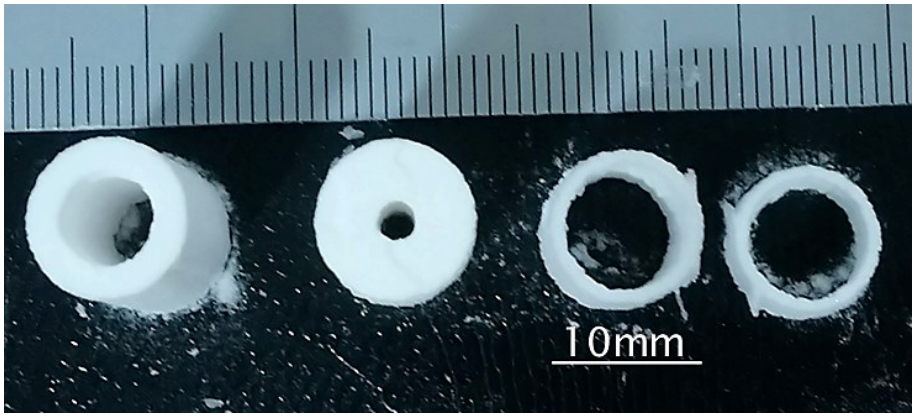

Figure 54. 3D printed silica preforms with different wall thickness.

This experiment demonstrated the possibility to create a wall thickness of 1mm without defects in the structure. Geometries with wall-thickness below 1mm presented structural inconsistencies between layers, and the structure was exceptionally fragile after the residual powder from the printing process was removed.

Further optimisation on the energy density was performed to enable the simultaneous printing of thin and thick wall-thickness in the same preform, as shown in Figure 55. Other silica preforms with complex structures were achieve varying the deliver energy density accordingly to the structure lattice.

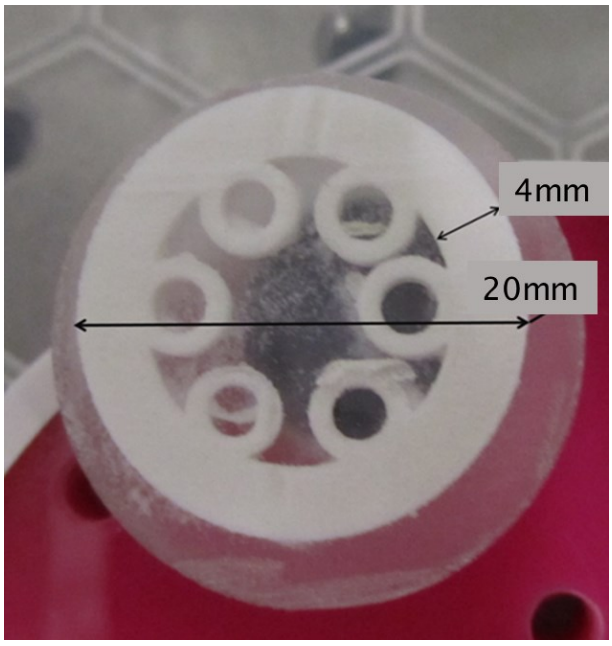

Figure 55. 3D printed silica anti-resonant preform

The external diameter of the preform was 20mm with a wall thickness of 4mm and the inner lattice wall-thickness of 1mm. The printing parameters were adjusted for a laser power of 60W, a scan speed of 850mm/s and a layer thickness of 100µm.

This antiresonant preform structure was used for calibrating the parameters of the 3D printing process.

4.2 3D printed preforms in a single material

Arbitrary designs of PCF and ARF silica preforms were 3D printed using the printing parameters defined in the previous section. An energy density of ~2.7 J/mm^3 was used to produce these preforms. The different photonic crystal fibre designs, fabricated by LPBF, are described in Table 9.

Table 9. PCF designs for 3D printed silica preforms

PCF Preform	Air hole diameter [mm]	Pitch distance [mm]	Arms num.	Core Diameter [mm]	OD [mm]
a	2	5	3	8	38
b	1.5	3	3	3.5	20
c	0.5	1.2	5	2	16

The designs vary in the following characteristics: air-hole diameter, pitch distance, number of arms and external diameter. Figure 56 presents the cross-section of the 3D printed PCF silica preforms. The chosen designs demonstrate the capability to print small holes in complex geometries as well as define wall structures with a good resolution.

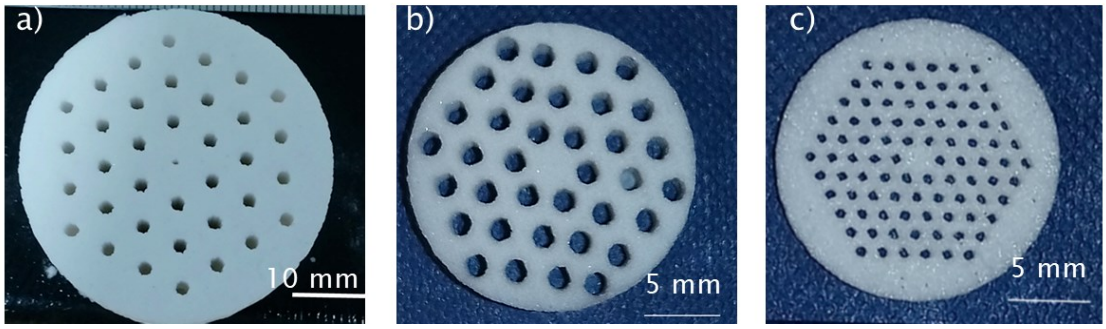

Figure 56. 3D printed silica PCF preform designs

In addition, anti-resonant preforms were 3D printed in silica according to the designs described in Table 10.

Table 10. ARF designs for 3D printed silica preforms.

AR Preform	Fibre designed	Core Diameter [mm]	Cladding wall-thickness [mm]	OD [mm]
a	SAR_{fbf}	5	1	16
b	DAR_{fbf}	2.5	1	16
c	DAR_{fbf}	5	1	16
d	DAR_{fbf}	6	1	19

The selected AR preform designs demonstrate the versatile possibilities to print extreme ratios between core diameter and air hole cladding, as shown in Figure 57.

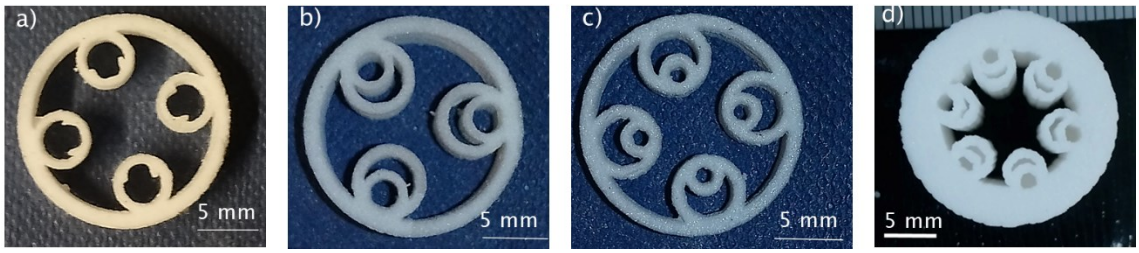

Figure 57. 3D printed silica anti-resonant preforms designs.

The printed designs do not follow any specific pattern or AR design based on mathematical models; the designs were chosen only for demonstration purposes. The capability to print thin walls and complex geometries with good control of the printing structures were demonstrated using a low energy density in a LPBF process. In section 7.1, the effect of the energy density on the printed preforms is discussed.

4.3 3D printed preforms in multiple materials

In this section, preforms using multiple materials were produced by the assembly process of core and cladding. Due to equipment limitations, it was not possible to print multiple materials simultaneously. Therefore, the fabrication process was adjusted to produce 3D printed cores and claddings independently, and subsequently, assemble them prior to heat treatment.

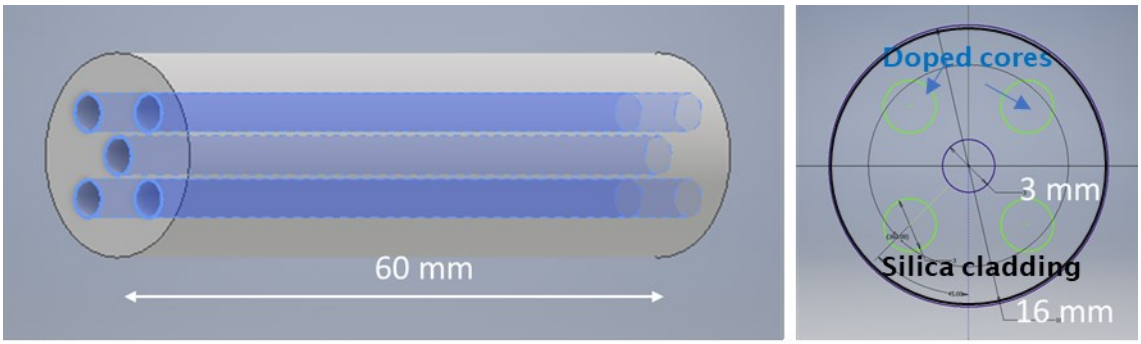

Figure 58. Multicore preform design for 3D printing of multi-materials using LPBF.

Single-core and multicore preforms were fabricated according to the model shown in Figure 58, where doped core structures are shown in blue and silica cladding is shown in white. An initial preform length of 60mm with an OD of 16mm and a core size of 3mm was selected to demonstrate the capability of the process. The selected composition of the core material was silica powder doped with 4mol% of germanium dioxide, aiming to reach a delta n of 0.0056 in the optical fibre.

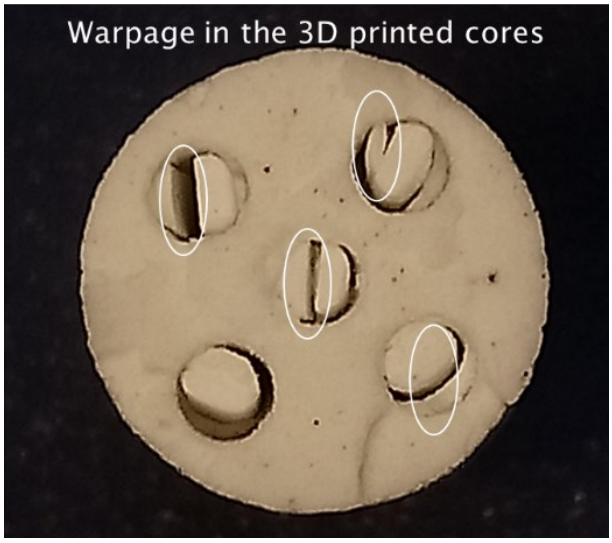

Figure 59. Multicore preform with warpage in the core regions.

The multicore preform was built in three steps: first, the silica cladding structure with five holes was printed; second, the five core structures using germanium doped silica were printed; and finally, both structures were assembled by inserting the cores in the cladding holes. A preform with evident warpage in the core region is shown above in Figure 59.

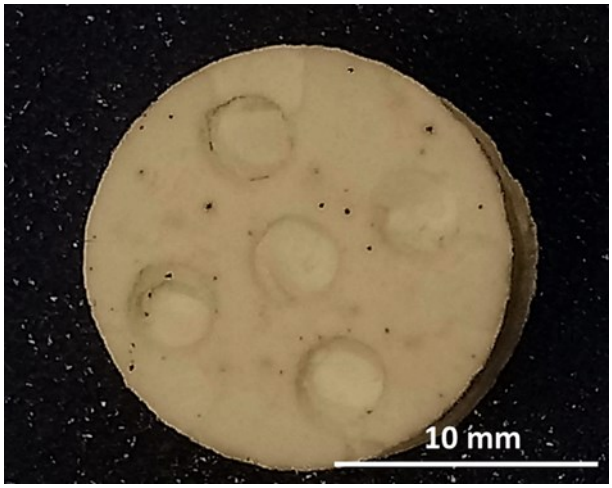

Figure 60. 3D printed multicore preform using multiple materials.

The defects in the core areas are the result of the chosen printing strategy for these parts. The cores were printed longitudinally due to their small diameter; however, they showed large amounts of defects after the heat treatment. Therefore, the printing strategy for the core parts was modified, changing the axial reference of the printing system. Figure 60 shows the first demonstration of a 3D printing multicore silica preform fabricated using LPBF.

4.4 Fabrication overview of optical fibres from 3D printed silica preforms

The paramount objective of this research was to fabricate optical fibres from 3D printed preforms. Figure 61 shows the assembly of the preform before the fibre fabrication. The 3D printed preforms were placed inside a silica glass tube F-300 to help to hold the preform inside the vertical furnace for fibre drawing.

Figure 61. Fibre drawing conditioning of 3D printed silica preforms.

As explained in section 2.2.1, the first section of the preform, which is called a drop, is a disposable piece of glass that works as weight, which precipitates by gravity, forming the pulling neck during the fibre drawing. Therefore, in the preparation of the 3D printed preforms, a disposable weight was added to the assembly to maximise the available 3D printed preform length, as shown in Figure 62.

Figure 62. Disposable weight for the 3D printed preforms.

Once the assembly was completed, it was transferred to the vertical furnace of the fibre drawing tower, as presented in Figure 63.

Figure 63. 3D printing preform set in fibre drawing furnace.

Figure 64 shows the 3D printed optical silica fibres coming out of the lower iris of the furnace as the tower mini capstan is pulling it. The fibres were coated with the UV curable high-index polymer DSM-314.

Figure 64. Fibre drawing process of the 3D printed silica preforms.

The attenuation measurements were performed using an optical spectrum analyser (OSA) and a white light source (WLS).

4.4.1 Optical fibres from 3D printed preforms in a single material

A 3D printed solid silica preform with a diameter of 9mm was inserted in a fluorinate glass tube to obtain a high refractive index contrast with respect to the silica preform. An initial preform was drawn to a 200µm OD fibre with a core diameter of 110µm. The final fibre exhibited a noticeable porosity across the core region, visible as small black holes in Figure 65.

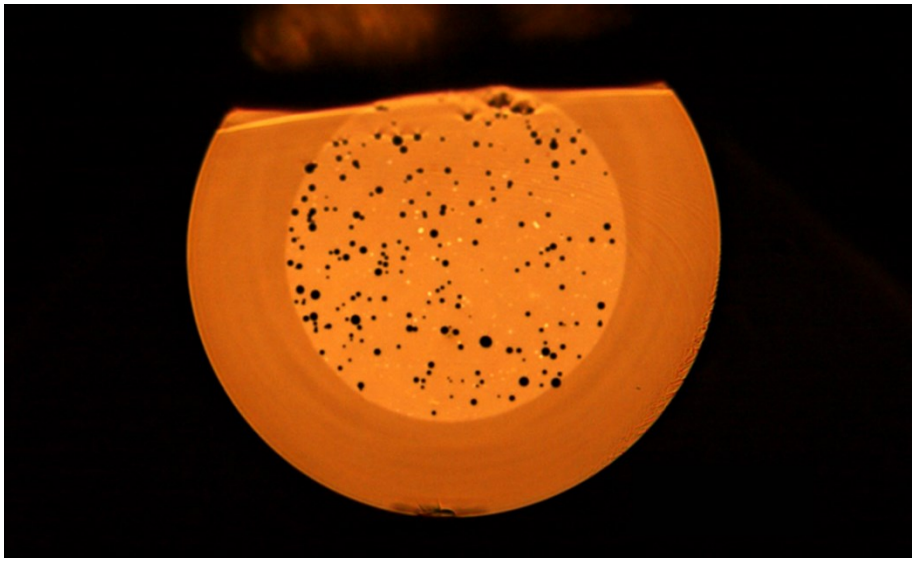

Figure 65. 3D printed silica preform drawn to fibre with 110µm core size.

Therefore, the drawing process was optimised using vacuum during the drawing process. A second fibre was produced with an OD of 120µm and a reduced core diameter of 45µm. As is shown in Figure 66, the porosity of the core region in the second fibre showed a considerable improvement. The use of a vacuum system helps to improve the densification on the printed parts.

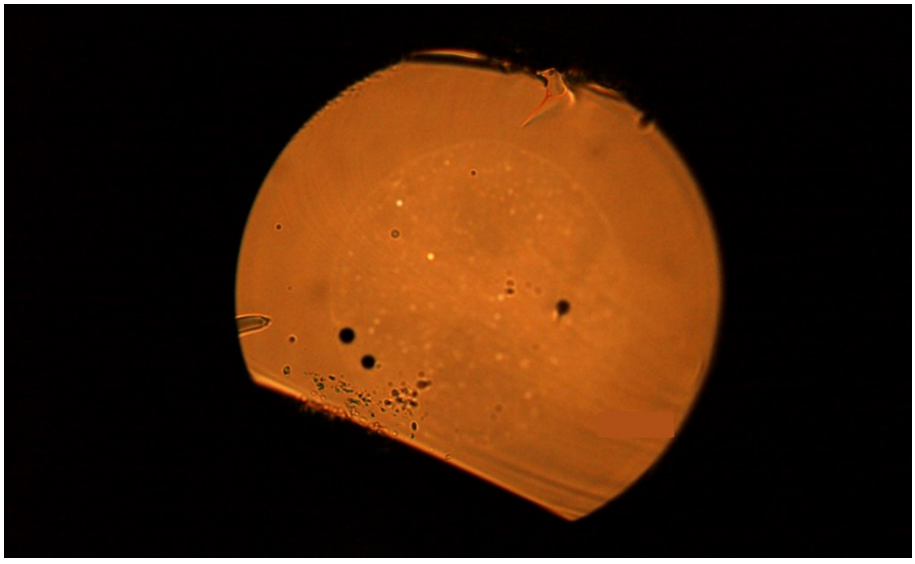

Figure 66. 3D printed silica preform drawn to fibre with a core size of 45µm.

The transmission measurement of the fibre revealed a high OH absorption at ~1380nm and a considerable additional absorption in the ~1195nm region. This was not investigated but is likely to be an absorption associated with the impurities in the raw material. The transmission spectrum of the fibre spans from 350nm to 1750nm and is shown in Figure 67.

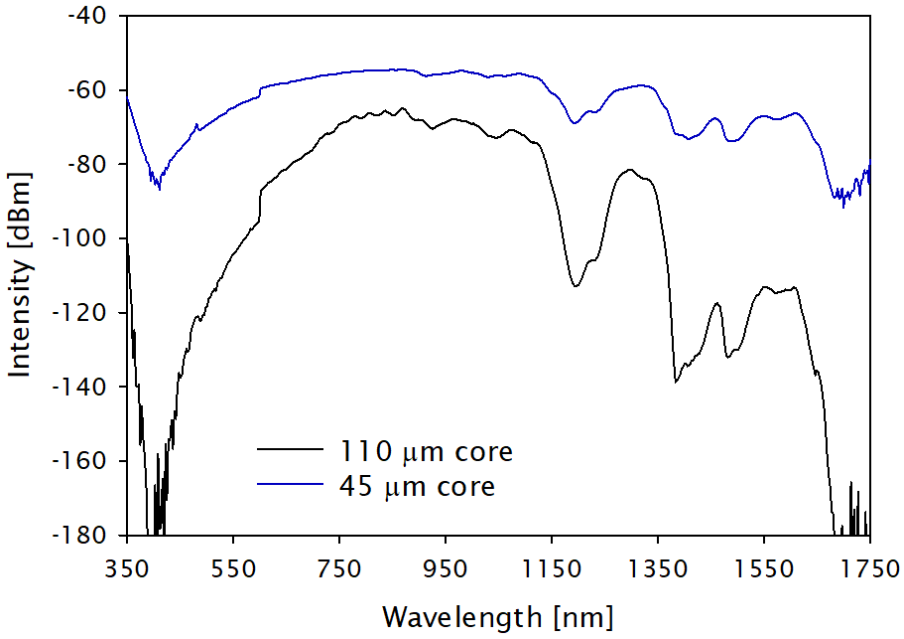

Figure 67. The transmission spectrum of 3D printed silica optical fibres.

Both fibres with a core size of 110µm and 45µm have an attenuation level of ~50dB/m and ~23dB/m at 800nm respectively. Due to the low NA between the 3D printed silica preforms and the fluorinated tube, the induced modal propagation losses are noticeable higher for the fibre with a larger core size.

A validation experiment was performed to evaluate the loss contribution of the 3D printing process to the fibre produced by LPBF. A fibre was drawn from a preform fabricated with the powder-in-tube technique. SiO_2 spherical powder was placed inside a fluorinated tube and was drawn under the same conditions as the 3D printed preforms. The fibre was drawn to an OD of 120µm and a core size of 45µm. The cross-section of the fabricated fibre is shown in Figure 68.

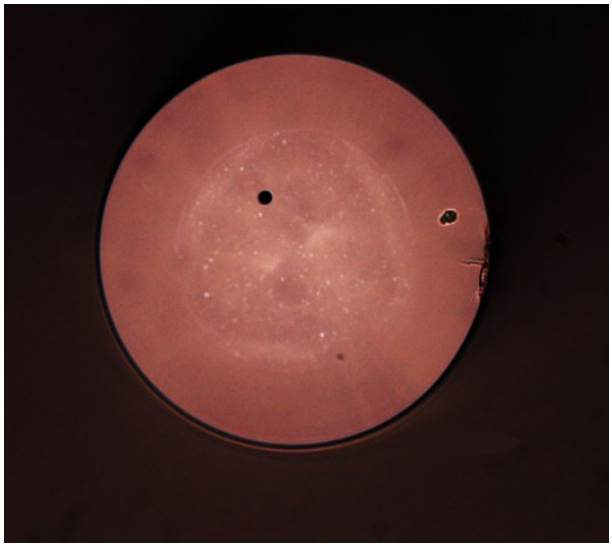

Figure 68. Optical fibre from a powder in tube preform.

The optical fibre produced with the powder-in-tube method has an attenuation level of 1.4dB/m at 800nm, while the fibre drawn from a 3D printed solid silica preform presented attenuation of ~23dB/m at the same wavelength. Figure 69 shows the loss of the 3D printed fibre, which is considerably larger than the attenuation of the fibre produced with the powder-in-tube technique. This loss contribution can be seen as the result of scattering due to the porosity of the 3D printed preform.

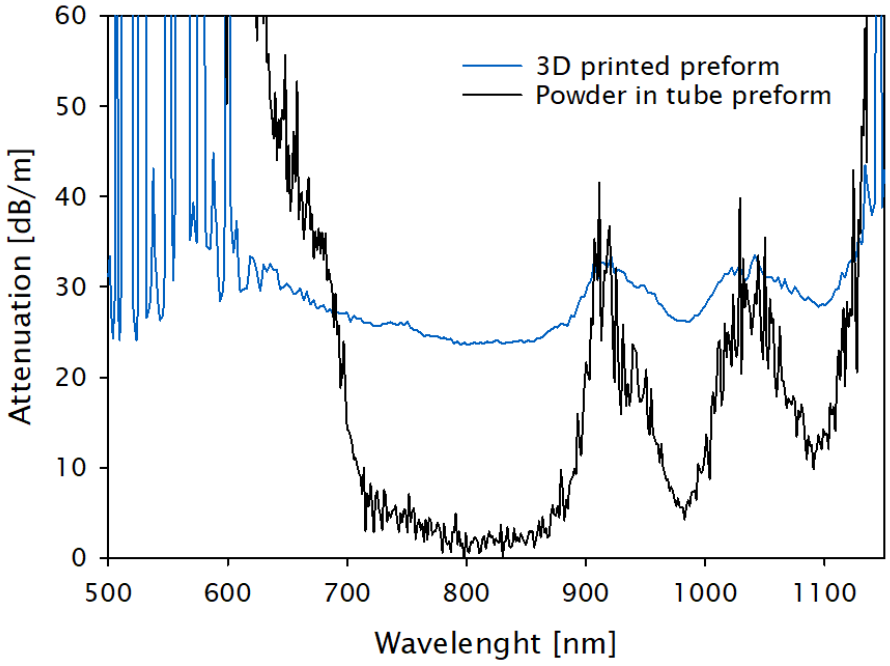

Figure 69. Attenuation of 3D printed silica fibre.

This is the first demonstration of silica optical fibres fabricated through 3D printing using the LPBF fabrication method and therefore form the starting point for the development of this technology. The attenuation levels show that there is still room for improvement in the LPBF process to reduce the optical losses to the same level

of the non-3D printed glass. This can be part of further development that will be discussed in section 0.

It is important to consider the quality of the starting material as this is crucial for the improvement of the optical losses. The silica powder used in this work contains a fraction of polycrystalline nature and hence suffered from crystallisation problems during the 3D printing and sintering processes. This can also be a significant contributor to the increased level of attenuation. The use of a fully amorphous silica powder is expected to improve the optical properties of the final optical fibre.

4.4.2 Optical fibres from 3D printed preforms in a single material and with complex geometries

3D printed silica preforms were fabricated using complex geometry such as PCF and ARF. Controlling the shape of the fibre during the fibre drawing process is the main challenge for optical fibre fabrication with this type of complex structure. The selected 3D printed preforms with complex structures were drawn accordingly to Figure 70 and Figure 71.

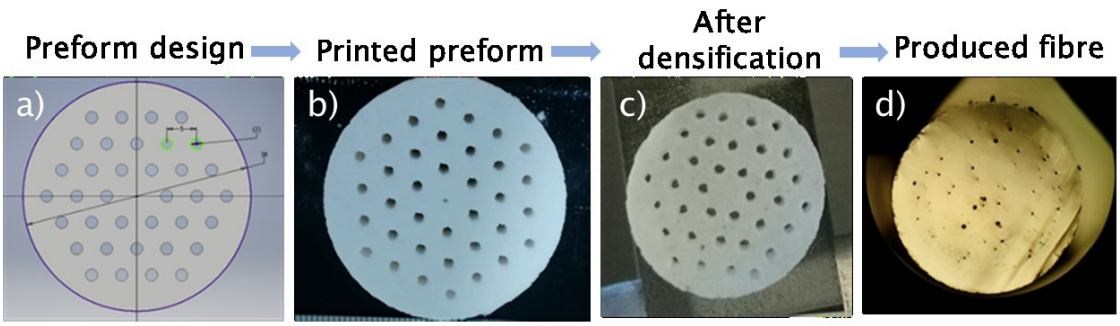

Figure 70. Optical fibre fabrication overview of a PCF from 3D printed silica preform.

A 3D printed preform structure of a PCF was heat-treated and drawn to a 200µm OD fibre. The fibre, A1238, was fabricated using a furnace temperature of 2100°C. Due to the internal lattice of the fibre, the drawing process was run at low tension to avoid breaking the fibre during pulling. In order to control the fibre lattice, the pressure control system was used to adjust the internal pressure of the preform aiming to stabilise the internal fibre geometry.

The fibre drawing process was targeted at an OD of 200µm. From the beginning of the fibre pull, samples of fibre were collected to monitor the internal lattice continually. The cross-sectional area of the drawn fibre A1238 is shown in Figure 70d, where it is visible that the air-holes were fully collapsed. The lack of the control

on the internal lattice of the fibre during the drawing process was a combination of two factors: the inhomogeneous heat distribution in the preform, the porosity of the 3D printed preform, material viscosity and law tension drawing caused the air holes in the fibre to close. Additionally, fibre drawing process development is necessary to improve the inner pressure conditions, allowing it to maintain the correct geometry, along with an improvement in the preform assembly process to eliminate interface gaps between the outer cladding and 3D printed silica preform.

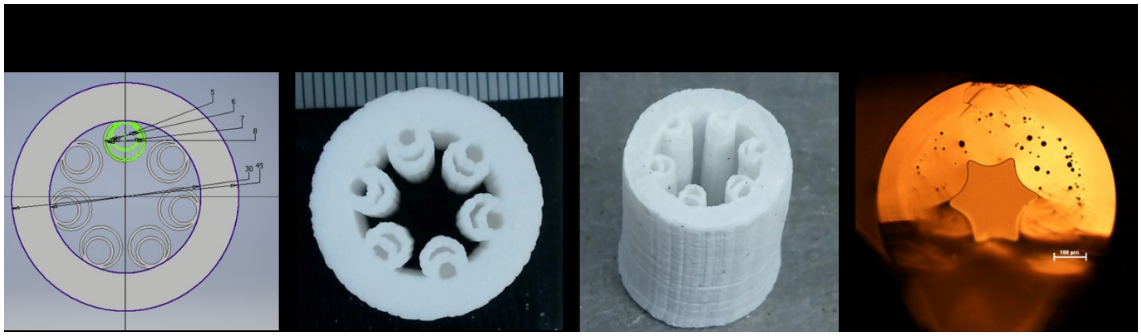

Figure 71. ARF drawn from 3D printed silica preform.

Figure 71 shows the ARF 3D printed silica preform with an OD of 18mm drawn into an optical fibre. The fibre A1275 was drawn to an OD of 750µm. Samples were also taken during this fibre drawing process, and the cross-sectional image of fibre A1275 shows that despite the cladding rings were fully collapsed, the hollow core region remained during the fibre drawing process. Further development is required to improve the internal pressure conditions that allow the stabilisation of the inner geometry.

4.4.3 Optical fibres from 3D printed preforms in multiple materials

A 3D printed preform with silica cladding and core composition of SiO_2 – GeO_2 mixed with 4mol% of germanium oxide was selected to demonstrate the capability to fabricate 3D printed preforms with multiple materials. The fibre was produced under the drawing conditions explained in section 4.4. Figure 72 shows the optical fibre with an OD of 100µm. In this figure, large porosities can be seen in the 3D printed doped core as well as the 3D printed silica cladding.

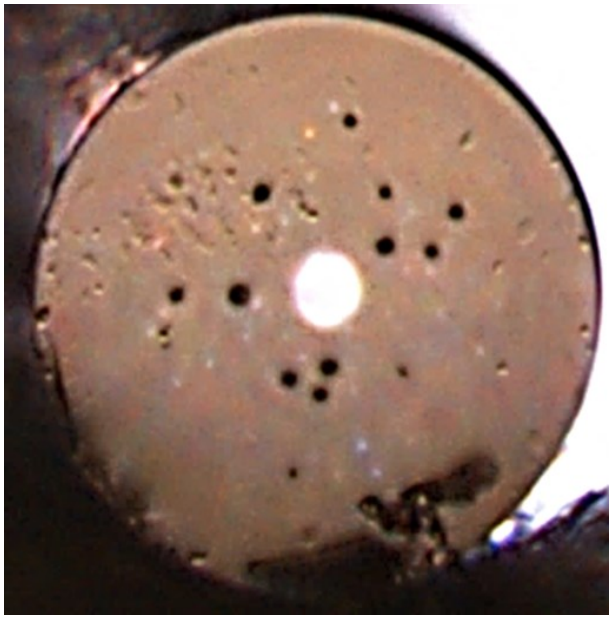

Figure 72. Multiple materials 3D printed optical fibre.

The optical losses of optical fibre with multiple materials were evaluated, showing attenuation of 8.3dB/m at 800nm. Figure 73 shows the attenuation curve of the first demonstration of 3D printed optical fibre using multiple materials fabricated by LPBF process.

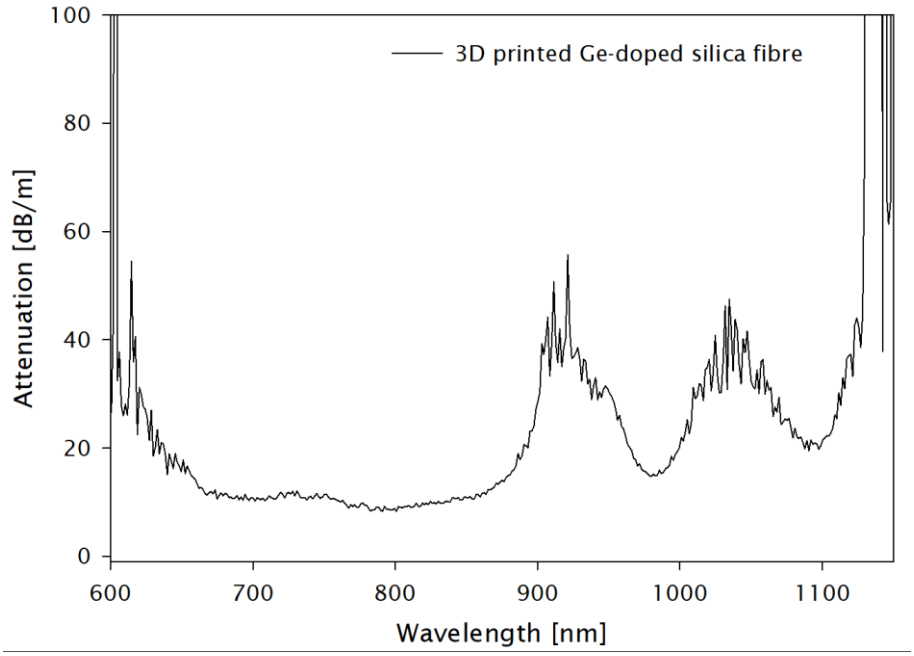

Figure 73. Attenuation of 3D printed germanium-doped fibre.

The attenuation reported in the 3D printed Ge-doped silica optical fibre is lower than the silica counterpart. The losses improved by approximately 36%. The enhancement of the attenuation values is due to the lower melting temperature of the Ge-doped powder composition, as reported in section 3.7, which effectively promotes a higher density material, and shows, therefore, lower defects levels after

the printing and sintering processes. However, there is still room for further optimisation of the fabrication process, particularly to eliminate voids in the cladding. In addition, the use of higher quality raw material can also improve the optical performance of the fibre.

4.4.4 Optical fibres from 3D printed preforms in multiple materials and complex geometries

A multi-core preform was selected to demonstrate the capability to 3D print multiple materials with complex structures. A fibre with an OD of 150µm was drawn from a 3D printed multicore preform with an OD of 16mm, which is shown in Figure 74. As explained in section 4.3, cores were printed horizontally for the first multi-core preform, and they presented structure stress and delamination as it can be seen in Figure 74. The preform was heat-treated and drawn to evaluate the effect of the printed deviation of the cores on the final fibre.

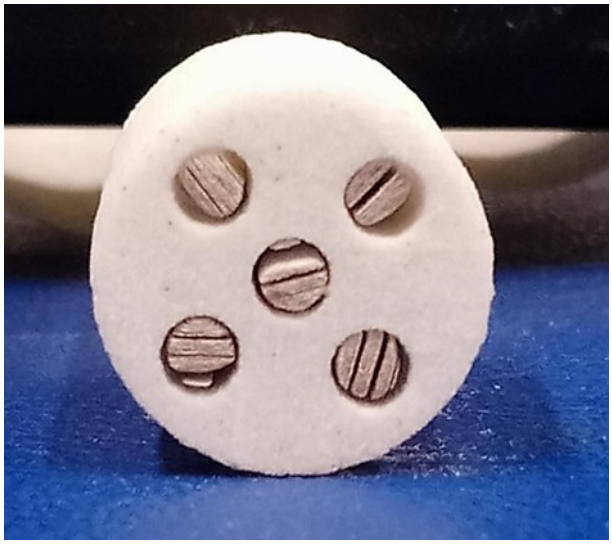

Figure 74. 3D printed multi-core optical preform.

The first multi-core optical fibre drawn from the 3D printed preform using LPBF is shown in Figure 75. The cross-sectional image of fabricated fibre shows large bubbles in the core region. The voids in the printed cores and the gaps between core-cladding caused large defects in the fibre. The use of the vacuum system did not compensate for the large gaps between the bodies, and the air kept trap between the layers.

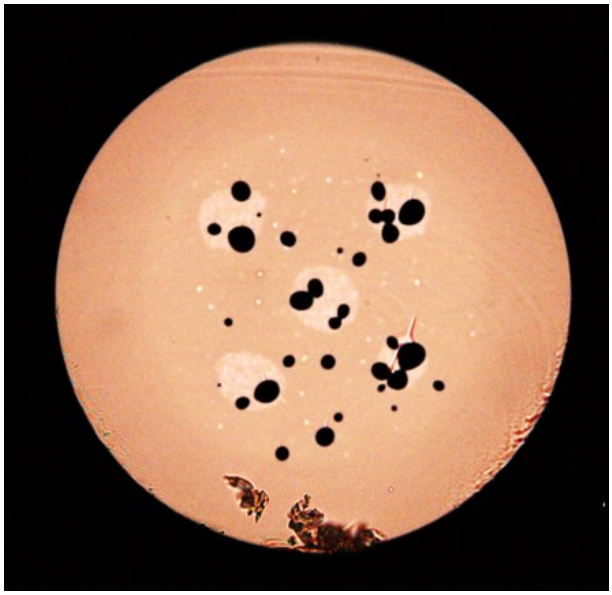

Figure 75. 3D printed multi-core optical fibre.

The modification of the core printing process eliminated the stress in the cores and significantly reduced the gaps between the core-cladding interfaces, as explained in section 4.3. Improve the fibre drawing conditions will be part of future work that can lead to producing a multicore fibre suitable for optical applications.

4.5 Summary

This chapter presented the development of the 3D printing process enabling the fabrication of preforms with a thin wall thickness. A minimum wall thickness of 1mm is needed to maintain the mechanical structure of the 3D printed preforms. This chapter also presented the first demonstration of PCF and ARF 3D printed preforms and fibres. The need for further development in the fibre drawing process has been identified.

The attenuation of optical fibres drawn from 3D printed preforms was compared and routes to improve the performance of these fibres has been discussed, the quality of the raw material is a key factor for improvement. The chapter also reports the first demonstration of a 3D printed optical preform with core and cladding using LPBF. The optical fibre from this preform has an attenuation of 8.3dB/m. In this chapter, the first demonstration of a multicore preform manufactured using 3D printing has also been presented.

Chapter 5 3D Printed Silica Preforms by Direct Ink Writing

In this chapter, we will discuss a direct ink writing (DIW) fabrication method that allows the use of a fully amorphous silica with a low impurities level. Unlike laser powder bed fusion (LPBF) process, the DIW is not limited by the material flowability on the use of nano-particulate powders. Nevertheless, the DIW fabrication method has different challenges that are discussed in the following sections.

For the purpose of this research work, it was important to validate that the use of fully amorphous starting materials improves the optical performance on the 3D printed glasses, as suggested in previous chapters.

The use of DIW for 3D printing glasses has been recently explored[90]. This technique requires silica powder to be mixed with a binder, which in this case is a resin called polydimethylsiloxane (PDMS). The mixture is prepared in a solvent, which has a high boiling temperature, called tetraethylene glycol dimethyl ether, also known as tetraglyme. The viscous mixture is then used as ink in a conventional DIW printing system. The 3D printed part is then dried inside a furnace to remove solvent residue. Once the solvent is fully evaporated, the 3D printed part is exposed to higher temperatures (>500˚C) to remove the binder by thermal reduction. Finally, the glass structure is sintered above 1500˚C.

In this chapter, the development of a colloidal ink of doped silica is discussed. In addition, the first demonstration of an active silica fibre fabricated using a 3D printing process is reported.

5.1 Micro-particulate Silica Powder

Prior to 3D printing, a study on the composition of the silica ink was performed, using micro and nanoparticles of silica. The first set of experiments was carried out using micro-particulate spherical silica powder, used in the LPBF process. Initially, the powder with larger particle size (30μm) was mixed with 1wt% of polymer binder and different ratios of SiO_2 and solvent, as described in Table 11. The composite was mixed for 3hrs in a centrifuge mixer at 450rpm.

Table 11. Silica ratio for composite mixture experiments (micro-particulate powder).

Particle size [µm]	SiO_2 [wt%]	Solvent [wt%]	PDMS [wt%]	Comments
30	15	84	1	Low viscosity
30	20	79	1	Medium viscosity
30	25	74	1	High viscosity

The mixture ratios, selected in this experiment, were based on the results with hydrophilic silica reported by Nguyen Du T. et al.[90] The mixture with 15wt% of silica presented liquid consistency, while the mixture with 25wt% of silica was too dry to flow through the extrusion nozzle. Due to its viscosity, ink with 20wt% was selected to evaluate the viability to print microparticles of silica using this method. Silica powders with a different particle size were mixed, as is described in Table 12. The densification of the composites was evaluated in the second stage of the experiment.

Table 12. DIW composite (SiO_2 + tetraglyme + PDMS).

Particle size [µm]	SiO_2 [wt%]	Solvent [wt%]	PDMS [wt%]
5	20	79	1
2	20	79	1
15	20	79	1
30	20	79	1

The composites were 3D printed using a modified Ultimaker^{+2} printer. A single layer was extruded on a quartz substrate using a nozzle with a diameter of 2mm. The printed geometry has a diameter of 10mm. The layers were dried in a furnace at a temperature of 100˚C for 100 hours in a N_2 atmosphere with a thermal cycle shown in Figure 76.

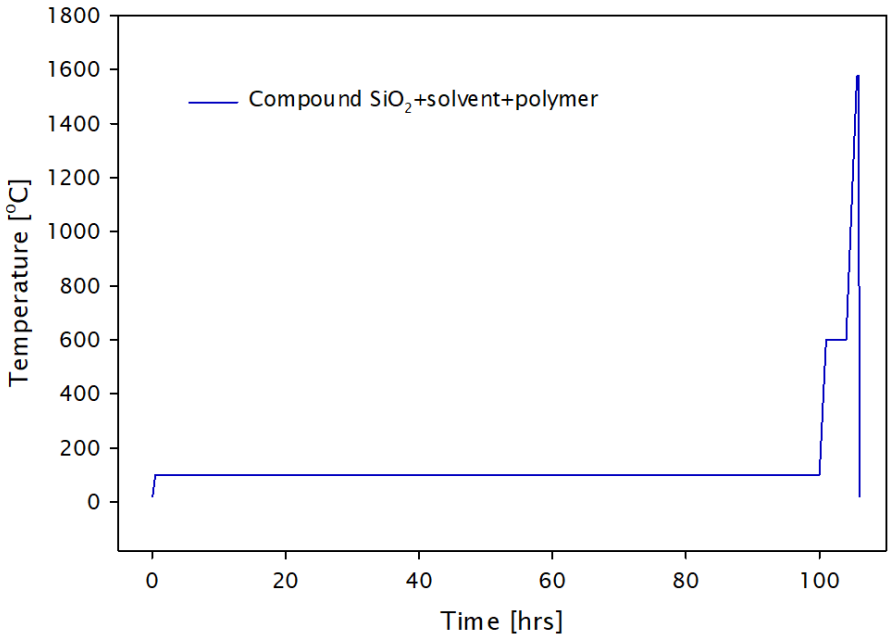

Figure 76. Thermal treatment for DIW composite (SiO_2 + tetraglyme + PDMS).

After the solvent evaporated from the 3D printed part, the samples were heated to 600˚C at a rate of 10˚C/min, where the temperature plateaued for 1 hour to allow thermal decomposition of the binder (PDMS). The samples were then exposed to a second increase in temperature with 10˚C/min ramping rate, reaching 1575˚C for 20 minutes. The samples were rapidly cooled down to room temperature.

The samples were analysed after the drying process using an optical microscope, and a SEM was used to investigate the topography of the samples after the consolidation process (see Figure 77).

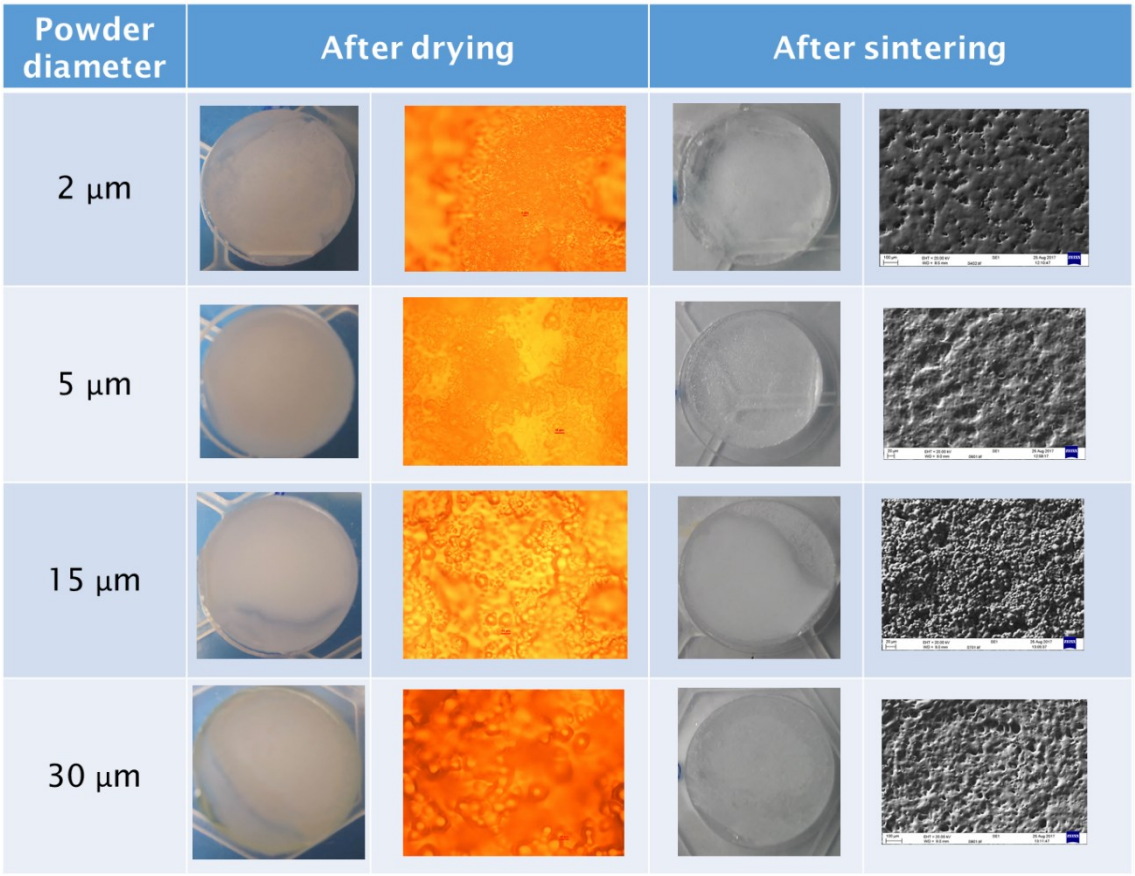

Figure 77. Effect of particle size in DIW composite (SiO_2 + tetraglyme + PDMS)

After the drying process, samples show a formation of agglomerates, which can be seen in the optical microscope images. An improvement in the transparency and topography of the sintered samples can be observed when powder with a smaller particle size was used.

A secondary experiment was performed to evaluate the contamination of PDMS in the composite and validate if the roughness observed in the densified samples is related to the thermal decomposition of the polymer and the by-products associated with it. Silica powder and solvent were mixed without adding PDMS as described in Table 13. A centrifuge mixer was used to mix the components for 3hrs at 450rpm.

Table 13. DIW composite (SiO_2 + tetraglyme).

Particle size [µm]	SiO_2 [wt%]	Solvent [wt%]	PDMS [wt%]
5	20	80	-
2	20	80	-
15	20	80	-
30	20	80	-

The produced composites were extruded in a glass substrate by the 3D printing process explained in previous experimentation. However, the thermal treatment

and the densification process was modified since the composites did not contain PDMS. The thermal cycling of the process is shown in Figure 78.

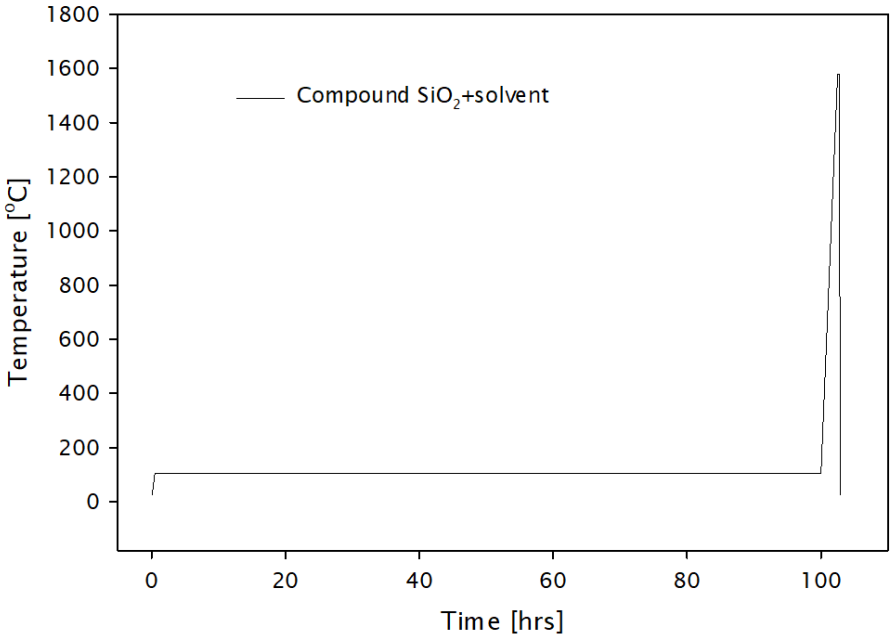

Figure 78. Thermal treatment for DIW composite (SiO_2 + tetraglyme).

After the drying process, the samples were analysed using an optical microscope. A SEM was used to investigate the topography of the samples after the consolidation process (see Figure 79). The samples from this experiment exhibited a noticeable lower density after the drying process. Nonetheless, the samples had adequate mechanical stability to continue with the densification process.

As shown in Figure 79, the samples no longer exhibit the formation of agglomerates after the drying process. Similar to the previous experiment, where PDMS was added to the composite, transparency and topography of the densified samples improves when powder with smaller particle size is used.

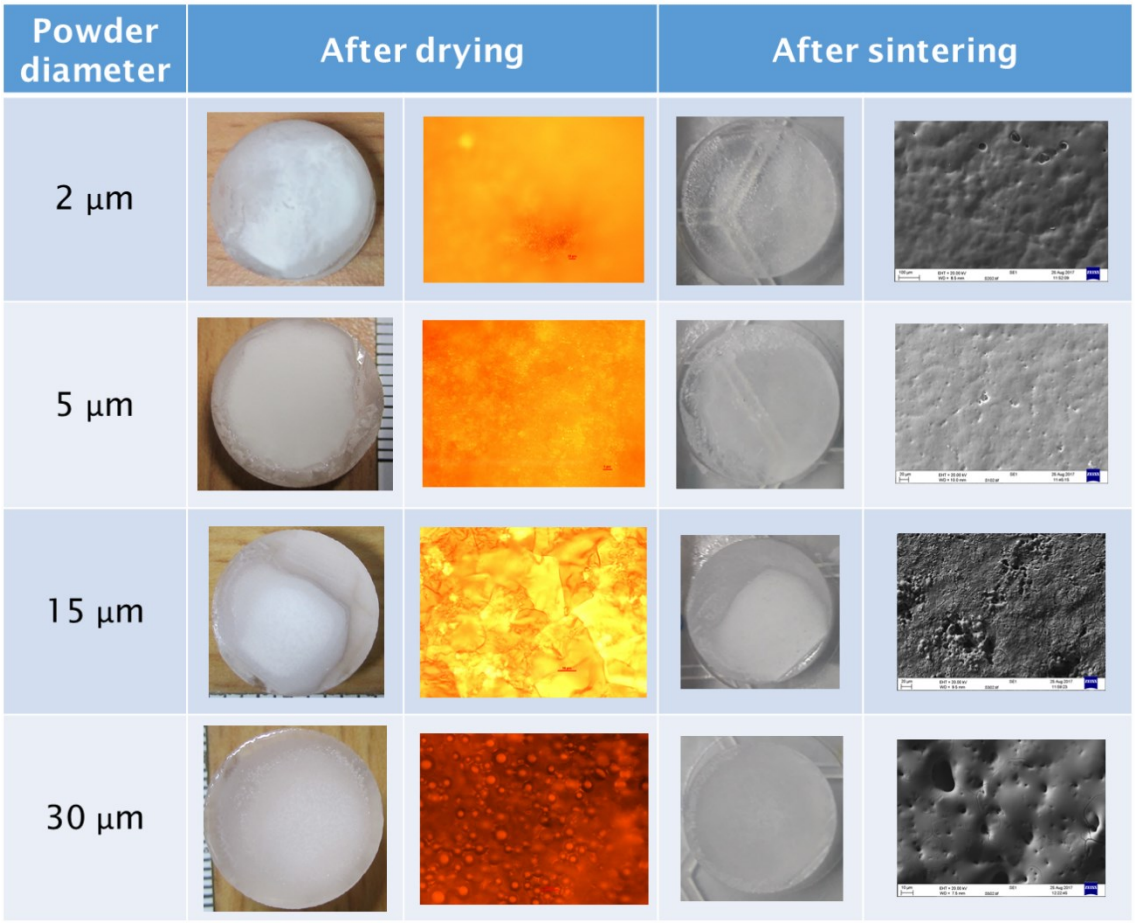

Figure 79. Effect of particle size in DIW composite (SiO_2 + tetraglyme).

5.2 Nano-particulate Silica Powder

The previous experiments showed that the use of powders with smaller particle size improves the densification of the printed parts. Therefore, nano-particulate powders were explored, and its results are reported in this section.

The viscosity of the silica compound can be controlled by adjusting the solvent-solute ratio. In addition, it is important to monitor and control the detrimental effects in the surface roughness of the deposited layers due to the thermal decomposition process of the PDMS, as it was observed in section 5.1. Therefore, nano-particulate silica powder was mixed at different ratios of SiO_2 and solvent (tetraglyme), adding 2wt% of polymer binder in the composites, as described in Table 14. Following the previous mixture recipe, the components were mixed in a centrifuge mixer at 450rpm for 3 hours.

Table 14. Silica ratio for composite mixture experiments (nano-particulate powder).

SiO_2 [wt%]	PDMS [wt%]	Tetraglyme [wt%]	Viscosity	Density [g/cm^3]
6	2	92	Low	0.4294
12	2	86	Low-Medium	0.6963
13	2	85	Medium	0.8401
15	2	83	Medium	0.8587
18	2	80	High	N/A
20	2	78	High	N/A

The colloidal inks were extruded and deposited in a glass substrate using a Ultimaker^{+2} printer with a nozzle with a diameter of 2mm. Composites with a higher content of SiO_2 (18 and 20wt%) had a high viscosity, which prohibited the mixture from flowing through the deposition nozzle. In contrast, solutions with less than 6wt% of silica had low viscosity, and the composite was too liquid to remain the shape after the extrusion.

Composites with silica content between 6 and 15wt% had a medium viscosity, which allowed the material to be extruded through the nuzzle, whilst retaining the shape. However, the composite with 15wt% of silica was too dry to print a single layer as it can be seen in Figure 80*c*. A single layer of the colloidal ink, with 6wt% and 12wt% silica content, were deposited on the glass substrate as it is shown in Figure 80*a* and *b* respectively. The composite mixture with 12wt% of SiO_2 content presented better extrusion conditions than composites with less silica content

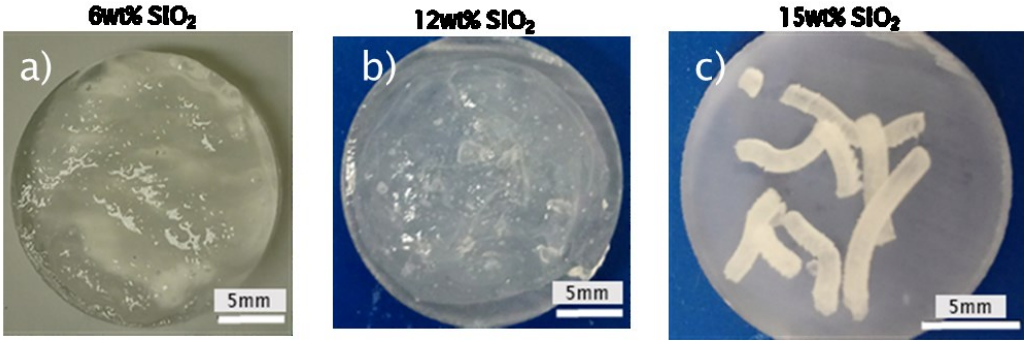

Figure 80. Composite mixtures extruded in a modified Ultimaker^{+2}, a) 6wt%, b) 12wt% and c) 15wt% of SiO_2.

A mass loss analysis was performed using ink samples with the content of 12wt% of silica. After the composite was deposited on the glass substrate, it was heat treated to eliminate the solvent and binder. The evaluation of the volume over time showed that the solvent is fully evaporated from the samples. The composite was deposited on two glass substrates with a diameter of 15mm and a height of 10mm. Both samples were placed inside a furnace at 21˚C. The temperature in the furnace

chamber was increased to a set value of 90˚C, at a ramp rate of 10˚C/min. The volume of one of the samples was regularly monitored during the first 40 hours. Figure 81 shows the change in volume measured in the 3D printed samples. The second sample was left in the chamber and measured after 40hrs, comparing the differences in volume between the two samples. No significant differences were found.

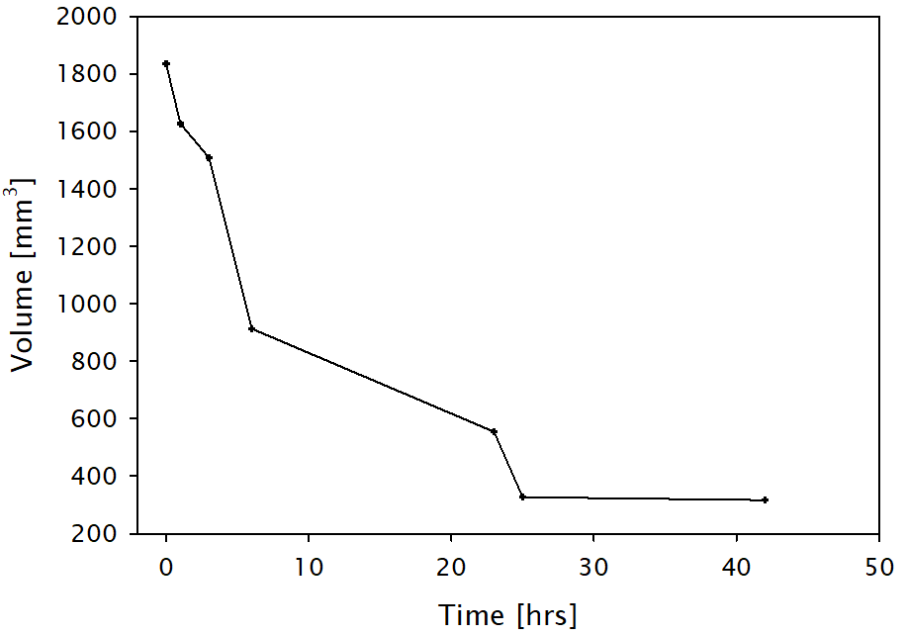

Figure 81. Effect of time in the change of volume during the drying process.

Dried samples presented a total volume reduction of approximately 6 times their original size. During the first 10 hours, the 3D printed bodies had a volume reduction of 50%. After approximately 23 hours in the furnace, the samples reached the maximum volume contraction. Prolonged heat treatment did then not contribute to further volume reduction. From the validation experiment of the drying process, an improved thermal treatment cycle was designed (see Figure 82).

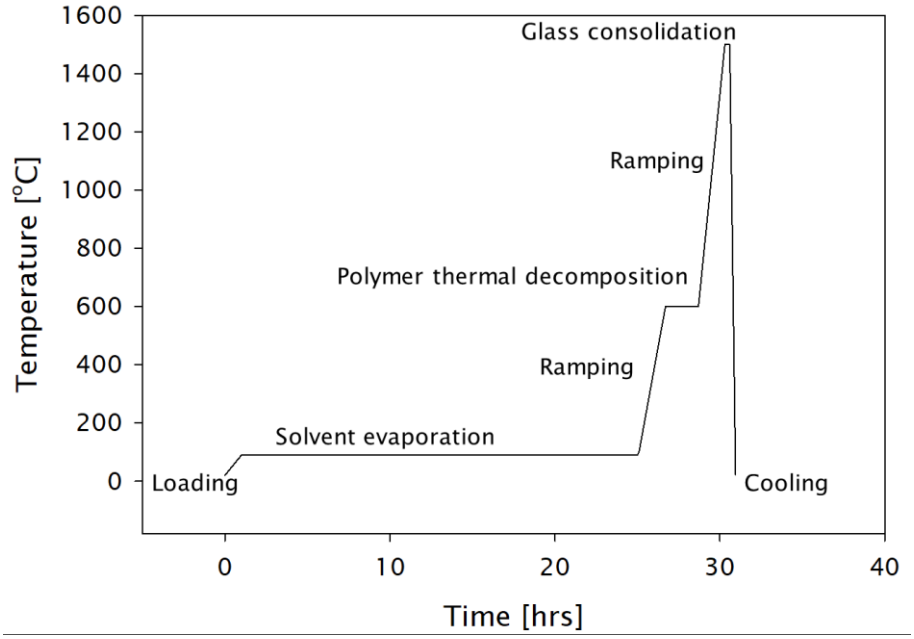

Figure 82. Thermal treatment for DIW composite using nano-particulate powders.

The control of the drying process governs the structural stability of the 3D printed body. It was observed that samples heat-treated at higher temperatures, than the ones described above, broke in the drying or burning stages. The same phenomenon happened at high temperature ramp rate.

Figure 83 shows the structural stability of 3D printed samples before and after the drying process using 6, 12 and 15wt% SiO_2. It is shown that the overall shape is retained in the entire range of compositions after the drying process.

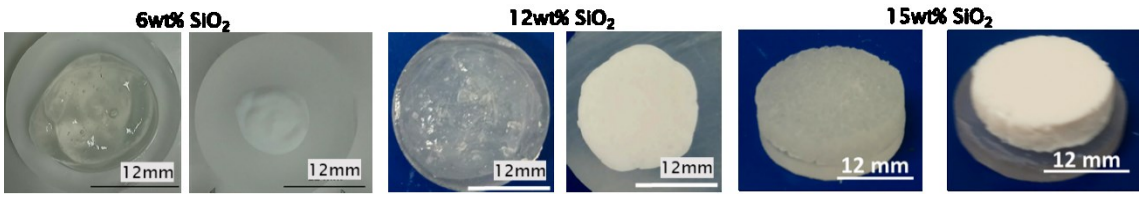

Figure 83. Structural stability of 3D printed composite by DIW with 6, 12 and 15wt% SiO_2.

The dried 3D printed samples were placed in a furnace with a controlled atmosphere of He and N_2 at ~100˚C. After the drying process, the temperature was increased to 600˚C at a rate of 10˚C/min. The thermal decomposition of the polymer binder was set to two hours in a controlled atmosphere. Finally, the temperature was increased at a rate of 10˚C/min, reaching the densification temperature of 1575˚C. The dwell of the sample in the last stage of the heat treatment was set to 20 minutes returning to room temperature with a quick cooling process.

The volume of the 3D printed samples was measured before the drying and after the consolidation process. Figure 84 shows the correlation of the mass loss of the colloidal ink with respect to the silica content in wt%.

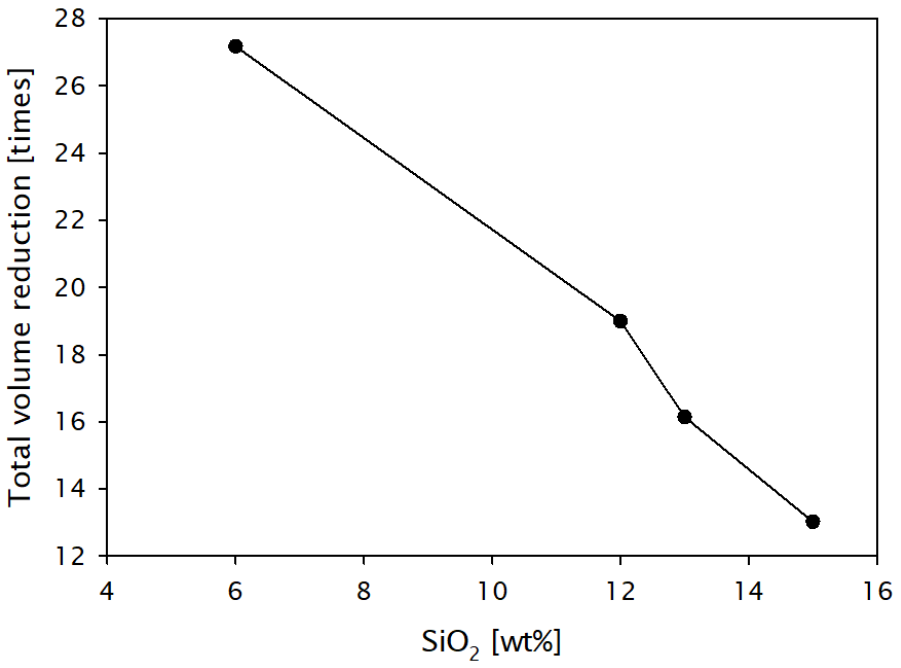

Figure 84. The mass lost in colloidal ink for SiO_2 content.

Samples with high solvent content presented a size reduction above 25 times their original size after the sintering process, while samples with 15wt% of silica had a volume reduction of below 13 times with respect to the original 3D printed part.

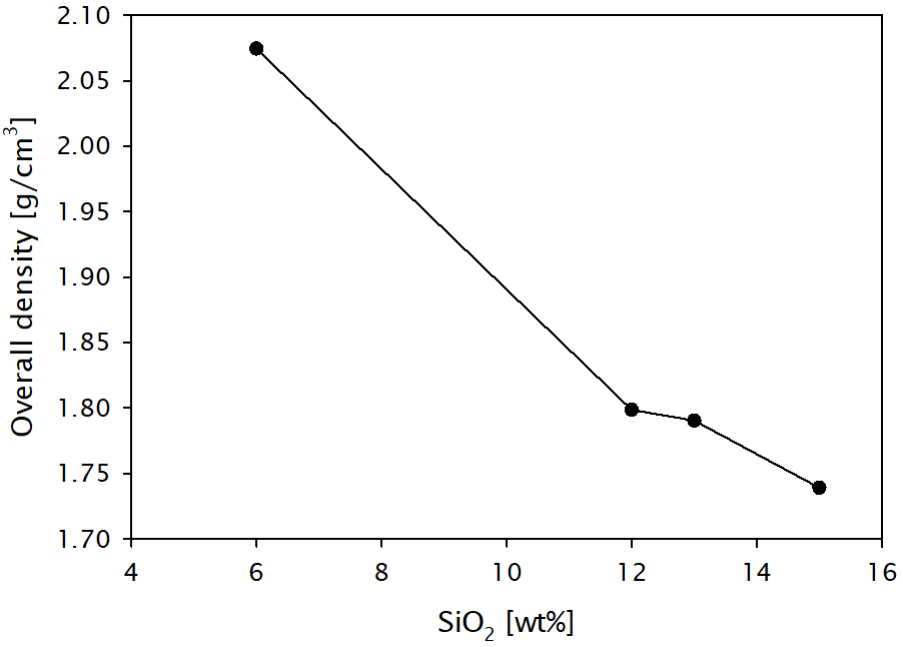

Figure 85. The effect of wt% of silica in the overall density of the glass formation process.

Figure 85 shows the densities obtained from the 3D printed silica samples. All the samples were fully densified, producing a fully transparent glass. Samples with low silica content exhibited a higher density than the samples with high silica content in the compound. It was observed that the samples with low silica content have a larger reduction in volume.

5.3 3D Printed RE doped silica fibre using DIW for laser applications

A silica 3D printed optical preform was fabricated using DIW, following the fabrication process for 3D printing silica colloidal ink and post-process the printed part, densifying the transparent glass. The preform was fabricated using a colloidal ink of 12wt% SiO_2, 2wt% PDMS, 85wt% of tetraethylene glycol dimethyl ether and 1wt% of rare-earth (RE) in chloride form with a purity of 6N. A modified 3D printer Ultimaker^{+2} was used to deposit the composite mixture in layers with a thickness of 500µm and a constant printing speed of 40mm/s at room temperature. A 2mm nozzle was used to print a cylindrical CAD model, which was heat-treated using the thermal cycle showed in Figure 82. A full densification process was achieved, obtaining a fully transparent glass structure shown in Figure 86.

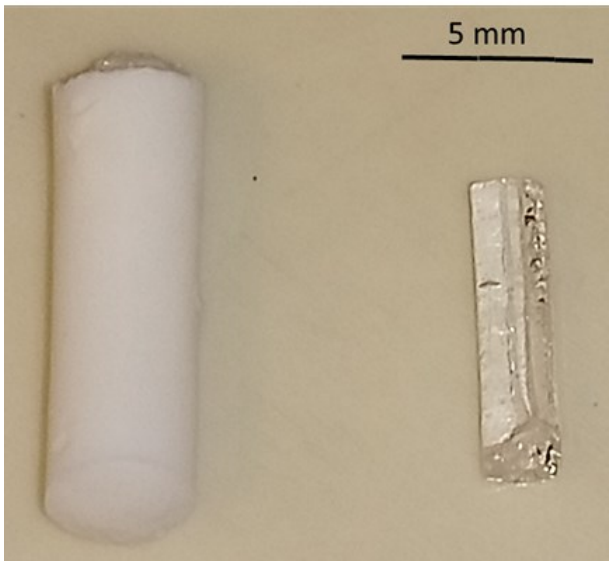

Figure 86. 3D printed erbium-doped silica glass.

The 3D printed erbium-doped silica preform was drawn into an optical fibre, and its characterisation is presented in the following sections. Similar to section 4.4, the 3D printed doped preform was placed inside a fluorinated tube that was used to provide the refractive index contrast between the core and the cladding of to the fibre. After assembling the preform, it was drawn into a fibre using a 2000˚C

furnace on a fibre drawing tower. This resulted in a multimode erbium-doped optical fibre with an outer diameter (OD) of 100µm and a core diameter of ~50 µm. The characterisation of the fibre is reported in the following section.

5.3.1 Fibre characterisation

The sample was analysed using energy-dispersive X-ray spectroscopy (EDX). The compositional analysis confirmed the incorporation of erbium into the silica glass. The transmission of the optical fibre was measured using an oscilloscope signal analyser (OSA) and a white light source (WLS) to evaluate the absorption in the core region caused by the rare-earth doping. The transmission spectrum of the fibre A1329 is shown in Figure 87 The absorption spectrum of this fibre presents characteristic absorption features of Er^{+3} ions with a main absorption at a wavelength of 980 and 1535nm.

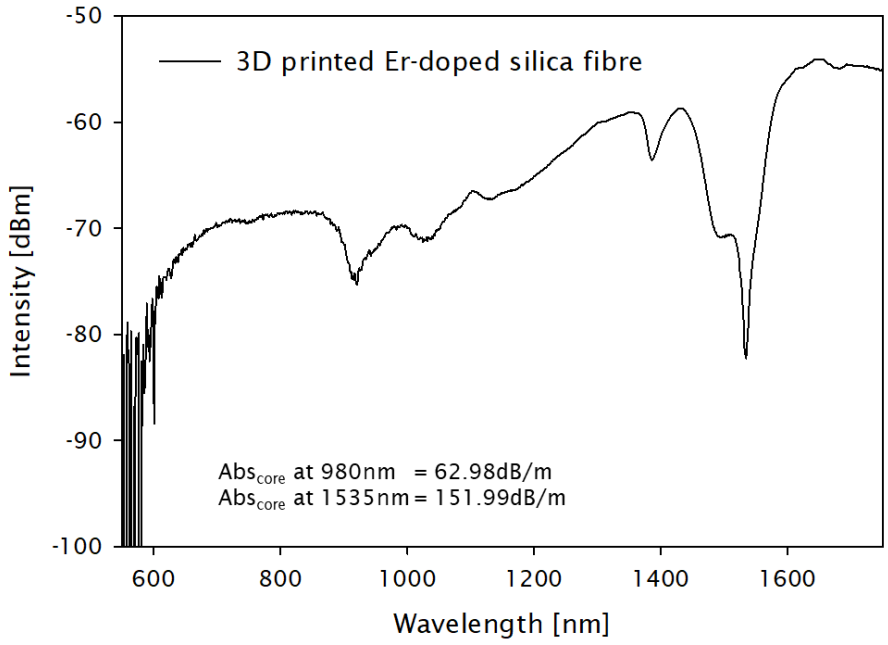

Figure 87. The transmission spectrum of 3D printed erbium-doped silica fibre.

Absorption values of 62.98dB/m at 980nm and 151.49dB/m at 1535nm are reported. The transmission spectrum shows additional absorptions at ~1380nm and ~1030nm, which are likely caused by contributions of residual OH, PDMS and impurities from the starting materials.

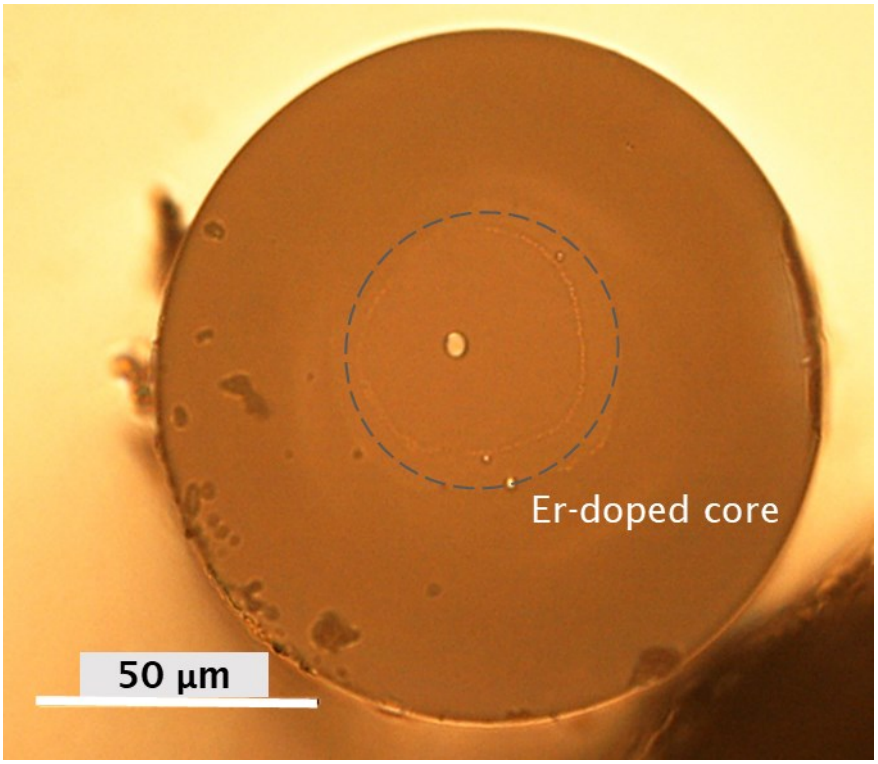

Figure 88. Erbium-doped silica fibre drawn from 3D printed preform.

Figure 88 shows the cross-sectional area of the fibre. The refractive index contrast was expected to be low due to the small contribution of the rare-earth to the refractive index of the core. However, the external fluorinated tube and the erbium-doped core have a sufficient contrast to allow the fibre to be characterised.

As mentioned at the beginning of this chapter, one of the motivations of exploring this fabrication method was to evaluate the optical performance of the optical fibres while using fully amorphous materials. Figure 89 presents the attenuation measured in the fibre.

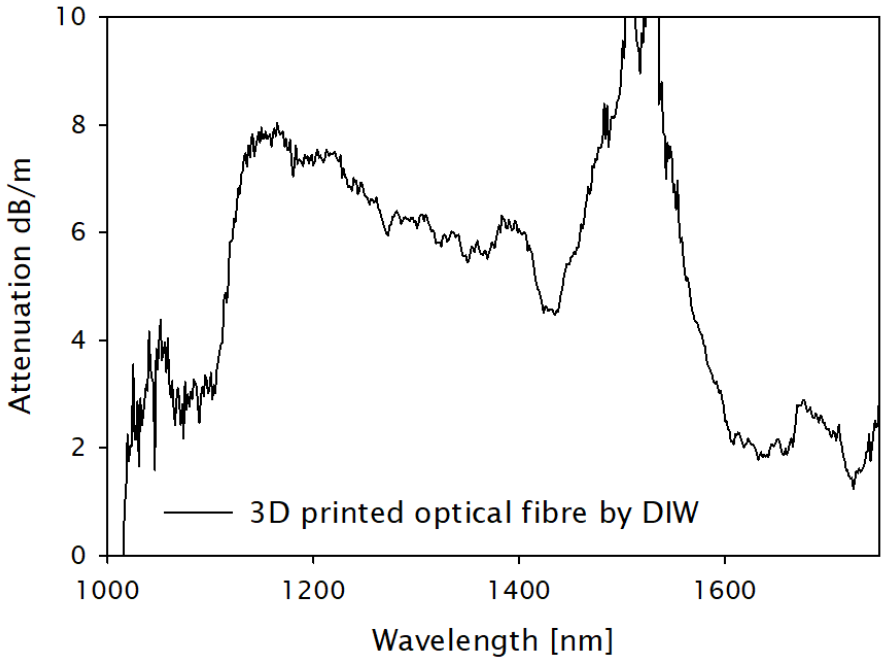

Figure 89. Attenuation of 3D printed Er-doped silica fibre.

The 3D printed optical fibre, which was fabricated using fully amorphous starting materials, presents an attenuation level of ~3bB/m at 1100nm. This value is a considerable improvement compared to previous attenuation levels, shown in Table 15.

Table 15. Attenuation level of 3D printed silica fibres

Material	Attenuation at 1100nm
3D printed amorphous silica	~3
3D printed spherical silica powder	~28
Silica spherical powder	~12
3D printed Ge-doped silica	~20

Finally, an initial spectroscopy study was carried out, which is an indicator of the lasing capabilities and expected performance of the erbium-doped optical fibre. It was expected that the lifetime values of the fabricated fibre are shorter than the typical values reported, owing to the fact that no network modifiers (aluminium (Al) or phosphorous(P)) were added to the silica matrix. The lack of network modifiers is expected to have detrimental effects in the spectroscopic characterization of the fibre due to the potential non-fluorescent deactivation of the ions populated in the excited and meta-stable states.

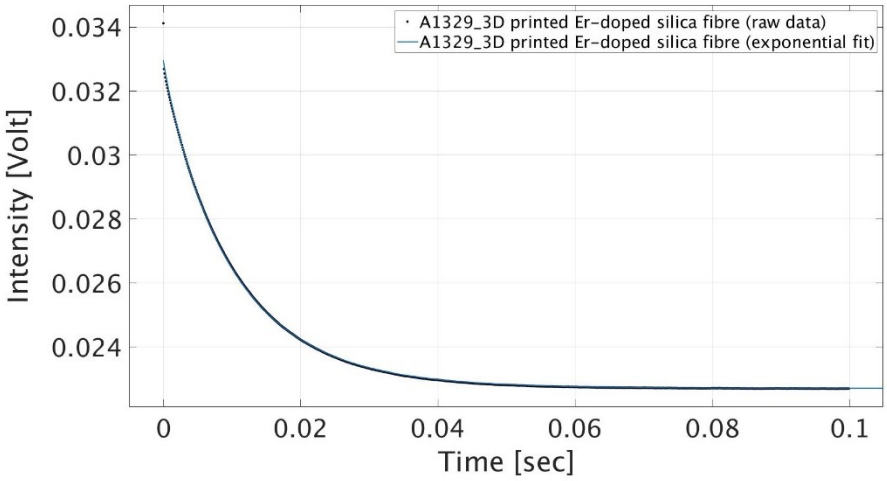

Figure 90. Lifetime fitting for 3D printed Er-doped fibre.

Figure 90 shows the lifetime fitting curve obtained from the 3D printed erbium-doped fibre. The lifetime value calculated from the experimental data is ~10ms, which is consistent with the reported lifetime values for erbium-doped silica glasses.

$$f(x) = a * \exp(-(b * x)^p) + c$$

Equation 7. Stretched exponential decay

The mathematical model used for the lifetime calculation is described in Equation 7. The lifetime was obtained using a modulated976nm laser diode, with a duty cycle of 10% and a pulse width of 10ms.

5.4 Summary

The DIW process for manufacturing 3D printed silica optical preforms has been demonstrated. The use of micro-particulate powder showed that the smaller particle sizes improve the roughness and reduced defects in the printed parts. The development of a colloidal ink of nano-particulate hydrophobic silica powder was successfully demonstrated. The fabrication of 3D printed parts using a silica ink by a DIW process was demonstrated.

Drying and densification processes of the printed parts were reported. An evaluation of the mass loss and the densification of the printed colloidal ink was performed. It was validated that the use of fully amorphous silica powder as starting material for 3D printed optical glasses, improving the optical performance of the fabricated optical fibres. The fabrication of a 3D printed erbium-doped silica optical fibre has been successfully demonstrated. Absorption, attenuation and lifetime of the erbium-doped optical fibre were reported.

Chapter 6 Polymer Preforms Fabricated by Fused Deposition Modelling

Additive manufacturing processes have become popular due to their flexibility, accuracy and repeatability, as discussed in **Error! Reference source not found.**. These advantages can overcome some of the current limitations in the optical fibre fabrication, such as low yields as well as expensive and time-consuming processes. The previous developments on 3D printing of optical preforms and fibres based on polymers have been attempted using traditional polymers and equipment, such as fused deposition modelling (FDM) and stereolithography (SLA), which are readily accessible at low cost. Hence, one of the aims of this research is to produce polymeric optical fibres (POF).

This section of the thesis proposes the development of 3D printing processes that will enable the fabrication of speciality polymer optical fibre using innovative materials for demanding applications such as biomedicine and sensing.

Polymer preforms with complex structures manufactured using FDM are reported. Optical fibres were drawn from the 3D printed COC preforms and were characterised in the THz region.

6.1 Development of polymer preforms fabricated by Fused Deposition Modelling (FDM)

FDM is a process where a thermoplastic is extruded through a heated nozzle, creating objects layer by layer when the material cools down and solidifies as described in **Error! Reference source not found.**. These materials are suitable for optical fibre fabrication due to their capability to be re-melted and pulled from the preform in the final shape of an optical fibre. The thorough characterisation was carried out in order to select the most suitable material to explore this fabrication method. The properties of interest include melting temperature (T_m), glass transition temperature (T_g), and refractive index.

Polymers such as ABS, PET-G, PMMA and COC have been used previously in FDM as reviewed in Chapter 2. Thus, these materials were selected, and their optical and physical properties were characterised. All polymers were available as filaments for

COC, which is also known as TOPAS. This material is supplied in pellets; which made it necessary to produce the filament in-house, as reported in section 6.2.1.

Although the thermal and mechanical properties of the polymers mentioned above are well known, the specific characteristics of the polymer filaments produced from different manufacturers can vary. Therefore, a differential scanning calorimetry (DSC) analysis of the polymers was performed to validate the deviations between the measured values and those provided in the specification's datasheet.

Table 16. DSC analysis of polymers for FDM 3D printing method.

Material	Spec T_g [°C]	Spec T_m [°C]	Meas T_g [°C]	Meas T_m [°C]	FDM nozzle temp target
PET-G	80	240	83.99	242.88	250
ABS translucent	105	230	104.77	232.06	240
PMMA	100-120	270	99.5	237.55	240
COC	80	210	76.44	199.3	205

Table 16 shows the glass transition temperature (Tg) and the melting point (Tm) of the different polymers. Validate these temperatures on the polymers is important to establish the printing parameters window. These temperatures dictate the polymer features during the deposition.

In addition, the refractive index (n) of the polymers was measured with a multi-wavelength analyser, to ensure the optical requirements for the final fibre are met. The results are shown in Table 17.

Table 17. Refractive index of materials used for 3D printing processes[119-122].

Material	n (Literature)	n (Measured)
PET-G	1.5850	1.5840
ABS translucent	1.5400	1.5120
PPMA	1.4887	1.4915
COC	1.5319	1.5300

The refractive index is a parameter which is not usually provided by the filament suppliers, but was experimentally measured for PET-G, PMMA and COC and compared with the reported values in the literature. There are many different types of ABS reported in the literature with a variety of additives added to the different grades of transparency and colours, which explains the discrepancy in refractive index observed in ABS.

6.1.1 Preliminary analysis for 3D printing polymer optical preforms

The printing condition for specific filaments is usually given by the manufacturers of the material and equipment. Nevertheless, a comprehensive analysis of the 3D

printing process and its impact on the final optical preforms was performed. The main challenge of the FDM method is to create smooth interfaces between the deposited layers, which can cause scattering points within the fibre by the microscopic defects in the printed. In addition, the selection of the printing pattern can influence light transmission[101]. The printing pattern is set by default on the equipment software, but it is possible to modify the printing sequence and explore the effect of different printing patterns in the solid structures[123]. Since this was not part of the scope of this project, the effect of modifying the printing pattern can be explored in future work.

The main printing parameters in an FDM process are the printing speed, nozzle diameter, feeding rate, printing lattice and layer resolution. These variables will define the overlap between the deposited stripes and hence the quality of the overall print. The individual layer thickness is a crucial parameter for any set of fabrication variables selected for the process. Figure 91 demonstrates the effect of the layer thickness during the printing process.

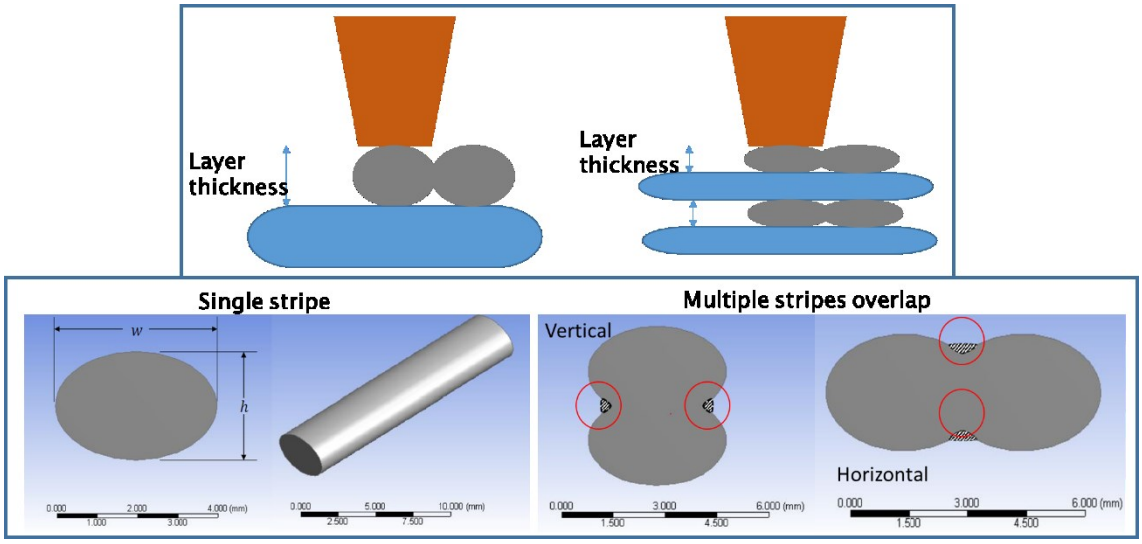

Figure 91. Effect of the layer thickness in the FDM process.

The effect of the nozzle diameter in the printed part was studied. Circular samples with a diameter of 20mm and 5mm in height were printed in an Ultimaker+2. The nozzles diameters used in this experiment were 400, 600 and 800µm. The layer thickness varied from 100 to 400µm for each nozzle. The results of this experiment are presented in Figure 92.

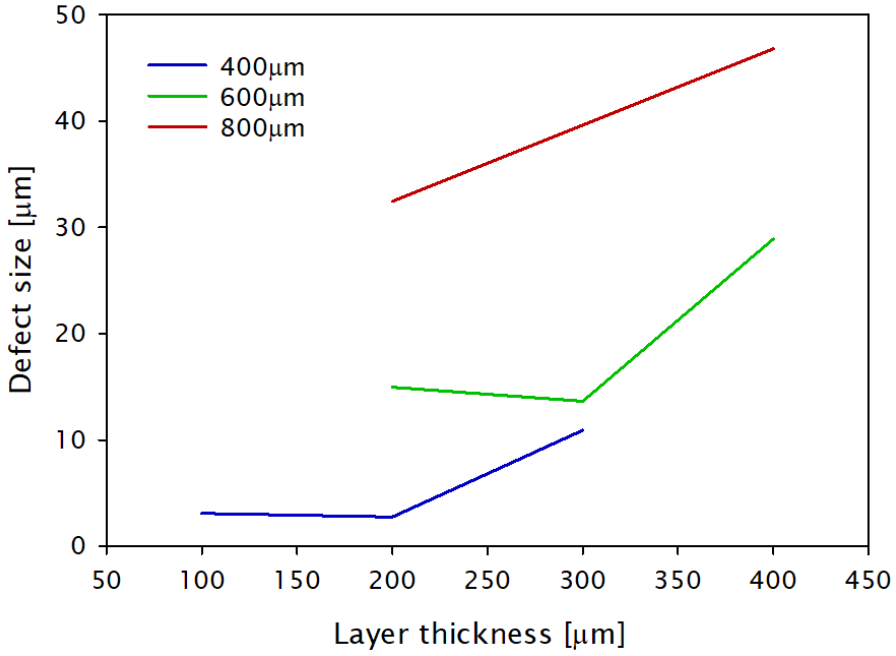

Figure 92. Effect of the nozzle size and layer thickness in the defect size between printed stripes.

It was observed that the combination between the nozzle diameter and the layer thickness has an effect on the size of the defects between the printed stripes. The 3D printed solids presented smaller defect size between the stripes when the layer thickness was smaller than the nozzle diameter. Based on the experimental data, a relation between the layer thickness (h) and the nozzle diameter (w) is proposed as described in Equation 8 shows.

$$h < \frac{1}{2}w$$

Equation 8. Layer thickness for FDM process.

Using the information from Figure 92 and following Equation 8, a nozzle diameter of 400µm and a layer thickness of 100µm were selected as process parameters for the following experimentations.

PMMA filament was print to evaluate the effect of different printing patterns or lattices to the transparency of the 3D printed parts, circular samples with a diameter of 20mm and a height of 5mm were printed in two different patterns: a) orthogonal pattern and b) concentric pattern as shown in Figure 93. These patterns will be used in the fabrication of COC fibres to evaluate the impact of the printing strategy in fibre performance.

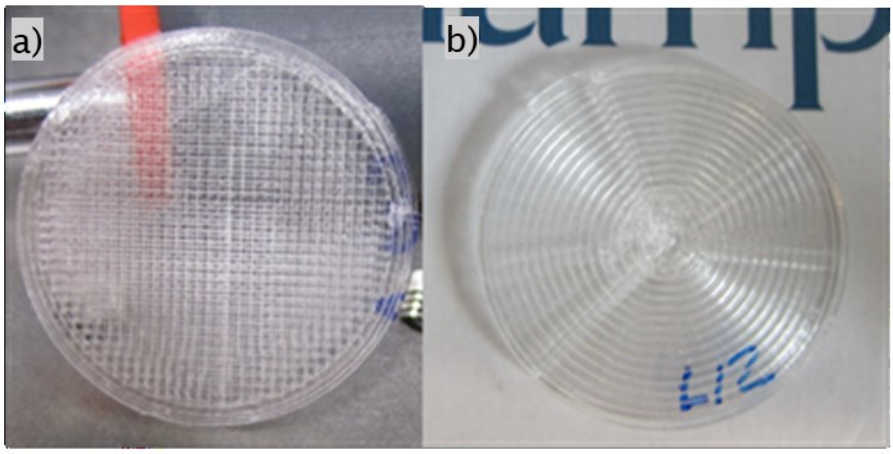

Figure 93. PMMA samples printed with different strategies; a) orthogonal pattern; b) concentric pattern.

The samples printed with concentric pattern presented better transparency than the solids printed using the orthogonal pattern. This can be explained due to the more significant number of intersections produced by the orthogonal pattern, causing multiple scattering points and resulting in lower transparency. Nevertheless, optimisation on the fabrication parameters can improve transparency while using orthogonal patterns in the printing process.

3D printed PMMA preforms were produced. They had an OD of 20mm and a length of 100mm. The solid was printed at a temperature of 260˚C with a printing speed of 50mm/s using an orthogonal pattern. Figure 94 shows the 3D printed optical preforms fabricated on PMMA by FDM.

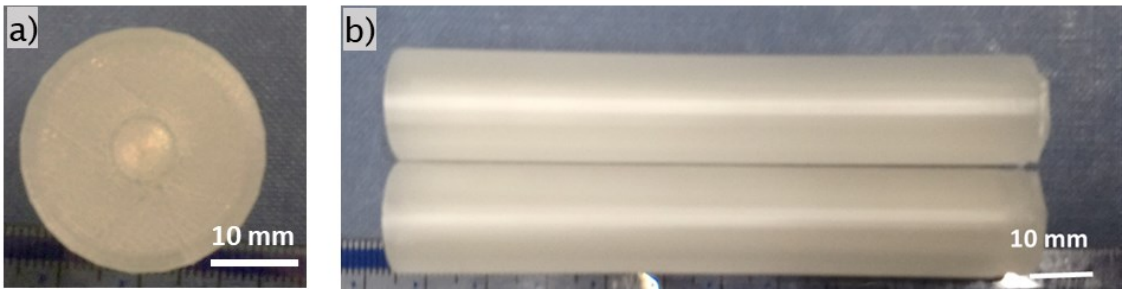

Figure 94. 3D printed PMMA optical preform.

This demonstrated the capability of the FDM process to produce 3D printed PMMA optical preforms with complex structures. Preforms with hexagonal PCF and equiangular spiral PCF structures[124] were produced. The spiral PCF design was developed by A. Agrawal from the City University of London, and it was fabricated as a result of research collaboration. The solids were printed at 50mm/s with an orthogonal pattern at a temperature of 260˚C. The 100mm long preforms had an OD of 30mm. The preform with a spiral design has three rings holes in an arrange

of five arms with a spiral radius (r_o) of 5mm, an air hole radius (r) of 3mm and a spiral angle of 30 degrees, as is shown in Figure 95.

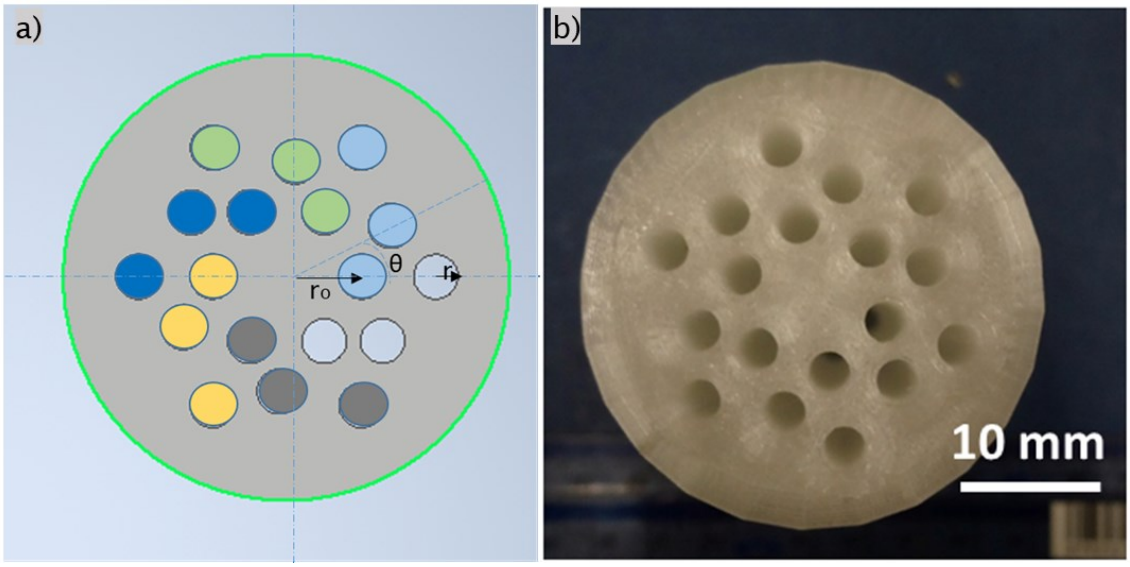

Figure 95. 3D printed PMMA preform using spiral PCF design; a) CAD model; b) the printed preform.

This preform successfully demonstrated the capabilities of the FDM process to produce PMMA optical preforms with solid and complex geometries.

6.2 3D printing of polymer optical fibres for THz applications

COC or TOPAS is an amorphous polymer based on cyclic olefin monomers and ethane. This polymer has become an interesting material for several applications. It present optical advantages over polymers due to its characteristics such as high T_g, optical transparency, low shrinkage, low moisture absorption, and low birefringence[119]. The use of this amorphous polymer for optical fibres for sensing and biomedical applications has gained attention within the research community[125,126].

TOPAS can usually be found on the market as a pellet or bulk material. However, an only very limited number of TOPAS suppliers provides the material in the form of filament for FDM processing. Therefore, it was decided to produce the filament in-house. The polymer filament was produced from pellets prior to the fabrication of the preforms. The fabrication process of the COC material is described in the following section.

6.2.1 COC Filament fabrication

Since the limited availability of COC for FDM process presented a challenge for this research, an in-house process to produce the required filament was developed. A desktop extruder from 3DEVO was selected to develop the filament fabrication process, which is shown in Figure 96.

The equipment was adapted to extrude the Cyclic Olefin Copolymer TOPAS 8007X10. The extruder has a complex heating system along with the extruder worm, which can be controlled independently in four heating zones over a temperature range from 25 to 300˚C.

Figure 96. 3DVO desktop extruder.

The polymer pellets are fed to an extruder worm through the feeder hopper. Then, the extruder worm transports the raw material across the heating system, where the polymer is softened and transported to the nozzle, as shown in Figure 97. The melted polymer is fed through the nozzle forming the filament. The fast cooling system after the extrusion process prevents crystal formation in the filament during the process. The diameter of the filament is controlled using the feedback signal of a diameter gauge. The filament is then collected in a spool by a winder system.

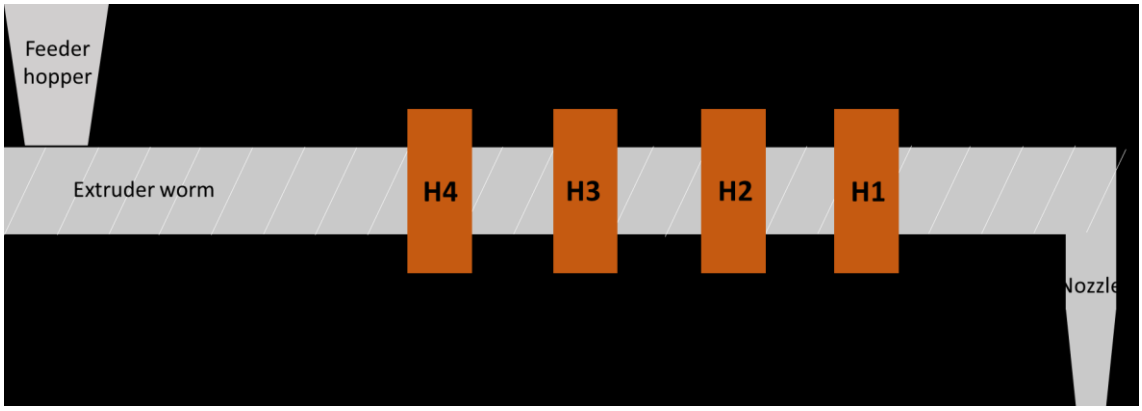

Figure 97. Schematic of the polymer path across the heating system.

Using the information from a DSC analysis, the temperature effect in the polymer was analysed. Figure 98 shows the range of temperatures required for processing the COC in the extruder.

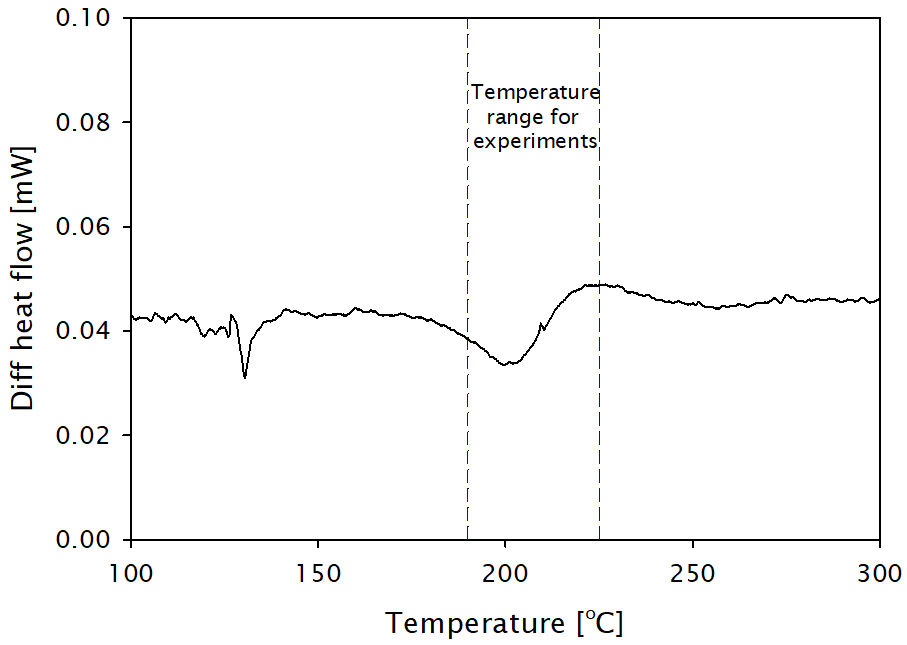

Figure 98. DSC of COC polymer for the extrusion process.

The filament fabrication process was developed, analysing the thermal condition of the process. During this experiment, all the heaters were set to the same temperature as described in Table 18.

Table 18. Different temperature settings to analyse the effect of uniform temperatures in the polymer extrusion.

Heater 1 Temperature [˚C]	Heater 2 Temperature [˚C]	Heater 3 Temperature [˚C]	Heater 4 Temperature [˚C]
190	190	190	190
195	195	195	195
200	200	200	200
205	205	205	205
210	210	210	210
215	215	215	215
220	220	220	220

In this experiment, the effect of the temperature in the transparency of the COC material was observed. There is a noticeable improvement in the transparency of the material as the extrusion temperature increases, which is shown in Figure 99.

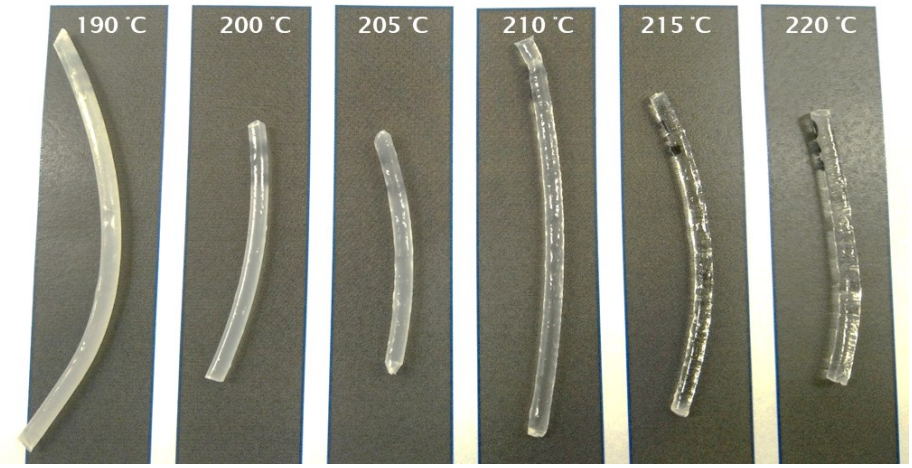

Figure 99. Effect of temperature in the transparency of TOPAS.

The OD deviation with respect to the nominal diameter was also monitored during this experiment. Figure 100 shows the diameter deviation on the filament for different extrusion temperatures.

The transparent filament, which was fabricated with a uniform temperature above 210˚C, presented an OD deviation >200µm with respect to the nominal diameter of 3mm. As seen in Figure 99, the material started to form bubbles inside the filament. Since this impairs the internal structure of the fibre, and make the drawing process more difficult, further experiments were performed to improve the trade-off between transparency and the formation of bubbles. Particularly, the effect of non-uniform heating temperatures where analysed.

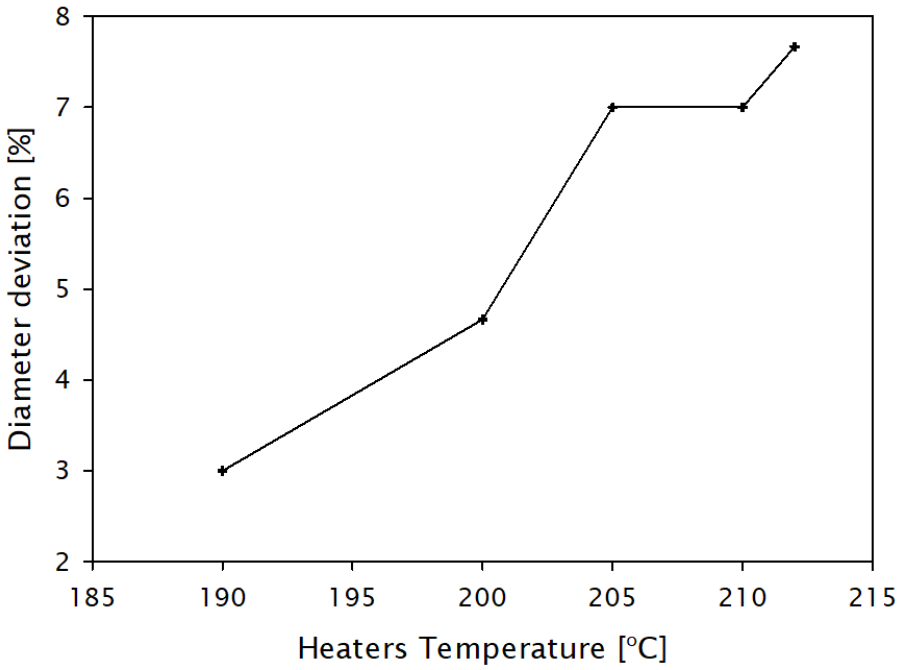

Figure 100. Effect of temperature in diameter deviation.

An experiment with a decreasing temperature along the heating zones (from H4 to H1) was carried out. Table 19 shows the temperatures for each of the heaters during this experiment.

Table 19. Effect of decreasing temperature in polymer extrusion.

Heater 1 Temperature [°C]	Heater 2 Temperature [°C]	Heater 3 Temperature [°C]	Heater 4 Temperature [°C]
190	200	210	220
185	195	205	215
180	190	200	210
180	180	190	200

Decreasing the temperature on the heaters in the extrusion process produced elliptic filament. The high temperatures on the material at the beginning of the extrusion process created bubbles that got trapped inside the filament, causing a lack of uniformity in the extrusion process. Even though the temperature was reduced in the final section of the heating zone, the material was not cold enough before reaching the pulling system. Therefore, the filament was compressed while still soft, which resulted in the filament, forming an elliptical shape.

Finally, an experiment with an increasing temperature along the heating zones (from H4 to H1) was performed. The temperatures for each of the heaters are described in Table 20.

Table 20. Effect of incremental temperature in polymer extrusion.

Heater 1 Temperature [˚C]	Heater 2 Temperature [˚C]	Heater 3 Temperature [˚C]	Heater 4 Temperature [˚C]
220	210	200	190
225	215	205	195
230	220	210	200
235	225	215	205

A sequential increase in the temperature of the heaters produced a smaller OD deviation and good transparency characteristics when the heaters were set to H1=225˚C and H4=195˚C. This approached delivers the best results in the filament formation so far. The extrusion process with an increasing temperature in the extruder system allowed the production of COC transparent filaments with a controlled OD for 3D printing.

It is important to highlight that after the successful development of the extrusion process, several meters of COC filament was produced with the parameters described above. This filament was used to produce 3D printed preforms using FDM. Moreover, customised filaments can be easily fabricated, such as composite materials, mixed polymers or dopants can be added to create customised filaments for the manufacturing of speciality polymer optical fibres. The produced TOPAS filament was used to produce 3D printing preforms with solid and complex structures as described in the next section.

6.2.2 COC polymer preforms

After overcoming the challenge of COC filament market availability, by producing the filament in-house, this following section will focus on the fabrication of optical preforms. The use of COC polymer for optical fibres has caught the attention of the research community due to its broad transmission range from UV to NIR, which makes this polymer a versatile material for sensing and biomedical applications. Moreover, research has explored complex geometries such as PCF structures as well as using this polymer for terahertz applications[124].

Based on the FDM data from the preliminary analysis for PMMA in section 6.1.1, the fabrication parameters were adjusted for COC. The produced TOPAS filament was used to 3D print circular samples with a diameter of 20mm and a height of 5mm, using a layer thickness of 100µm. The effect of the process temperature on the printed layer was analysed, as shown in Figure 101.

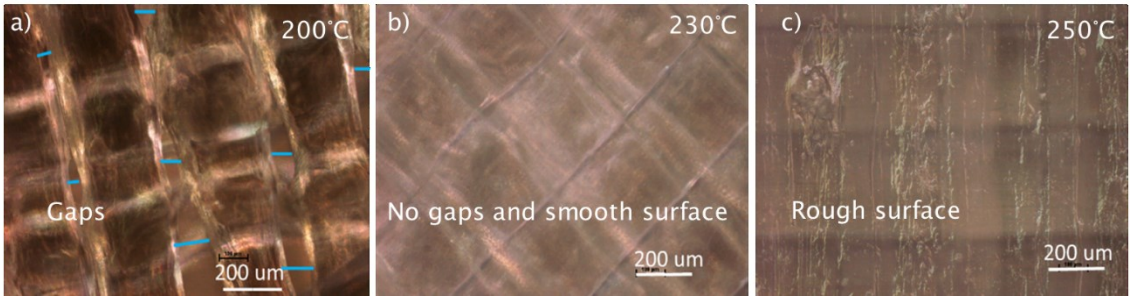

Figure 101. Microscope images showing the effect of nozzle temperature in COC 3D printed layers.

The printed cylinders were analysed using an optical microscope. These pictures indicate that samples printed with temperatures below 220°C in the nozzle displayed gaps between the deposited stripes. Samples printed with nozzle temperatures above 240°C showed signs of degradation of the polymer, indicated by the formation of bubbles and exhibiting a rough surface in the printed layers. Finally, samples printed with a nozzle temperature of 230°C showed a closed orthogonal structure without a rough surface.

Using the optimised fabrication conditions for COC a set of solid 3D printed optical preforms were produced for fibre drawing. The preforms had a length of 150mm and a diameter of 20mm. Orthogonal and concentric patterns were printed using a nozzle temperature of 230°C with a layer thickness of 100µm.

The solid preforms were drawn in CFATA – UNAM Mexico as part of research collaboration. The results of the drawing process are described in the next section.

6.2.3 Fibre drawing of COC polymer preforms

A fibre drawing tower for polymer preforms from CFATA-UNAM was used to produce the optical fibres from the 3D printed preforms fabricated in the ORC. The customised tower has a furnace with two heating zones that can be controlled independently. At the exit to the furnace, the equipment has a diameter control unit ZUMBACH with a precision of ±1µm[127].

For the drawing process, the upper furnace zone (UZ) was set to 200°C, and the lower zone (LZ) was set to 165°C. The drawing process of COC optical fibres was successfully demonstrated by CFATA-UNAM team. Optical fibres drawn from orthogonal and concentric 3D printing patterns were produced and sent back to Southampton for their characterisation, which is described in the following section.

6.2.4 Polymer optical fibre characterisation

The COC optical fibres fabricated from 3D printed preforms were characterised using terahertz-time domain spectroscopy (THz-TDS). In THz-TDS time-dependent measurements of the amplitude and phase of the THz electric field are recorded. The study of COC fibres in the THz region provided the refractive index and the THz spectrum transmission from THz time-domain scans.

The THz-TDS setup, which was used to characterise the TOPAS optical fibres, is shown in Figure 102.

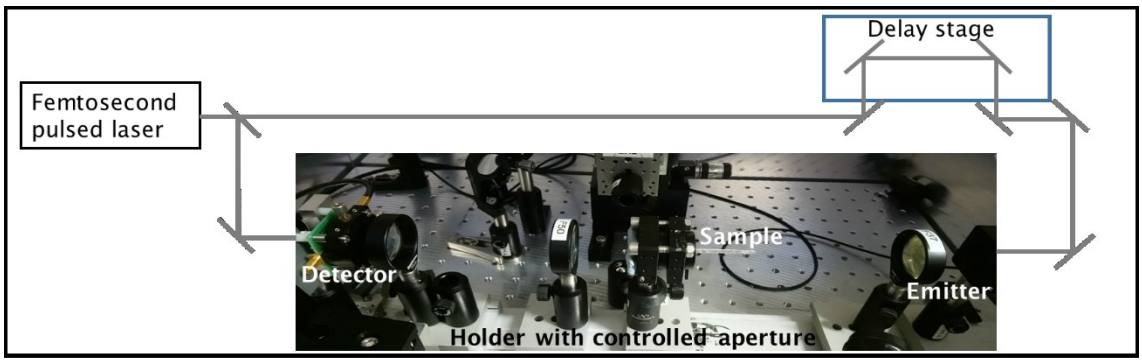

Figure 102. THz-TDS experimental setup.

The effective bandwidth from the spectroscopic data can be obtained in the range from 0.1THz to 1.0THz, limited by ambient noise and component alignment in the setup. The TSD system consists of a Tera-SED from Laser Quantum GMBH, which is a GaAs photoconductive emitter that emits broadband terahertz waves up to 2.5THz. The setup also has a detector, Menlo GMBH TERA8-1, which is a photoconductive antenna with a bandwidth capability of up to 4THz. A metal disk fitted to the fibre diameter was limiting the transmission of the signal to only the straight path through the waveguide.

In THz-TDS time-dependent measurements, amplitude and phase of the THz electric field, are recorded. Should material be present in the THz beam path, the THz electric field will be modified due to the dielectric properties of the material.

A reference scan of air was taken by measuring the time domain scan for the electric field of a THz pulse passing through the iris without a sample present. Then, a second-time domain scan for the electric field of a THz pulse was taken when the sample of the 3D printed fibre was placed in the iris. It was possible to determine the average refractive index of the samples, comparing the differences between the sample and reference scan,

The average refractive index of the fibres was determined by measuring the time difference between the main pulse in the reference and the sample scans (Δ t) using the Equation 9, where c is the speed of light and L is the sample length.

$$n = 1 + \frac{c\Delta t}{L}$$

Equation 9. Refractive index.

An average refractive index of 1.5319 was calculated from the experiments' s data, which correspond to the theoretical refractive index of COC of 1.53. Therefore, the transmission in THz of the 3D printed fibre was validated.

As explained in section 6.1.1, COC preforms were printed in two different patterns: orthogonal and concentric. To calculate the attenuation of the fibre depending on printing pattern was evaluated by a cutback method using the THz-TDS set up. This data is recorded in the time domain of the THz pulse. The Fourier transform is used to determine the transmission spectra of the samples in the frequency domain. The attenuation is estimated from the difference in the amplitude of the signal at a specific frequency between the largest and shortest measured samples. This method was applied for both fibres, and its attenuation is reported in Figure 103.

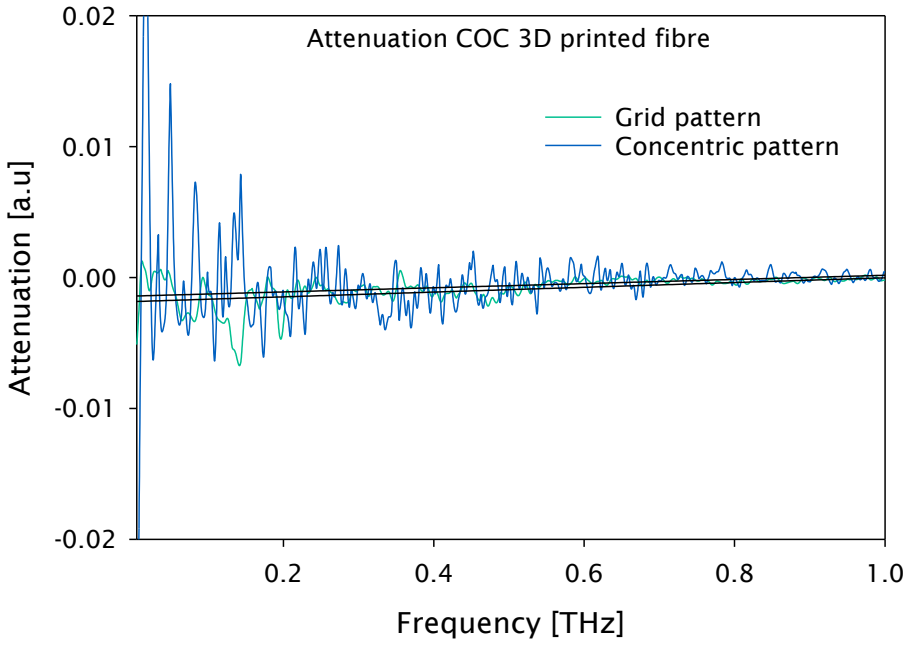

Figure 103. Attenuation of 3D printed TOPAS fibres in THz region.

The fabricated fibres transmit in the range below 0.5THz with attenuation similar to the noise level above 0.8THz. Fibres with an orthogonal pattern exhibit higher attenuation than those with a concentric pattern.

6.2.5 3D printed COC preforms with complex geometries

Finally, the fabrication of 3D printed TOPAS preforms with complex structures was proposed. A spiral PCF preform was produced with a process temperature of 230˚C and a layer thickness of 100µm. The printing speed of 50mm/s was used with an orthogonal printing pattern. The preform had an external diameter of 21mm, and three rings with five arms. The spiral radius (r_o) was 3.2mm, and the air hole radius (r) was 2.2mm, with a spiral angle of 30 degrees. Figure 104 shows the 180mm long preform fabricated in TOPAS with the spiral PCF design.

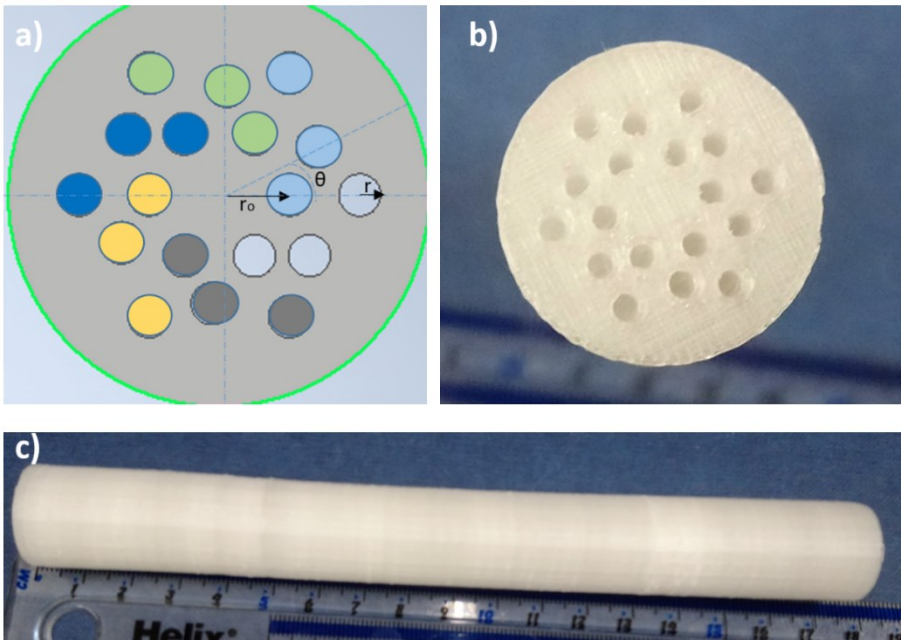

Figure 104. 3D printed COC preform using spiral PCF design; a) CAD model; b) cross-sectional image of the printed preform; and c) image of the longitudinal section.

An additional COC preform with complex geometry, using a hexagonal PCF design, was fabricated using the home-made filament. A 190mm long 3D printed preform was produced at a process temperature of 230˚C and with a layer thickness of 100µm. The printing speed was set to 50mm/s, and an orthogonal printing pattern was used. The 3D printed preform had a diameter of 25mm with a distance between the air holes (Λ) of 3.15mm. The air hole radius was 1.3mm. The produced preform is shown in Figure 105.

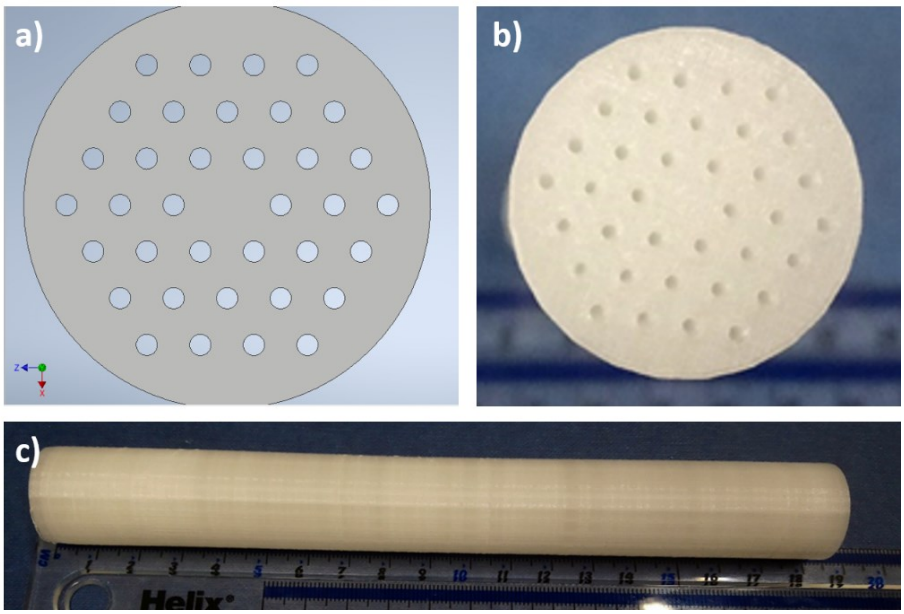

Figure 105. 3D printed COC preform using hexagonal PCF design; a) CAD model; b) cross-sectional image of the printed preform; and c) image of the longitudinal section.

The fabrication of 3D printed optical preforms with complex geometries in COC was successfully demonstrated. The accuracy of the developed 3D printing process is ±0.05mm with respect to the CAD design. The air hole diameters can be produced without deformation for diameters above 1mm. Complex shapes can be produced with a good definition at the edges of the holes. The fibre drawing process and fibre characterisation from the final 3D printed preforms will be reported in future work.

6.3 Summary

3D printing processes for the fabrication of polymer optical fibres were performed and analysed. A variety of materials were analysed for preform and optical fibre fabrication. Optical and physical properties of the materials used in the 3D printing processes to fabricate optical fibres were discussed.

A range of thermoplastics to use in FDM processes were characterised. The FMD printing parameters were optimised for the successfully demonstrated fabrication of preforms using PMMA. The effect of layer thickness, nozzle size and printing patterns was discussed.

The limited availability of COC polymer was overcome by developing the filament fabrication process for TOPAS using a bulk material in the form of pellets. The demonstrated capability to produce specific filaments in-house opens up the

possibility to explore different materials such as composites, mixed polymers, or even adding dopants to the material.

The 3D printing process for COC was optimised using the preliminary experiments of PMMA as a reference. After a successful demonstration of 3D printing solid optical preforms in TOPAS, samples were sent to CFATA – UNAM Mexico for fibre drawing and the resulting fibres were characterised in the THz regime at the Optoelectronics Research Centre in Southampton. The optical characterisation showed that the optical fibres can transmit below 0.6THz and at a noise level of 0.8THz.

Finally, the fabrication of 3D printed preforms in COC using complex geometries in a spiral and hexagonal PCF designs were successfully demonstrated.

Chapter 7 Discussion

7.1 Laser Powder Bed Fusion (LPBF) for SiO2 and its applications

The results presented in chapter three and four correspond to the experimentation related to 3D printed silica powder using the LPBF method. The material was characterised, and the printing parameters were established for the 30µm spherical silica powder. The produced 3D printed silica porous bodies were post-processed with heat treatment, obtaining an amorphous 3D printed glass. Based on these results, 3D printed silica preforms were produced and drawn to fabricate optical fibres, which were characterised. The discussion of the reported results is contained in this chapter.

7.1.1 Silica powder characterization

The angle of repose technique evaluated the flowability of the silica powder. Powders with amorphous shape and spherical shape was evaluated. It was found that the powder flowability does not only depends on the particle morphology, but also the particle size. It was found that smaller particle sizes present poor flowability features and result in small groves, and many voids in the powder bed surface. Silica powder with irregular shape and average particle size above 40µm, presented better flowability, but the powder bed showed an irregular surface. The sharp edges of the powder caused voids in the powder bed.

Spherical powder presented a better flowability in larger particle size. The morphology of the spherical powder favoured the distribution of the particles, and the powder bed was even for 30µm particle size. In contrast, the powder beds from spherical silica powder with smaller particle size (<15) presented many cavities and a non-uniform powder bed density. Therefore, the 30µm spherical silica powder was chosen as a feedstock powder due to the smooth and even powder bed it produced. The chemical composition of this powder was reported.

The powder has low levels of impurities from elements such as Na, K, Mg and Fe, which are not desirable for optical fibres. From the Additive Manufacturing (AM) point of view, the powder can be considered as a high purity silica powder; however, it is not comparable with the purity of silica soot use in optical fibres, which is produced in a chemical vapour deposition method (CVD). This soot does not

present any other impurity, because it forms a chemical reaction when the SiCl4 is oxidised producing SiO_2. These differences are also clear in the thermogravimetric analysis of the powders. The spherical silica powder presents a lower softening and melting point than soot silica. This difference can be explained due to the impurities present in the spherical powder. Therefore, it was foreseen a high attenuation level in the optical fibres fabricated from a 3D printed preform using LPBF. However, it was reasonable to expect that the impurities of the powder might be removed during the densification and drawing process. Unfortunately, it was found in the XRD analysis that the chosen powder has a crystalline nature, which also causes losses in the final fibre and prohibited to remove the impurities in the powder. These powder's features were taken into account in the optical fibre characterisation.

7.1.2 LPBF printing parameters and characterization

One of the aims of this thesis was the fabrication of porous silica bodies for further densification. Due to the intrinsic properties of silica glass, such as glass transition temperature, melting temperature, viscosity and surface tension, it was not considered to fully melt the powder in the LPBF process. Therefore, the premilitary experiments evaluated the effect of the CO_2 laser beam in a silica powder bed, showing that low energy density applied on the surface of the silica powder could form small sintering necks, which indicates a solid-state bonding mechanism. It was observed that the particles coalesce on a more uniform stripe-like shape and well-defined geometries are obtained when the laser exposure is performed at a low power level. As the power laser was reduced, stable and well-defined stripes were achieved at a relatively low linear energy density of ~25J/m. These preliminary experiments provided information for a home-made LPBF apparatus.

Equipment based on laser powder bed fusion (PBF) was built and used to process the spherical silica powder. Single tracks were printed using a CO_2 laser beam at a wavelength of 10.6µm. The effect of the printing variables was analysed. The experiment was set to vary the laser power from 10 to 100W, and scanning speeds from 100 to 500mm/s. The linear energy density applied to the powder bed was calculated by EL=P/V; where P is the laser power, and V is the scan speed. The energy density delivered to the powder affects the definition of the edges and the strength of the printed tracks. The printed tracks at low laser powers and scan speeds above 100mm/s did not have mechanical stability to be taken out of the building chamber, and the parts broke during the removal process. The low energy

density applied to the powder by the laser beam did not provide enough heat to enable bonding between the particles and no sinter neck was formed. In contrast, stripes printed at higher linear energy density, for instance at 60W laser power and 100mm/s scan speed, presented massive irregularities in the stripe edges and its large cross-section area. This is the result of molten silica forming concave structures, which can be an indication of potential warpage in a single printed layer.

Single layers were printed using a CO_2 laser beam at a wavelength of 10.6um. The experimental variables were ranged between 20 and 100W for the laser power and the scanning speed from 10 to 1300mm/s. The thickness of the 3D printed areas was measured, and the morphology of the layer was evaluated accordingly to the energy density applied to during the printing process. The energy density delivered to the power bed depends on the laser power and the exposure time of the laser beam on the material. Therefore, it is crucial to understand the relation of the laser power, the scan speed and their effect on the layer thickness, given by the energy density equation: Es=P/V*h; where P is the power of the laser, V is the scan speed, and h is the distance between the printed tracks, also known as hatch distance. It was observed from the experiments that printed layers of 100µm thickness presented well-defined edges, better surface homogeneity and higher overall density. Printed layers with an energy density below 0.4J/mm^2 were broken and did not show neck formation. Whereas, printed layers with an energy density above 0.9J/mm^2 form rough surfaces with irregularities and large voids between the printed tracks. Low level of warpage can be found in layers printed with an energy density between 0.7 and 0.8J/mm^2.

3D printed cubes of 10mm per side were produced using SiO_2 spherical powder using a CO_2 laser beam at a wavelength of 10.6um. The experimental conditions established three variables: laser powers with a range between 20 and 60W; scan speeds in a range from 100 to 500mm/s, and layer thickness between 0.05 and 0.15mm. The hatch distance was fixed at 300µm. The overall density of the printed cubes was estimated based on their mass and their measured dimensions. The volumetric energy density applied to the printed cubes was correlated to their density; evaluating the printed parameters of the porous silica bodies. The volumetric energy density can be expressed as ED= P/V*t*h; where P is the power of the laser, V is the scan speed, and h is the hatch distance, and t is the layer thickness.

The evident warpage presented in some 3D printed structures presented poor cohesion between layers when high energy density was applied in the printing

process. The overall density of the printed solids improves significantly at higher scan speeds, whereas silica bodies printed below 300mm/s exhibit a high level of deformation due to warpage and poor overall density. The use of higher scan speeds produces a more compact structure, and consequently, a higher overall density is noticeable in the printed body.

There is a barely noticeable effect in the printed volume structures by modifying the laser power. The energy density on the silica powder varied from 2J/mm^3 to 6.6j/mm^3, when the laser power was varied. Even though the overall density of the printed bodies under these conditions present a slight change, it does not show evidence of detrimental warpage on the samples due to the increase in laser power. Therefore, the laser power was not considered a critical printing parameter in contrast to the scan speed. The result of the analysis on these variables provides information of the relevance of the exposure time of the laser beam on the powder surface. As the exposure of the powder to the laser beam is extended, the heat absorbed by the material diffuses on the powder bed, causing larger deformation in the printed layer due to the surface tension effect. The laser radiation time (t_r)can be calculated by dividing the laser beam spot size (d), by the scanning speed (V). t_r=d/v.

There is a detrimental effect on the 3D printed parts when the layer thickness is increased. The overall density of silica volumes has a more considerable repercussion with a varied layer thickness than with varied laser power. Layer thickness below 0.1mm presented a larger dimension error than cubes printed at a layer thickness of 0.1mm. Cubes printed with 1.5mm and above, presented a lack of attachment between the layers.

The development of the 3D printing process for silica bodies using the LPBF method was reported, concluding with the successful fabrication of porous silica bodies with an average relative density of 51% using a volumetric energy density of 2.2J/mm^3.

7.1.2.1 Doped silica powder

The process of doping silica powder was developed to produce the 3D printed parts for doped optical fibres. Spherical silicon dioxide and germanium dioxide (GeO_2) were mixed mechanically, producing doped silica powder. It was found that at a low GeO_2 content, the mixture presents a similar angle of repose compared to pristine SiO_2 powder, regardless of the germanium particles morphology. From a

thermogravimetric analysis, it was estimated that the glass transition temperature of the mixed powder was approximately 250°C lower than the pristine spherical silica powder. The added GeO_2 affected the T_g and T_m of the powder even though the powder was not fused by a chemical reaction. Therefore, the printing parameters of the doped powder had to be adjusted, starting with a poor relative density on the printed parts of less than 30% using an energy density of 2.1J/mm^3. The main cause of the low density was warpage and voids between layers. The energy density applied in the printing process was reduced to just below 2J/mm^3, reaching a relative density of 46%. It might be possible to increase the density in the printed parts, reducing the exposure time of the laser beam on the powder surface and, increasing the power of the laser. However, more studies related to doped silica powder and their printing process must be done to conclude a final model.

7.1.2.2 3D printed silica preforms

The fabrication of optical preforms with complex geometries for single and multiple materials was developed. The results presented in Chapter 4 described the printing process for 3D printed optical silica micro-structured designs such as PCF and ARF; in addition, the fabrication process of a 3D printed multicore optical preform was described. The minimum wall-thickness resolution reached for the printed part with spherical silica powder is 1mm. The structures printed with a wall thickness below this resolution were fragile, and the internal lattice did not remain after the cleaning process. The printing parameters to produce preforms with complex geometries were developed. The 3D printed PCF and ARF silica preforms were fabricated with an energy density of 2.7J/mm^3, in contrast to solids printed at slightly lower energy density (ED) of 2.5J/mm^3, reported in Chapter 3. The preforms with an internal lattice and a thin wall thickness did not present visible warpage with an increased energy density. The minimum diameter of a 3D printed porous preform is 3mm using the reported printing parameters.

The core rods were printed initially horizontally due to their small dimensions; however, they showed massive stress in the printed parts, causing delamination and defects in the final preform. Thus, the printing strategy of the core rods was modified to be printed vertically with successful results, using an energy density of 1.9J/mm^3. The multi-materials preform was produced by assembling 3D printed silica cladding structures, and 3D printed doped silica rods.

7.1.3 Post-processing of 3d printed silica solids

The 3D printed silica structures were heat-treated to improve the overall density of the printed bodies. The post-process was carried out aiming to produce a full, dense amorphous glass. The first set of experiments was set up with a dwelling time of 3 hours at different temperatures from 1550˚C to 1600˚C. The treated solids presented an average shrinkage of 35%. The samples treated at temperatures above 1580˚C presented cracks on the surface. The fractures were explained by the stress presented in the samples due to a visible crystallisation on the surface of the solid. After the heat treatment, all parts went through a nucleation process during the cooling period, reaching a full crystallisation of the samples. This crystallisation was explained by the formation of cristobalite crystals in the 3D printed silica structures due to the heat treatment. The origin of the nucleation was the crystalline nature of the raw material demonstrated by the XRD analysis. Further XRD analysis evaluated the conditions of temperature and dwelling, where the phase change occurs. A threshold was found, where the samples start to exhibit severe crystallisation. This occurred, at a maximum duration of 1.5 hours (10min dwell) of the densification process and temperatures above 1580˚C. 3D printed parts densified below the threshold presented a final relative density between 90% and 95%.

The full densification and transparency of the silica printed parts were not reached during the heat treatment, but the crystallisation of the samples was avoided. The fully amorphous state of the glass was reached in the drawing tower furnace, where the silica was drawn at a temperature above 2000˚C, and a vacuum system was used during the process. The densification parameters are significantly affected by the particle size of the silica powder; the smaller the particle size, the greater the driving force for the mass to flow. Transparent glass can be obtained from SiO_2 nanoparticles using a sintering temperature of 1500˚C without vacuum1. However, the particle size of the silica powder used in the presented research work is a thousand orders of magnitude greater than the soot used to produced transparent silica glass. Therefore, it is not possible to reach the full transparency of the printed parts with the threshold temperature chosen in the process and without a vacuum system. Nevertheless, the melting temperature was reached in the drawing furnace, and the voids presented in the printed solids can be eliminated using vacuum during the fibre pulling.

7.1.4 Optical fibre fabrication and characterization

The 3D printed preforms fabricated using the LPBF method were prepared for drawing, using an external glass tube F-300. The assembly was placed in the furnace tower, and the optical fibre was drawn and coated with a high index UV curable polymer DSM-314. The background loss of the multimode fibres was measured. The fibre with a core diameter of 110μm showed a large number of black holes, as a result of a noticeable porosity across the core region. This fibre presented attenuation of ~50dB/m at a wavelength of 800nm. The second fibre was drawn with a core diameter of 45μm, and the vacuum system was used during the process. The attenuation of the second fibres was ~23dB/m at the same wavelength. Due to the low NA between the 3D printed silica preforms and the fluorinated tube higher induced modal propagation losses were noticed for the fibre with a bigger core.

The optical profile of the spherical silica powder was measured using an optical fibre fabricated with the powder in tube technique. The fibre with a spherical powder core presents a transmission from the visible to the NIR with a minimum attenuation level of 1.4dB/m at a wavelength of 800nm. The difference in attenuation between raw silica and the fibres fabricated from the 3D printed bodies can be attributed to the porosity in the 3D printed part, which causes the light to scatter.

An optical fibre with an OD of 100μm was drawn from a 3D printed preform with silica cladding and a core composition of SiO_2 – GeO_2 mixed at 4mol% of germanium oxide. The multiple materials optical fibre presents an attenuation of 8.3dB/m at 800nm. This is an improvement of approximately 36% in comparison to the pure silica core fibres. The enhancement of the attenuation values is due to the lower glass transition temperature of the Ge-doped powder, which can effectively promote a denser material and therefore, fewer defects after the printing and sintering processes. In addition, a multicore optical fibre was drawn from a 3D printed multicore preform. The fibre presents large defects in the core regions due to the stress in the printed cores. Even though the vacuum system was used during the drawing process, it did not compensate for the large gaps in the preform core areas.

3D printed silica preforms were pulled to obtain PCF and ARF with an OD of 200μm. The structure was not controlled during the drawing process. The air-holes collapsed, and the internal lattice did not remain. The lack of control on the internal

lattice of the fibre, during the drawing process, was a combination of two factors: the inhomogeneous heat distribution in the preform and the porosity of the 3D printed preform. It is necessary to improve the densification of the printed silica preforms prior to the fibre fabrication process.

7.2 Silica Optical Fibres produced by Direct Ink Writing Method

Nanoparticulate hydrophobic silica powder was used to produce a colloidal ink to obtain a 3D printed Er-doped silica optical fibre with the Direct Ink Writing (DIW) method. The results presented in chapter five describe the development of the composite. In addition, the fabrication methodology to produce optical fibre is described. Finally, the characterisation of the fibre was presented. In this section, we will discuss the features of the colloidal ink and the potential to produce doped glasses with this method. In addition, we will discuss the performance of the optical fibre and its fabrication development process.

7.2.1 Colloidal ink preparation

Micro and nanoparticles of silica were used to produce a colloidal ink, which can be used in a DIW printing process. The silica compound contains a polymer binder (polydimethylsiloxane (PDMS)), a solvent with a high boiling point, known as tetraglyme. The content of the binder in ink was fixed at 2wt% to avoid contamination in the silica after the heat treatment.

The first evaluation of the silica powder was carried out based on the silica particle size. Secondly, the wt% of silica present in the compound was analysed. The study evaluated the viscosity of the compound and its transparency after being exposed to densification. Finally, the heat treatment was developed to densify the compound and eliminate the solvent and binder present in ink. The mass loss and densification of the compound were evaluated.

It was observed that the use of powders with smaller particle size improves the densification of the printed parts. As explained in previous sections, the mass flow is favourable with smaller particle sizes. Therefore, nanoparticles of hydrophobic silica were selected to produce the colloidal ink. The viscosity of the silica compound was controlled by the solvent-solute ratio. The content of silica as solute varied from 6wt% to 20wt% in the compound. Ink with low content of silica, (below 6wt%), presented a liquid consistency, while ink with more than 15wt% of silica was

dry. The ink with silica content between 12 and 13w% exhibited better extrusion conditions than composites with less silica content. Thus, further ink composition was developed considering 12wt% content of silica powder in the compound.

The elimination of solvent and binder in ink was carried out by heat treatment. Solvent evaporation was set at 90˚C, just below the boiling point of the solvent. After 24 hours, the solvent was totally removed, and the ink reduced 82% of its original volume. The non-organic binder is burned with a temperature of 600˚C, which is just above the boiling point of the polymer. It was observed that samples treated at higher temperatures or with abrupt temperature changes broke during the heat treatment. After the burning stage, the samples were exposed to a temperature of 1575˚ for full densification, after 20 minutes of dwell time. The samples have lost 20 times their original volume, and the full transparent object was obtained; however, its relative density was only 83%. The developed treatment leaves room for densification improvement, for example, if a vacuum is applied during the process. Nonetheless, the full transparency of the solids produced from the developed silica ink was successfully demonstrated.

7.2.2 Optical fibre fabrication and characterization

The DIW method was used to produce a 3D printed Er-doped silica solid to be used as a core of an optical preform. A colloidal ink was developed incorporating the rare-earth (RE) in chloride form with a purity of 6N. The composite composition was 12wt% SiO_2, 2wt% PDMS, 85wt% of tetraglyme and 1wt% Er chloride. A modified Ultimaker^{+2} was used to deposit the composite mixture. The produced solid was dry and densified, reaching a final relative density of 82%.

The 3D printed doped silica solid was assemble inside a fluorinated tube and drawn at 2000˚C on a fibre drawing tower. A multimode Er-doped optical fibre with a core diameter of ~50µm was fabricated. Energy-dispersive X-ray spectroscopy (EDX) analysis confirmed the incorporation of erbium into the silica glass. The Fibre also presents an absorption of 62.98dB/m at 980nm and 151.49dB/m at 1535nm. The fibre shows additional absorptions at ~1380nm and ~1030nm, which are likely to be the contribution of residual OH, PDMS and impurities from the starting materials. Based on the transmission wavelength range, the lower attenuation of the fibres of ~3bB/m is shown at 1100nm.

7.3 Polymer Preforms by Fused Deposition Modelling

A comprehensive analysis of the 3D printing process and its impact on the final optical preforms was performed. The effect of the nozzle diameter on the printed part was studied. It was observed that the combination between the nozzle diameter and the layer thickness has an effect on the size of the defects between the printed stripes. The 3D printed solids presented smaller defect sizes between the stripes when the layer thickness was smaller than the nozzle diameter. Based on the experimental data relation between the layer thickness (h) and the nozzle diameter (w), given by $h<0.5w$. In addition, the effect of different printing lattices in the transparency of the 3D printed parts was evaluated. It was found that modifying the printing lattice can be advantageous for the fabrication of optical fibres.

7.3.1 Fabrication of COC filament

Cyclic Olefin Copolymer TOPAS 8007X10 was extruded to obtain the filament for FDM process. A 3DEVO desktop extruder was used to heat the bulk material along of its extruder worm, which contains four heaters to control the material viscosity. Three different heating strategies, warming the heating zones, were followed to produce a transparent and well-defined filament: constant temperature, decreasing temperature and increasing temperature. The extrusion speed remained constant at 50mm/min. It was observed that the transparency of the material improves at higher constant extrusion temperatures. However, the diameter of the filament presented a larger deviation with increasing extrusion temperatures. When the temperature gradually decreased during the extrusion process, the filament showed degradation, such as bubbles that were trapped inside the filament. The decreased temperature profile in the heating zones does not have a positive effect on the extruded filament, which presented an elliptical shape. In contrast, increasing the temperature along the heating zones produced filaments with a small OD deviation and good transparency. The produced COC filament was used to fabricate 3D printed preforms with solid and lattice structures. The accuracy of the developed 3D printing process is ±0.05mm with respect to the CAD design. Air holes can be produced with diameters above 1mm without deformation. Complex shapes can be produced with good edge definition at the holes.

7.3.2 Optical fibre fabrication and characterization

3D printed circular samples with a diameter of 20mm and 5mm in height with a layer thickness of 100µm were produced in TOPAs to characterise the printing process. The effect of the process temperature in the printed layer was analysed. Samples printed with nozzle temperatures below 220˚C presented gaps between the deposited stripes, while samples printed with nozzle temperatures above 240˚C exhibited signs of degradation of the polymer. A nozzle temperature of 230˚C was used for TOPAS printed parts, as they showed a regular grid structure without a rough surface.

3D printed COC cylinders with a length of 150mm and a diameter of 20mm were produced using two printing patterns: orthogonal and concentric. The cylinders were drawn in external facilities using a furnace with temperatures set at to 200˚C on the upper zone (UZ), and 165˚C on the lower zone (LZ). The obtained COC fibres were characterised using terahertz-time domain spectroscopy (THz-TDS). The study of COC fibres in the THz region provided the refractive index and the THz spectrum transmission from the THz time-domain scans.

An average refractive index of 1.5319 was estimated from the experimental data, which correspond to the theoretical refractive index of COC of 1.53. Therefore, the THz transmission of the 3D printed fibre was validated.

The attenuation intrinsic to the printing pattern was evaluated by a cutback method using the THz-TDS set up. The attenuation of two preforms printed with different patterns: grid and concentric were evaluated. The produced fibres transmit in the range below 0.5THz with attenuation similar to the noise level above 0.8THz. Fibres with a grid pattern exhibit higher attenuation than those with a concentric pattern. The signal amplitude in both fibres increased as the fibre length is reduced; however, the quality of the signal is low.

Chapter 8 Conclusions and Future Work

The conclusions and further suggestions to continue the presented research work are listed in this chapter. The need for innovative fabrication methods for optical fibres with novel designs has been toughly discussed in this thesis. The specific conclusions of the results presented in chapter 3,4,5 and 6 are listed accordingly to the materials and the respectively AM methods applied to process them. Based on the results of the explored additive manufacturing method in the presented research work, we can, in general, conclude that the fabrication of silica optical fibres by additive manufacturing methods viable. Further analysis in the LPBF method can be persuaded using purer silica powders, while DIW method present advantages over LPBF for optical fibre fabrication.

8.1 Conclusions

8.1.1 SiO_2 optical fibres fabricated through 3D printing processes

- The application of AM technologies in the fabrication of optical fibres was analysed, and a general overview of the current 3D printing process was studied and discussed.
- Two AM method for silica optical preforms fabrication were selected to be analysed in this thesis: Laser Powder Bed Fusion (LPBF) and Direct Ink Writing (DIW)

8.1.1.1 LPBF

- Spherical silica powder was used to produce 3D printed preforms using the LPBF method. The mechanical and physical features of the selected powder were analysed, finding that regular shape and particle sizes above 30μm presented better flowability than powder with smaller particle sizes and irregular shape. The impurities contained in the silica powder have an effect on the softening and the melting point of the powder; therefore, the printing parameters depend on the content of impurities in the silica powder.
- Single tracks of 3D printed silica powder at linear energy density below 100J/m presented no neck formation. In contrast, single tracks printed with an energy density above 200J/m presented warpage. The tracks printed with

an energy density between 12 to 150J/m showed defined edges, good mechanical strength and no visible warpage.

- Single layers of 3D printed silica powder with an average energy density of 0.6J/mm^2 presented a low warpage level and neck formation between the powder particles.
- The laser power was not considered a critical printing parameter in contrast to the scan speed. The exposure time of the laser beam on the powder bed must be taken into consideration for the printing process of silica powder. Due to the heat absorbed by the material at a long period of time, the printed layers present larger warpage because of the surface tension effect. The exposure time used in the fabrication of silica cubes was 0.1ms.
- It is possible to reach an average relative density in the silica printed green bodies above 60%; however, the dimensions are not accurate as the printed bodies had a relative density between 50 and 52%. This density can be achieved using an energy density of approximately 2.5J/mm^3.
- Ge-doped silica powder was printed using the LPBF method. A mechanical doping process was developed and reported in this PhD thesis. The characterisation of the powder was presented, finding the appropriate flowability condition of the mixed powder in correlation to the mixing ratio. The printing conditions for a 4wt% Ge-doped silica powder was established. Ge-doped silica porous bodies were printed using an energy density of 1.96J/mm^3, with a relative density of approximately 46%.
- Post-printing densification of the 3D printed silica solids was performed. The threshold for the process was found to be at a temperature just below 1580˚C and at a maximum cycle of 1.5 hours (10min of dwell), reaching a maximum final density of 95%.
- 3D printed silica preforms were successfully fabricated. The capability to print thin walls and complex geometries with reasonable control of the printing structures was demonstrated using a low volumetric energy density of 2.7J/mm^3 in the LPBF process. In addition, multi-material preforms were produced by assembling doped core and cladding structures.
- The fabrication of optical fibres from 3D printed silica preforms was successfully demonstrated. The transmission wavelength range of the optical fibres is between 600 and 1200nm. The lower attenuation level of the 3D printed silica fibre is ~23dB/m at a wavelength of 800nm.
- A multicore fibre was fabricated from a 3D printed silica preform. The fabrication of 3D printed optical preforms using multi-materials was

demonstrated using Ge-doped silica in step-index and multicore preforms. Ge-doped optical fibre was fabricated from the printed preforms in a drawing process. The Ge-doped fibre presented attenuation of 8.3dB/m at 800nm. The losses are improved by approximately 36% compared to the silica core fibres.

8.1.1.2 Direct Ink Writing (DIW)

- A recipe for fabricating a colloidal ink of doped silica for optical preform fabrication for direct ink writing (DIW) was developed. The use of nanoparticulate and amorphous hydrophilic SiO_2 powder at 12wt% in the compound is favourable for the printing and densification of the silica. It was demonstrated that it is possible to incorporate rare-earth to silica with the colloidal ink recipe.
- The fabrication of erbium-doped silica optical fibre from a 3D printed silica preform using DIW method was shown. The produced erbium-doped fibre was characterised, and the optical profile was reported with absorption of 62.98dB/m at 980nm and 151.49dB/m at 1535nm. The first 3D printed RE-doped silica fibre and preform were reported, and their potential for laser applications was mentioned.
- It was confirmed that the attenuation level of the optical fibres produced with an AM method is improved by using nanoparticle-sized silica powder, which promotes the densification process of the printed parts.

8.1.2 Polymer optical fibres fabricated with a 3D printing process

- The use of FDM fabrication methods was discussed, and the development of the fabrication parameters for PMMA and COC was established. Along with the analysis of the printing parameters, the relationship between layer thickness (h) and nozzle diameter (w), given by $h<0.5w$ was defined.
- Several meters of COC filament was produced under controlled extrusion conditions. The development of the filament fabrication process opens the possibility to explore different materials for speciality polymer optical fibre fabrication.
- The produced TOPAS filament was used to successfully fabricate 3D printed preforms with solid and complex structures. The accuracy of the developed 3D printing process is ±0.05mm with respect to the CAD design. Air holes

can be produced with diameters above 1mm without deformation. Complex shapes can be produced with good edge definition at the holes.

- The 3D printed COC solids were drawn, and the fabricated fibres were characterised using THz-TDS, showing transmission in the range below 0.5THz with attenuation similar to the noise level above 0.8THz.

8.2 Future Work

This research is the first complete study in the application of AM technologies for optical fibre fabrication. Through this PhD thesis, the advantages, drawbacks and fundamentals for optical preform fabrication using AM manufacturing methods (LPBF, DWI and FDM) are analysed, providing the framework for further studies in this area. Even though this research work already presented successful results in silica optical fibre fabrication, there is still more investigation required in this field.

8.2.1 SiO_2 optical fibre by 3D printing processes

The recommendations for future work on processing silica by additive manufacturing in this section are based on the presented results from this research thesis.

8.2.1.1 **LPBF**

a) The use of higher purity silica powders is desired for the fabrication of optical preforms using the LPBF method. However, the use of soot silica is not suitable for this technique due to the poor flowability of small particles. One potential solution is to use a liquid-phase sintering method, coating the soot silica and processing it using the LPBF method. Another potential solution is to use a DED method, feeding a coated silica powder though a nozzle and melting the coated material instead of the silica powder. Further studies of high purity silica powder are suggested to reduce the attenuation level of the fibres due to impurities in the raw material.

b) The initial printing parameters for porous silica bodies were established in this PhD thesis; however, an additional heat transfer analysis and the effect of the laser beam on the kinetic of the neck growth of the silica powder can be an output of an undergraduate or master thesis. It is recommended to develop a heat transfer simulation and develop a theoretical model to predict the printing conditions for doped silica.

c) The viability to process doped silica powder using the LPBF method was demonstrated. It is recommended to improve the density of the printed doped parts. Incorporate new dopants and improve the bonding mechanisms between silica and the dopants is suggested as the next stage of this study.

d) The use of multi-materials in the SLS process was successfully demonstrated; however, further experimental work is suggested to explore a wider variety of glass compositions, which can include the addition of dopants such as rare-earth (RE) for laser applications.

e) To improve the densification of the 3D printed porous bodies is the key to improve the fabrication of optical fibre. This might be possible if a vacuum system is applied during heat treatment. Improving the density can contribute to improving the losses on the optical fibre attributed by the porosity of the 3D printed part, which causes the light to scatter.

f) The pressure control on the drawing process for preforms with complex internal lattice is a challenge that must be tackled for successfully developing 3D printed preforms with complex geometries. In contrast to solid preforms, where a vacuum system can be used during the drawing to eliminate vacancies in the preform, 3D printed preforms with internal lattices, such as PFC and ARF, need to use pressure to keep and control the internal structure. Therefore, the voids already present in the structure cannot be reduced. Moreover, the porosity does not allow to control the geometry on the fibre. Therefore, it is recommended to improve the density of the 3D printed preforms prior to the drawing process.

8.2.1.2 **Direct Ink Writing (DIW)**

a) The DIW process for optical fibre fabrication requires further process development as well as the optimisation of the colloidal ink. The incorporation of new rare-earth or other compounds to modify the features of the glass host can be part of future work to improve the performance of the produced optical fibres. In addition, the refinement of drying and thermal decomposition of the binder and densification process must be

optimised. For instance, the densification of the ink can be improved if a vacuum system is applied during the heat-treatment.

8.2.2 Polymer optical fibre fabricated by a 3D printing process

a) During the FDM process, it was demonstrated that the printing pattern plays an important part in the optical characteristics of the preform. Further research on the effect of different and unusual printing patterns can be achieved by modifying the printer software. This modification might improve the attenuation level in the POF. Moreover, it can also improve the deformation of the fibre during the drawing process for MPOF.
b) It is essential to complement the fabrication capabilities of the Optoelectronics Research Centre with a system that allows the drawing of polymer optical fibres. Unfortunately, the existing facilities are not suitable for the materials used in this thesis. The use of external facilities limited the possibility to explore the polymer optical fibre fabrication further.

List of References

1 Montgomery, S. in *Specialty Optical Fibers Handbook* (eds Alexis Méndez & T. F. Morse) 1-17 (Academic Press, 2007).

2 Kara, P. Polymer optical fiber sensors—a review. *Smart Materials and Structures* **20**, 013002 (2011).

3 Lee, B. Review of the present status of optical fiber sensors. *Optical Fiber Technology* **9**, 57-79, doi:https://doi.org/10.1016/S1068-5200(02)00527-8 (2003).

4 Pissadakis, S. Lab-in-a-fiber sensors: A review. *Microelectronic Engineering* **217**, 111105, doi:https://doi.org/10.1016/j.mee.2019.111105 (2019).

5 Pinkerton, A. J. [INVITED] Lasers in additive manufacturing. *Optics & Laser Technology* **78**, 25-32, doi:https://doi.org/10.1016/j.optlastec.2015.09.025 (2016).

6 Li, T. *Optical fiber comunication,* . Vol. 1 1-177 (1985).

7 MacChesney, J. B., Bise, R. & Méndez, A. in *Specialty Optical Fibers Handbook* (eds Alexis Méndez & T. F. Morse) 69-94 (Academic Press, 2007).

8 Liu, D., Tong, W., Liu, S. & Liu, H. *Study on the fabrication techniques of photonic crystal fiber and PCF based structures*. Vol. 5722 PWO (SPIE, 2005).

9 Bandyopadhyay, A. *Additive manufacturing*. (CRC Press, 2015).

10 Furlan, W. D. *et al.* 3D printed diffractive terahertz lenses. *Optics Letters* **41**, 1748-1751, doi:10.1364/OL.41.001748 (2016).

11 Cook, K. *et al.* Air-structured optical fiber drawn from a 3D-printed preform. *Optics Letters* **40**, 3966-3969, doi:10.1364/ol.40.003966 (2015).

12 Suszek, J. *et al.* 3-D-Printed Flat Optics for THz Linear Scanners. *IEEE Transactions on Terahertz Science and Technology* **5**, 314-316, doi:10.1109/TTHZ.2015.2398313 (2015).

13 Argyros, A. Microstructured Polymer Optical Fibers. *J. Lightwave Technol.* **27**, 1571-1579 (2009).

14 Alexis Mendez, T. F. M. *Specialty Optical Fibers Handbook*. (Academic Press, 2006).

15 Desurvire, E., Giles, C. R., Simpson, J. R. & Zyskind, J. L. (Google Patents, 1991).

16 Jensen, J. B. *et al.* in *Sensors, 2003. Proceedings of IEEE.* 269-278 Vol.261.

17 Nowosielski, J. *et al.* Large diameter nanostructured gradient index lens. *Opt. Express* **20**, 11767-11777, doi:10.1364/oe.20.011767 (2012).

18 Paschotta, R. *Field Guide to Optical Fiber Technology*. (2010).

19 Wu, J., Yao, Z., Zong, J. & Jiang, S. Highly efficient high-power thulium-doped germanate glass fiber laser. *Optics Letters* **32**, 638-640, doi:10.1364/OL.32.000638 (2007).

20 Monro, T. M., West, Y. D., Hewak, D. W., Broderick, N. G. R. & Richardson, D. J. Chalcogenide holey fibres. *Electronics Letters* **36**, 1998-2000, doi:10.1049/el:20001394 (2000).

21 MacChesney, J. B. & O'Connor, P. B. (Google Patents, 1982).

22 Mazzarese, D. J., Mcmahon, T. F., Oulundsen, G. E. & Owsiany, M. T. (Google Patents, 2000).

23 Nagel, S., MacChesney, J. & Walker, K. An overview of the modified chemical vapor deposition (MCVD) process and performance. *IEEE Journal of Quantum Electronics* **18**, 459-476, doi:10.1109/JQE.1982.1071596 (1982).

24 Li, M.-J. & Nolan, D. A. Optical Transmission Fiber Design Evolution. *J. Lightwave Technol.* **26**, 1079-1092 (2008).

25 Shukla, S. K., Kushwaha, C. S., Guner, T. & Demir, M. M. Chemically modified optical fibers in advanced technology: An overview. *Optics & Laser Technology* **115**, 404-432, doi:https://doi.org/10.1016/j.optlastec.2019.02.025 (2019).

26 Heyvaert, S., Ottevaere, H., Kujawa, I., Buczynski, R. & Thienpont, H. Stack-and-draw technique creates ultrasmall-diameter endoscopes. *Laser Focus World* **49**, 29-+ (2013).

27 Hansen, T. P. *et al.* Highly birefringent index-guiding photonic crystal fibers. *IEEE Photonics Technology Letters* **13**, 588-590, doi:10.1109/68.924030 (2001).

28 Muhd-Yassin, S. Z. *et al.* Solution doped preform with improved uniformity and concentration using dual-layer soot deposition. *Optical Fiber Technology* **28**, 23-27, doi:10.1016/j.yofte.2016.01.003 (2016).

29 Webb, A. S. *et al.* MCVD in-situ solution doping process for the fabrication of complex design large core rare-earth doped fibers. *Journal of Non-Crystalline Solids* **356**, 848-851, doi:https://doi.org/10.1016/j.jnoncrysol.2010.01.008 (2010).

30 Tang, F. Z., McNamara, P., Barton, G. W. & Ringer, S. P. Multiple solution-doping in optical fibre fabrication II – Rare-earth and aluminium co-doping. *Journal of Non-Crystalline Solids* **354**, 1582-1590, doi:https://doi.org/10.1016/j.jnoncrysol.2007.10.006 (2008).

31 Tang, F. Z., McNamara, P., Barton, G. W. & Ringer, S. P. Multiple solution-doping in optical fibre fabrication I – Aluminium doping. *Journal of Non-Crystalline Solids* **354**, 927-937, doi:https://doi.org/10.1016/j.jnoncrysol.2007.08.020 (2008).

32 Macho, A., Morant, M. & Llorente, R. Next-Generation Optical Fronthaul Systems Using Multicore Fiber Media. *J. Lightwave Technol.* **34**, 4819-4827, doi:10.1109/jlt.2016.2573038 (2016).

33 Mahdiraji, G. A. *et al.* Multicore Flat Fiber: A New Fabrication Technique. *Ieee Photonics Technology Letters* **26**, 1972-1974, doi:10.1109/lpt.2014.2343637 (2014).

34 Roy Choudhury, S. & Jaluria, Y. Practical aspects in the drawing of an optical fiber. *Journal of Materials Research* **13**, 483-493, doi:10.1557/JMR.1998.0063 (2011).

35 Dragic, P. D., Cavillon, M. & Ballato, J. Materials for optical fiber lasers: A review. *Applied Physics Reviews* **5**, 041301, doi:10.1063/1.5048410 (2018).

36 Ramírez-Martínez, N. J., Núñez-Velázquez, M., Umnikov, A. A. & Sahu, J. K. Highly efficient thulium-doped high-power laser fibers fabricated by MCVD. *Opt. Express* **27**, 196-201, doi:10.1364/OE.27.000196 (2019).

37 Price, J. H. V. *et al.* Supercontinuum generation in non-silica fibers. *Optical Fiber Technology* **18**, 327-344, doi:https://doi.org/10.1016/j.yofte.2012.07.013 (2012).

38 Ben-David, M. & Gannot, I. in *Specialty Optical Fibers Handbook* (eds Alexis Méndez & T. F. Morse) 699-733 (Academic Press, 2007).

39 Nazempour, R., Zhang, Q., Fu, R. & Sheng, X. Biocompatible and Implantable Optical Fibers and Waveguides for Biomedicine. *Materials (Basel)* **11**, 1283, doi:10.3390/ma11081283 (2018).

40 Wheeler, N. V. *et al.* Low-loss Kagome hollow-core fibers operating from the near- to the mid-IR. *Optics Letters* **42**, 2571-2574, doi:10.1364/OL.42.002571 (2017).

41 Belardi, W. Design and Properties of Hollow Antiresonant Fibers for the Visible and Near Infrared Spectral Range. *J. Lightwave Technol.* **33**, 4497-4503, doi:10.1109/JLT.2015.2477775 (2015).

42 Emslie, C. in *Specialty Optical Fibers Handbook* (eds Alexis Méndez & T. F. Morse) 243-277 (Academic Press, 2007).

43 Koike, Y. & Koike, K. Progress in low-loss and high-bandwidth plastic optical fibers. *Journal of Polymer Science Part B: Polymer Physics* **49**, 2-17, doi:10.1002/polb.22170 (2011).

44 Rajan, G. *Optical fiber sensors: advanced techniques and applications*. Vol. 36 521 (CRC Press, 2015).

45 Koike, Y. & Takahashi, S. in *Optical Fiber Telecommunications V A (Fifth Edition)* (eds Ivan P. Kaminow, Tingye Li, & Alan E. Willner) 593-603 (Academic Press, 2008).

46 Ziemann, O., Krauser, J. & Zamzow, P. E. *POF Handbook: Optical Short Range Transmission Systems*. 79-93 (Springer Berlin Heidelberg, 2008).

47 Arrospide, E. *et al.* in *Polymer Optical Fibres* (eds Christian-Alexander Bunge, Thomas Gries, & Markus Beckers) 201-216 (Woodhead Publishing, 2017).

48 Koike, Y. & Inoue, A. High-Speed Graded-Index Plastic Optical Fibers and Their Simple Interconnects for 4K/8K Video Transmission. *J. Lightwave Technol.* **34**, 1551-1555, doi:10.1109/JLT.2016.2517086 (2016).

49 Zubia, J. & Arrue, J. Plastic Optical Fibers: An Introduction to Their Technological Processes and Applications. *Optical Fiber Technology* **7**, 101-140, doi:http://dx.doi.org/10.1006/ofte.2000.0355 (2001).

50 Fasano, A. *et al.* Fabrication and characterization of polycarbonate microstructured polymer optical fibers for high-temperature-resistant fiber Bragg grating strain sensors. *Opt. Mater. Express* **6**, 649-659, doi:10.1364/OME.6.000649 (2016).

51 Emslie, C. Polymer optical fibres. *Journal of Materials Science* **23**, 2281-2293, doi:10.1007/bf01111879 (1988).

52 Beckers, M., Schlüter, T., Vad, T., Gries, T. & Bunge, C.-A. An overview on fabrication methods for polymer optical fibers. *Polymer International* **64**, 25-36, doi:10.1002/pi.4805 (2015).

53 Eijkelenborg, M. A. v. *et al.* Microstructured polymer optical fibre. *Opt. Express* **9**, 319-327, doi:10.1364/OE.9.000319 (2001).

54 ASTM52900-15, I. (ASTM International,, West Conshohocken, PA, , 2015).

55 Kodama, H. Automatic method for fabricating a three‐dimensional plastic model with photo‐hardening polymer. *Review of Scientific Instruments* **52**, 1770-1773, doi:10.1063/1.1136492 (1981).

56 Hull, C. W. Apparatus for production of three dimensional objects by stereolithography. The United States patent US6027324A (1984).

57 Masters, W. E. Computer Automated Manufacturing Process and Systems. The United States patent US4665492A (1987).

58 Bandyopanhyay, A. *Additive Manufactiring*. (CRC Press, 2015).

59 Butscher, A., Bohner, M., Hofmann, S., Gauckler, L. & Müller, R. Structural and material approaches to bone tissue engineering in powder-based three-dimensional printing. *Acta Biomaterialia* **7**, 907-920, doi:http://dx.doi.org/10.1016/j.actbio.2010.09.039 (2011).

60 Gao, W. *et al.* The status, challenges, and future of additive manufacturing in engineering. *Computer-Aided Design* **69**, 65-89, doi:https://doi.org/10.1016/j.cad.2015.04.001 (2015).

61 Lee, J.-Y., An, J. & Chua, C. K. Fundamentals and applications of 3D printing for novel materials. *Applied Materials Today* **7**, 120-133, doi:https://doi.org/10.1016/j.apmt.2017.02.004 (2017).

62 Dizon, J. R. C., Espera, A. H., Chen, Q. & Advincula, R. C. Mechanical characterization of 3D-printed polymers. *Additive Manufacturing* **20**, 44-67, doi:https://doi.org/10.1016/j.addma.2017.12.002 (2018).

63 Pinkerton, A. J. [INVITED] Lasers in additive manufacturing. *Optics & Laser Technology* **78, Part A**, 25-32, doi:http://dx.doi.org/10.1016/j.optlastec.2015.09.025 (2016).

64 Wang, X., Gong, X., Chou, K. & Asme. *REVIEW ON POWDER-BED LASER ADDITIVE MANUFACTURING OF INCONEL 718 PARTS*. (2015).

65 Bandyopadhyay, A. B. S. *Additive manufacturing*. 143-183 (CRC Press, 2015).

66 Zocca, A., Colombo, P., Gomes, C. M. & Günster, J. Additive Manufacturing of Ceramics: Issues, Potentialities, and Opportunities. *Journal of the American Ceramic Society* **98**, 1983-2001, doi:10.1111/jace.13700 (2015).

67 Stucker, I. G. D. R. B. *ADDITIVE MANUFACTURING TECHNOLOGIES*. (2014).

68 Kruth J‐, P., Mercelis, P., Van Vaerenbergh, J., Froyen, L. & Rombouts, M. Binding mechanisms in selective laser sintering and selective laser melting.

Rapid Prototyping Journal **11**, 26-36, doi:10.1108/13552540510573365 (2005).

69 Schmid, M., Amado, A. & Wegener, K. Polymer powders for selective laser sintering (SLS). *AIP Conference Proceedings* **1664**, 160009, doi:10.1063/1.4918516 (2015).

70 Spierings, A. B., Voegtlin, M., Bauer, T. & Wegener, K. Powder flowability characterisation methodology for powder-bed-based metal additive manufacturing. *Progress in Additive Manufacturing* **1**, 9-20, doi:10.1007/s40964-015-0001-4 (2016).

71 Shirazi, S. F. S. *et al.* A review on powder-based additive manufacturing for tissue engineering: selective laser sintering and inkjet 3D printing. *Sci. Technol. Adv. Mater.* **16**, 20, doi:10.1088/1468-6996/16/3/033502 (2015).

72 Klocke, F. A., C.; McClung, A. Direct laser sintering of borosilicate glass. *Solid Freeform Fabrication Symposium (SFF) <15, 2004, Austin/Tex.>* **Proceedings : August 2 - 4, 2004**, 214-219 (2004).

73 Brunelle, M., Ferralli, I., Whitsitt, R. & Medicus, K. *Current use and potential of additive manufacturing for optical applications*. Vol. 10448 OFB (SPIE, 2017).

74 Wang, H. B., David L; Beaman Jr., Joseph J. Selective Laser Sintering of Quartz Powder. *International Solid Freeform Fabrication Symposium* (1997).

75 Petit, V., Le Rouge, A., Beclin, F., El Hamzaoui, H. & Bigot, L. Experimental Study of SiO2 Soot Deposition using the Outside Vapor Deposition Method. *Aerosol Science and Technology* **44**, 388-394, doi:10.1080/02786821003671315 (2010).

76 Fateri, M. & Gebhardt, A. Selective Laser Melting of Soda-Lime Glass Powder. *International Journal of Applied Ceramic Technology* **12**, 53-61, doi:10.1111/ijac.12338 (2015).

77 Datsiou, K. C. *et al.* Additive manufacturing of glass with laser powder bed fusion. *Journal of the American Ceramic Society* **102**, 4410-4414, doi:10.1111/jace.16440 (2019).

78 Khmyrov, R. S., Grigoriev, S. N., Okunkova, A. A. & Gusarov, A. V. On the Possibility of Selective Laser Melting of Quartz Glass. *Physics Procedia* **56**, 345-356, doi:https://doi.org/10.1016/j.phpro.2014.08.117 (2014).

79 Schwager, A.-M., Bliedtner, J., Bruder, A. & Götze, K. *Manufacturing of three dimensional silicate moldings by selective laser beam sintering*. Vol. 10448 OFB (SPIE, 2017).

80 Chang, S., Li, L., Lu, L. & Fuh, J. Y. H. Selective Laser Sintering of Porous Silica Enabled by Carbon Additive. *Materials* **10**, 1313 (2017).

81 Luo, J. J., Pan, H. & Kinzel, E. C. Additive Manufacturing of Glass. *J. Manuf. Sci. Eng.-Trans. ASME* **136**, 6, doi:10.1115/1.4028531 (2014).

82 Luo, J. *et al. Bubble formation in additive manufacturing of glass*. Vol. 9822 SID (SPIE, 2016).

83 von Witzendorff, P. *et al.* Additive manufacturing of glass: CO2-Laser glass deposition printing. *Procedia CIRP* **74**, 272-275, doi:https://doi.org/10.1016/j.procir.2018.08.109 (2018).

84 Lei, J., Hong, Y., Zhang, Q., Peng, F. & Xiao, H. in *2019 Conference on Lasers and Electro-Optics (CLEO).* 1-2.

85 Billiet, T., Vandenhaute, M., Schelfhout, J., Van Vlierberghe, S. & Dubruel, P. A review of trends and limitations in hydrogel-rapid prototyping for tissue engineering. *Biomaterials* **33**, 6020-6041, doi:https://doi.org/10.1016/j.biomaterials.2012.04.050 (2012).

86 Brian, N. T. A review of melt extrusion additive manufacturing processes: I. Process design and modeling. *Rapid Prototyping Journal* **20**, 192-204, doi:10.1108/RPJ-01-2013-0012 (2014).

87 Parandoush, P. & Lin, D. A review on additive manufacturing of polymer-fiber composites. *Composite Structures* **182**, 36-53, doi:https://doi.org/10.1016/j.compstruct.2017.08.088 (2017).

88 Zubel, M. *et al.* in *25th International Conference on Plastic Optical Fibres - proceedings.*

89 Busch, S. F., Weidenbach, M., Balzer, J. C. & Koch, M. THz Optics 3D Printed with TOPAS. *Journal of Infrared, Millimeter, and Terahertz Waves* **37**, 303-307, doi:10.1007/s10762-015-0236-7 (2016).

90 Nguyen, D. T. *et al.* 3D-Printed Transparent Glass. *Advanced Materials* **29**, 5, doi:10.1002/adma.201701181 (2017).

91 Klein, J. *et al.* Additive Manufacturing of Optically Transparent Glass. *3D Print. Addit. Manuf.* **2**, 92-105, doi:10.1089/3dp.2015.0021 (2015).

92 Baudet, E., Ledemi, Y., Larochelle, P., Morency, S. & Messaddeq, Y. 3D-printing of arsenic sulfide chalcogenide glasses. *Opt. Mater. Express* **9**, 2307-2317, doi:10.1364/OME.9.002307 (2019).

93 Lewis, J. A. Direct Ink Writing of 3D Functional Materials. *Advanced Functional Materials* **16**, 2193-2204, doi:10.1002/adfm.200600434 (2006).

94 Kotz, F. *et al.* Three-dimensional printing of transparent fused silica glass. *Nature* **544**, 337, doi:10.1038/nature22061

https://www.nature.com/articles/nature22061#supplementary-information (2017).

95 Shukrun, E., Cooperstein, I. & Magdassi, S. 3D-Printed Organic–Ceramic Complex Hybrid Structures with High Silica Content. *Advanced Science* **5**, 1800061, doi:10.1002/advs.201800061 (2018).

96 Pandey, S., Gupta, B. & Nahata, A. Terahertz plasmonic waveguides created via 3D printing. *Opt. Express* **21**, 24422-24430, doi:10.1364/OE.21.024422 (2013).

97 Iezzi, V. L., Boisvert, J. S., Loranger, S. & Kashyap, R. 3D printed long period gratings for optical fibers. *Optics Letters* **41**, 1865-1868, doi:10.1364/ol.41.001865 (2016).

98 Prajzler, V., Kulha, P., Knietel, M. & Enser, H. Large core plastic planar optical splitter fabricated by 3D printing technology. *Optics Communications* **400**, 38-42, doi:https://doi.org/10.1016/j.optcom.2017.04.070 (2017).

99 Toal, P. M., Holmes, L. J., Rodriguez, R. X. & Wetzel, E. D. Microstructured monofilament via thermal drawing of additively manufactured preforms. *Additive Manufacturing* **16**, 12-23, doi:https://doi.org/10.1016/j.addma.2017.03.009 (2017).

100 Cook, K. *et al.* Step-index optical fiber drawn from 3D printed preforms. *Optics Letters* **41**, 4554-4557, doi:10.1364/OL.41.004554 (2016).

101 Wang, Y., Gawedzinski, J., Pawlowski, M. E. & Tkaczyk, T. S. 3D printed fiber optic faceplates by custom controlled fused deposition modeling. *Opt. Express* **26**, 15362-15376, doi:10.1364/OE.26.015362 (2018).

102 Talataisong, W. *et al.* Mid-IR Hollow-core microstructured fiber drawn from a 3D printed PETG preform. *Scientific Reports* **8**, 8113, doi:10.1038/s41598-018-26561-8 (2018).

103 Yudasari, N., Anthony, J. & Leonhardt, R. Terahertz pulse propagation in 3D-printed waveguide with metal wires component. *Opt. Express* **22**, 26042-26054, doi:10.1364/OE.22.026042 (2014).

104 Yang, J. *et al.* 3D printed low-loss THz waveguide based on Kagome photonic crystal structure. *Opt. Express* **24**, 22454-22460, doi:10.1364/OE.24.022454 (2016).

105 Cruz, A. L. S., Cordeiro, C. M. B. & Franco, M. A. R. 3D Printed Hollow-Core Terahertz Fibers. *Fibers* **6**, 43 (2018).

106 van Putten, L. D., Gorecki, J., Numkam Fokoua, E., Apostolopoulos, V. & Poletti, F. 3D-printed polymer antiresonant waveguides for short-reach terahertz applications. *Appl. Opt.* **57**, 3953-3958, doi:10.1364/AO.57.003953 (2018).

107 Luo, J. *et al. Additive manufacturing of glass for optical applications*. Vol. 9738 PWL (SPIE, 2016).

108 Chu, Y. *et al.* Silica optical fiber drawn from 3D printed preforms. *Optics Letters* **44**, 5358-5361, doi:10.1364/OL.44.005358 (2019).

109 Peng, G.-D. *et al.* in *Handbook of Optical Fibers* (ed Gang-Ding Peng) 1-17 (Springer Singapore, 2019).

110 Zhang, Q. *et al.* 3D printing of all-glass fiber-optic pressure sensor for high temperature applications. *IEEE Sensors Journal*, 1-1, doi:10.1109/JSEN.2019.2935689 (2019).

111 Camacho-Rosales, A., Núñez-Velázquez, M., Zhao, X., Yang, S. & Sahu, J. K. in *2019 Conference on Lasers and Electro-Optics Europe and European Quantum Electronics Conference.* ce_7_5 (Optical Society of America).

112 Camacho Rosales, A., Núñez Velázquez, M. M., Zhao, X. & Sahu, J. *Optical fibers fabricated from 3D printed silica preforms*. Vol. 11271 PWL (SPIE, 2020).

113 Jones, I. K., Seeley, Z. M., Cherepy, N. J., Duoss, E. B. & Payne, S. A. Direct ink write fabrication of transparent ceramic gain media. *Optical Materials* **75**, 19-25, doi:https://doi.org/10.1016/j.optmat.2017.10.005 (2018).

114 Seeley, Z. *et al.* 3D printed transparent ceramic YAG laser rods: Matching the core-clad refractive index. *Optical Materials* **107**, 110121, doi:https://doi.org/10.1016/j.optmat.2020.110121 (2020).

115 Camacho Rosales, A. L., Núñez-Velázquez, M. & Sahu, J. K. 3D printed Er-doped silica fibre by Direct Ink Writing. *EPJ Web Conf.* **243**, 20002 (2020).

116 USP. (<1174>Powder flow. USP30 NF 25 2007).

117 Beakawi Al-Hashemi, H. M. & Baghabra Al-Amoudi, O. S. A review on the angle of repose of granular materials. *Powder Technology* **330**, 397-417, doi:https://doi.org/10.1016/j.powtec.2018.02.003 (2018).

118 Nunez-Velazquez, M. *Speciality Optical Fibre Fabricated by Outside Vapour Deposition Process* PhD thesis, University of Southampton, (2018).

119 Khanarian, G. Optical properties of cyclic olefin copolymers. *Optical Engineering* **40** (2001).

120 LLC, M. *Overview of materials for Acrylonitrile Butadiene Styrene (ABS), Transparent, Molded*, 2019).

121 polymerdatabase.com. *REFRACTIVE INDEX OF AMORPHOUS POLYMERS*, 2015).

122 Polyanskiy, M. *Refractiveindex.info database*, 2008-2020).

123 Cuan-Urquizo, E., Yang, S., Bhaskar, A. & Iop. in *Advanced Materials for Demanding Applications* Vol. 74 *IOP Conference Series-Materials Science and Engineering* (2015).

124 Agrawal, A. *et al.* Ultra low bending loss equiangular spiral photonic crystal fibers in the terahertz regime. *AIP Advances* **2**, 022140, doi:10.1063/1.4726055 (2012).

125 Yuan, W. *et al.* Humidity insensitive TOPAS polymer fiber Bragg grating sensor. *Opt. Express* **19**, 19731-19739, doi:10.1364/OE.19.019731 (2011).

126 Emiliyanov, G. *et al.* Localized biosensing with Topas microstructured polymer optical fiber. *Optics Letters* **32**, 460-462, doi:10.1364/OL.32.000460 (2007).

127 Fuentes-Silva C., O.-M. M. A., Noriega-Ponce A, Serroukh I. in *Ingeniería Investigación y Tecnología UNAM* Vol. XIII 175-184 (2012).